CHARLES UNIVERSITY
Faculty of Mathematics and Physics

Doctoral Thesis

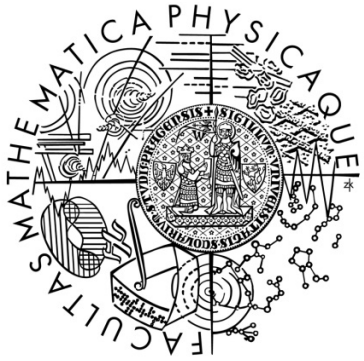

Elizabeth Vakkechalil John

SPECTROSCOPIC INVESTIGATION OF LATTICE DYNAMICS IN MULTIDOMAIN FERROELECTRICS

Department of Dielectrics
Institute of Physics
Academy of Sciences of the Czech Republic

Supervisor: Ing. Jiří Hlinka, PhD.

Study Programme: 4F3
Physics of Condensed Matter and Material research

Prague, March 2012

I dwelt in a city enchanted,
And lonely indeed was my lot;
. . . .
Though the latitude's rather uncertain,
And the longitude also is vague,
The persons I pity who know not the City
The beautiful City of Prague.

\- William Jeffery Prowse (1836- 1870)
The City of Prague,
("Little Village on Thames")

Acknowledgement

Knowledge is in the end based on acknowledgement.
-Ludwig Wittgenstein (1889- 1951)

Thus, I would like to acknowledge those who made this thesis possible.

First of all, I would like to express my deepest gratitude to my supervisor Ing. Jiří Hlinka, PhD., as my advisor and mentor. As my supervisor he always encouraged and challenged me throughout my work. I am especially grateful for his concern, patience, friendship and amenity.

I am indebted to RNDr. Jan Petzelt DrSc., who gave me this precious opportunity to come to this beautiful city of Prague for my higher studies. He introduced me to the world of ferroelectric perovskite. It is my honor to work with such a well-known scientist..

I am grateful to RNDr. Stanislav Kamba CSc., who offered me the opportunity to learn and work with Infrared measurements with the best laboratory conditions.

It's my pleasure to thank Ing. Ivan Gregora CSc., for assistance and help with Raman and PFM Measurements.

Great thanks to Fedir Borodavka for helping with PFM measurements and Dr. Dmitry Nuzhnyy for discussions and suggestions during the fitting of Infrared data.

Many thanks to all my labmates, Tetyana Ostapchuk, Elena Buixaderas, Victor Bovtun, Veronica Goian, Martin Kempa, Petr Kuzel, Pavel Marton, Petr Ondrejkovic, Maxim Savinov and Vladimir Zelezny for building up a scientific environment, filled with enthusiasm and encouragement.

I would like to thank Mrs. Martina Spanelova who did her best to as the department secretary, making it a very friendly environment to work.

Lastly, I am profoundly grateful to my husband Sibu Simon for his support and care during my doctoral studies and preparation of the thesis. My son Johan Simon participated with me throughout my doctoral studies and thesis writing.

Any acknowledgement will not be complete without acknowledging the Almighty God, who gave the strength, patience and blessing to withstand the pressure during this work.

Declaration

I declare that I carried out this doctoral thesis independently, and only with the cited sources, literature and other professional sources.

I understand that my work relates to the rights and obligations under the Act No. 121/2000 Coll., the Copyright Act, as amended, in particular the fact that the Charles University in Prague has the right to conclude a license agreement on the use of this work as a school work pursuant to Section 60 paragraph 1 of the Copyright Act.

In…..... date..... Signature

Abstrakt

Téma: Spektroskopické studium mřížkové dynamiky feroelektrických látek s hustou doménovou strukturou

Autor: Elizabeth Vakkechalil John

Katedra: Fyzika kondenzovaných látek a materiálový výzkum

Školící pracoviště: Fyzikální ústav AVČR., Na Slovance 2, Praha 8, 182 21, Czech republic.

Vedoucí doktorské práce: Ing. Jiří Hlinka, PhD.., Fyzikální ústav AVČR, Na Slovance 2, Praha 8, 182 21, Czech republic.

Konzultanti: RNDr. Stanislav Kamba CSc., Ing. Ivan Gregora CSc., Fyzikální ústav AVČR, Na Slovance 2, Praha 8, 182 21, Czech Republic.

Abstrakt:

Feroelektrické perovskity obsahující ionty olova mají aplikačně zajímavé fyzikální a strukturní charakteristiky. Je známo, že doménová struktura má zcela zásadní vliv na jejich dielektrické a piezoelektrické chování. Návrhem doménové struktury lze vhodně modifikovat makroskopické tenzorové vlastnosti těchto látek.

Feroelektrické domény hrají také klíčovou roli ve fyzice tenkých epitaxních filmů. V této práci jsme se zaměřili na projevy doménové struktury v tenkých filmech $PbTiO_3$, připravených pomocí chemické depozice z plynné fáze organokovových prekurzorů na různých krystalických substrátech, např. $LaAlO_3$, MgO, $NdGaO_3$, $SrTiO_3$, LSAT, atd. Některé aspekty doménové struktury mohou být odhaleny pomocí infračervené a ramanovské spektroskopie. Rozdíly v doménové struktuře jsou způsobeny různými vlivy, jako například tloušťkou filmu, rozdíly mezi přirozenými mřížkovými parametry vrstvy a podložky, atd. Lokální informaci o architektuře feroelektrických nanodomén v těchto filmech lze získat pomocí rastrovací mikroskopie piezoodezvy (PFM). Detailní studium PbTiO3 filmu na LaAlO3 substrátu umožnilo pozorovat řadu typů doménových uspořádání obsahující kombinace všech 6 typů tetragonálních feroelastických stavů a oba typy kompatibilních doménových stěn (180° a 90° stěny).

Daleká infračervená spektroskopie komplexní permitivity keramiky $PbTiO_3$ nám umožnila demonstrovat existenci několika nových mřížkových módů, tzv. geometrických resonancí. Tyto dodatečné hybridní excitace způsobené nehomogenním dynamickým depolarizačním polem se vyskytují ve spektru společně s dobře známými polárními módy homogenního $PbTiO_3$ krystalu. Srovnání našich experimentů a modelových výpočtů ukazuje, že silné geometrické resonance v okolí 300 a 500 cm^{-1} jsou spojené s přítomností 90° feroelektrických stěn.

V práci byla také studována anizotropie makroskopické dielektrické odezvy piezoelektrických PZT keramik ve fononové frekvenční oblasti, vtisknutá procesem jejich pólování v elektrickém poli. Výsledky studie jsou diskutovány v kontextu příspěvků jednotlivých polárních módů a modelů efektivního makroskopického prostředí.

Klíčová slova: feroelektrické domény, infračervená spektroskopie, ramanovská spektroskopie, zobrazování metodou PFM, tenké filmy, $PbTiO_3$ keramika, PZT

.

Abstract

Title: Spectroscopic investigations of lattice dynamics in multidomain ferroelectrics

Author: Elizabeth Vakkechalil John

Department: Department of Condensed Matter Physics

Institution: Department of Dielectrics, Institute of Physics, AVČR, Na Slovance 2, Praha 8, 182 21, Czech Republic.

Supervisor: Ing. Jiří Hlinka, PhD., Department of Dielectrics, Institute of Physics, AVČR., Na Slovance 2, Praha 8, 182 21, Czech Republic.

Consultants: RNDr. Stanislav Kamba CSc., Ing. Ivan Gregora CSc. Fyzikální ústav AVČR, Na Slovance 2, Praha 8, 182 21, Czech Republic.

Abstract: Lead based ferroelectric perovskites exhibit attractive physical and structural properties. Ferroelectric domains are known to have a very essential impact on dielectric and piezoelectric properties of ferroelectrics. Tailoring of domain structures allows to change the macroscopic symmetry of the material and to purposely modify its average tensor properties.

Ferroelastic domains play also a key role in physics of epitaxial ferroelectric films. Here we studied signature of domain structure in $PbTiO_3$ thin film grown by metalorganic chemical vapor deposition technique on different substrates, namely $LaAlO_3$, MgO, $NdGaO_3$, $SrTiO_3$ (100), $SrTiO_3$ (110), $SrTiO_3$ (111) doped with 0.5% Nb and LSAT. Certain aspects of domain structure can be conveniently revealed by using infrared reflectance and Raman spectroscopic techniques. Differences in domain pattern are associated with different aspects related to the thin film like the film thickness, lattice mismatch between substrate and thin film, etc. A local insight into the complex nanodomain architecture can be seen using piezoresponse force microscopy imaging techniques. A detailed study of 250 nm and 110 nm thick PTO/LAO thin film has shown different patterns of ferroelectric domain structure with all six tetragonal ferroelectric domain states and both 180^0 and 90^0 ferroelectric walls.

The far-infrared reflectance and theoretical investigation of complex dielectric permittivity on $PbTiO_3$ ceramics reveals the presence of several additional modes

identified as the so called geometrical resonances (i.e., extraneous hybrid excitations created by inhomogeneous depolarization fields) besides the well-known polar modes of bulk $PbTiO_3$. A comparison of our experiment and model calculations suggests that the strong geometrical modes located near 300 and 500 cm^{-1} are associated with the presence of 90^0 ferroelectric walls. This work also investigates the anisotropy of the macroscopic dielectric response of poled PZT ceramics in the phonon frequency region, introduced due to the poling processes. The results are discussed in terms of distinct polar phonon contributions and effective medium theory.

Keywords: Ferroelectric domains, Infrared Spectroscopy, Raman Spectroscopy, PFM imaging, $PbTiO_3$ thin films, $PbTiO_3$ ceramics and PZT.

Contents

Acknowledgement v
Declaration vii
Abstrakt (in Czech) ix
Abstract (in English) xi
Index xiii

1 Introduction

1.1 Introduction: Motivation 1
1.2 Domains 3
1.3 Perovskite 4
1.4 Overview of the Thesis 5

2 Basic Concepts

2.1 Lattice Dynamics: Introduction 7
2.2 Infrared Active Phonons 8
2.2.1 Transverse and Longitudinal Phonons 10
2.3 Ferroelectricity 11
2.3.1 Phase Transitions 13
2.3.2 Ginzburg-Landau Theory 14
2.3.2.1 Second-Order Phase Transition 15
2.3.2.2 First-Order Phase Transition 15
2.3.3 The concept of soft mode 16
2.4 Ferroelectric Domains 17
2.4.1 Domain Formation 18
2.4.2 Other types of Domain Walls 19
2.5 Thin Film Technology 22
2.5.1 Substrates 22
2.5.2 Strain in Thin Films 23
2.5.3 Domains in Thin Films 25
2.6 Effective Medium Approximation 25
2.6.1 Bruggeman Effective Medium Approximation 26
2.6.2 Lichtenecker Mixing Formula 27
2.6.3 Arlt and Peusens Model Approximation 27

3 Experimental Techniques

3.1 Introduction 29
3.2 Infrared Spectroscopy 29
3.2.1 Fourier Transform IR Spectrometer 29
3.2.2 Experimental Setup 31
3.2.3 Analysis of Data 33
3.2.3.1 Classical Oscillator Model 34

3.2.3.2 *4*-parameter Model 35
3.2.3.3 Kramers-Kronig Relations 36
3.2.3.4 Thin film fitting Model 37
3.3 Raman Spectroscopy 39
3.3.1 Origin of Raman Spectra: Classical explanation 40
3.3.2 Raman Spectrometer 42
3.3.3 Experimental Setup 44
3.3.4 Analysis of Data 45
3.4 Piezoresponse Force Microscopy (PFM) 46
3.4.1 Basic Principle of PFM 46
3.4.2 PFM imaging modes 48
3.4.3 Piezoresponse Force Microscope 49

4 Lead Titanate Ceramics

4.1 Introduction- $PbTiO_3$ 51
4.2 $PbTiO_3$ ceramics 54
4.2.1 PFM Measurements 54
4.2.2 IR Measurements 55
4.2.3 Effective Medium Approximation- Theoretical Approach 58
4.3 Discussion 60

5 Lead Titanate Thin Films

5.1 Introduction 63
5.2 Preparation of Epitaxial Thin Films 64
5.3 Substrates used for PTO Thin Films 66
5.3.1 Lanthanum Aluminate, $LaAlO_3$ (100) 66
5.3.2 $(La,Sr)(Al,Ta)O_3$ (100) 69
5.3.3 Magnesium Oxide (100) 71
5.3.4 $NdGaO_3$ 72
5.3.5 Strontium Titanate $SrTiO_3$ (100), (110) and 0.5% Nb doped (111) 75
5.4 Film Thickness 78
5.5 Discussion and conclusion 79

6 Lead Titanate Thin Films on Lanthanum Aluminate Substrate

6.1 Introduction 83
6.2 Analysis of IR spectra of the 250 nm thick film 83
6.2.1 Fit using Classical Oscillator Model 84
6.2.2 Fit using *4*-Parameter Model 85
6.2.3 *4*-Parameter fitting model using parameters of $PbTiO_3$ ceramics 86
6.2.4 Temperature Dependence 87
6.3 PFM Investigations of the 250 nm thick film 91
6.4 IR Data Analysis of the 110 nm thick film 94
6.4.1 Low Temperature IR Measurements 94

6.5 PFM data Analysis 97
6.6 Effective Medium Approach 98
6.7 Discussion 99

7 Poled Lead Zirconate Titanate

7.1 Introduction 101
7.2 Sample Used 102
7.2.1 Poling 103
7.3 IR Measurements 104
7.3.1 Temperature Measurements 107
7.4 Raman Measurement 109
7.5 Discussion 110

8 Conclusions 113

9 Future Works 117

Bibliography 119

List of Tables 126

List of Abbreviations 127

List of Variables 128

List of Publications 130

CHAPTER 1 Introduction

1.1 Introduction: Motivation

The nature has wide resources to support the necessities of mankind. Investigation into the different phenomena of nature was of prime interest during all times. Discovery of ferroelectricity by J. Valasek (1921)[1] in Rochelle salt has opened a new era of materials with ferroelectric properties. Ferroelectric materials are widely used for application as sensors and actuators in electromechanical systems.[2] The major part of non-volatile memory prepared for computer memory industry uses ferroelectric materials.[3, 4] Figure 1.1 shows the demand of ferroelectric materials and its applications.

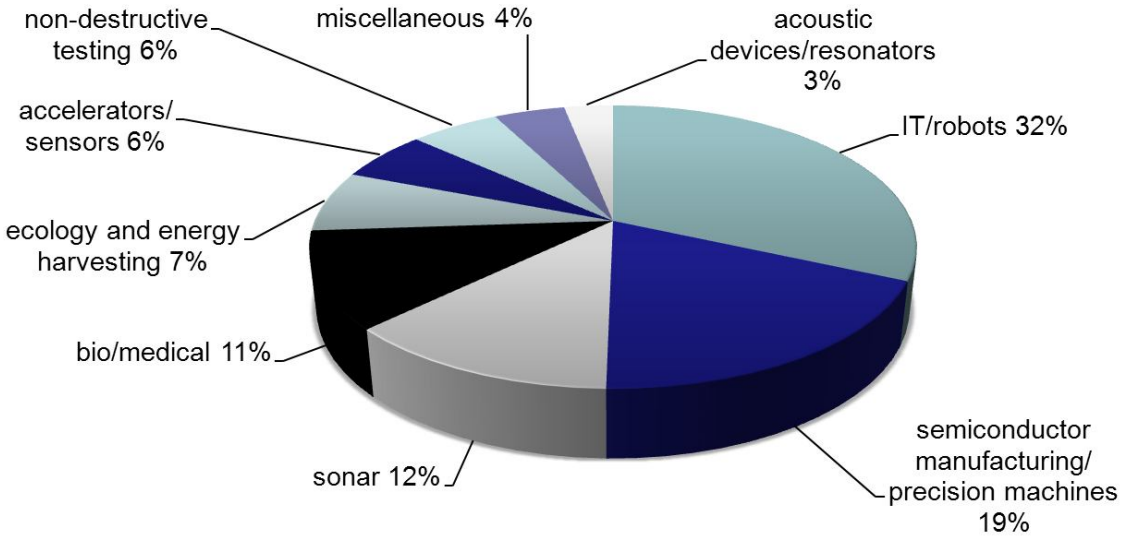

Figure 1.1. Diversified market of ferroelectric materials with piezoelectric properties[5].

Ferroelectric materials are dielectric materials having pyroelectric[i] and piezoelectric[ii] properties. Ferroelectric materials are polar crystals[iii], with spontaneous polarization (P_S)[iv], such that the polarization can be switched[v] and forms hysteresis loop where polarization varies according to the applied electric field. High permittivity and

[i] Pyroelectric property is the change in polarization due to the change in temperature.
[ii] Piezoelectric property is the appearance of strain (deformation) due to the applied electric field.
[iii] Polar crystals have electric dipole moment associated with them even in the absence of an external field.
[iv] Spontaneous polarization is the electric polarization a material possesses even in the absence of electric field.
[v] Polarization switching is the process of switching the spontaneous polarization by applying electric field, magnetic field, stress, etc.

low dielectric losses make the ferroelectric material suitable for wide range of applications.

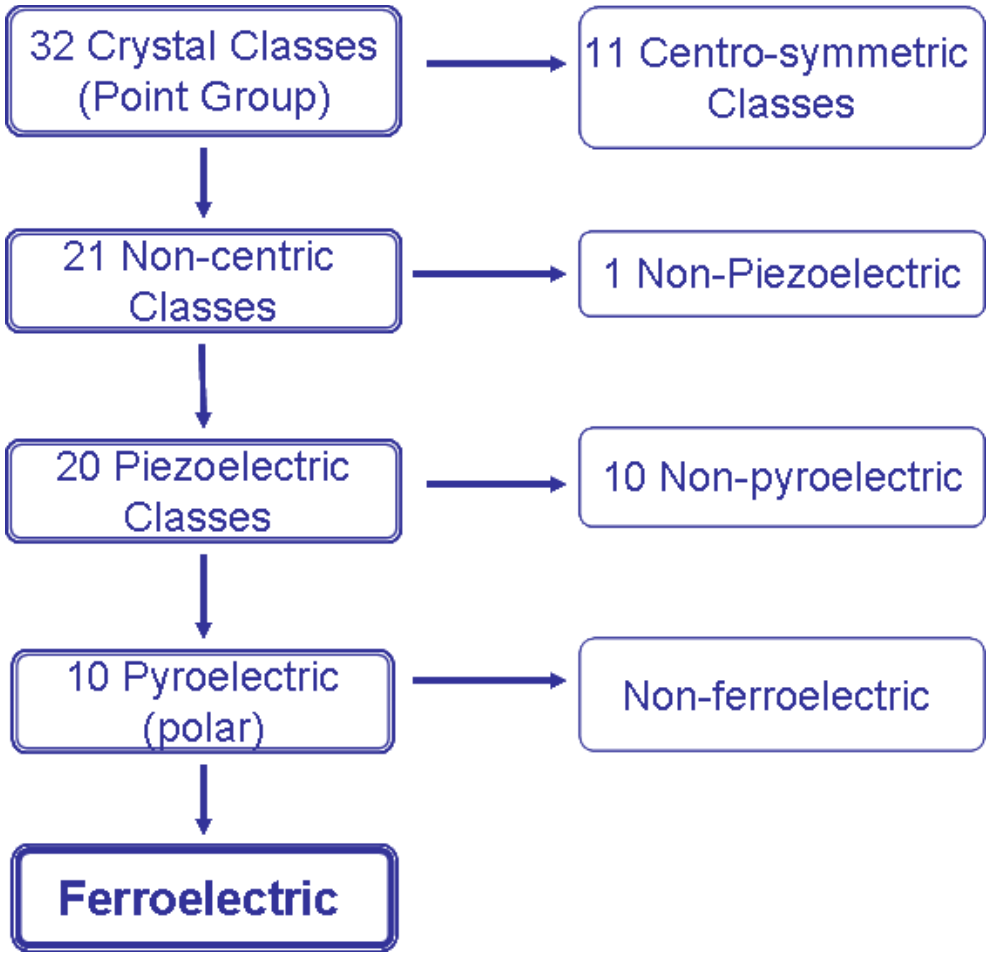

Figure 1.2. A classification scheme for the 32 crystallographic point groups.

Ferroelectricity being a symmetry based phenomenon can be studied as a sub-class among the 32 point groups symmetry as shown in figure 1.2. Out of the 32 point symmetry group, only 21 are non-centrosymmetric groups. Here 20 of the non-centrosymmetric groups have piezoelectricity effect. Among the 20 non-centrosymmetric groups, 10 are pyroelectric that exhibit spontaneous polarization property. All pyroelectric materials do not show polarization reversal as the ferroelectric materials. Thus all ferroelectric materials are pyroelectric but not all pyroelectric materials are

ferroelectric. The polarization reversal characteristic for ferroelectric materials is related to the domain[vi] pattern.

1.2 Domains

Systematic and in-depth study of the domains and their behavior with respect to temperature, electric field, pressure, etc., will help to understand ferroelectric materials with ease.[6] The domains can be engineered to modulate the ferroelectric properties. Various phenomena associated with the ferroelectric domains like domain formation, types of domains, domain wall movement, twinning, etc., will help to understand these systems in nature.[7]

Further investigations towards the miniaturization and price reduction have developed thin films with properties as or better than their bulk counterparts. Literature shows that ferroelectricity was observed in $BaTiO_3$ (BTO) thin films between two metallic $SrRuO_3$ electrodes in short circuit down to about 6 unit cell, that is ≈24 Å.[8] The application of ferroelectric thin films in the field of microelectronics, sensors, piezoelectric devices, etc., has successfully overcome the challenges of this century.[2, 9,10] Various phenomena like stress and strain, domain formation, defects, grain size effects, etc., formed during the process of thin film preparation influence their properties.[2, 11]

Theoretical predictions show that the domain formation in $PbTiO_3$ (PTO) films is a process of stress relaxation[12]. The domain configuration can be predicted as a function of lattice mismatch and temperature.[13,14,15,16] Domains formed during the process of stress relaxation in the ferroelectric thin films influence the physical properties such as dielectric, piezoelectric and optical ones.[13,17,18] Three- dimensional polarization imaging in epitaxial polydomain ferroelectric thin film was performed to explain why the ferroelectric domain structure is formed at/and/below the cubic-to-ferroelectric phase transition (PT).[19]

Different experimental techniques are widely used to study the properties of domains in thin films. Various scanning probe techniques such as voltage modulated scanning force microscopy[19], force microscopy[20], friction microscopy[21], scanning force microscopy[22, 23], etc., have been successfully used to peep into the domain structure

[vi] Ferroelectric domains are regions where the spontaneous polarizations are uniformly directed.

formed in epitaxial ferroelectric thin films. Domain evolution in ferroelectric epitaxial thin films can be studied by X-ray diffraction (XRD)[24]. We shall show that the spectroscopy is also a suitable tool for studying the domain structure and its transformation.

1.3 Perovskite

Perovskite materials, first discovered by L. A. Perovski in 1839, have the general chemical formula ABO_3.[25] Here 'A' and 'B' are cations, with 'A' larger than 'B' and O_2 is the anion that bonds to both cations. The typical perovskite structure is shown in figure 1.3. In a cubic unit cell, type 'A' atom sits in the corner positions (0, 0, 0), type 'B' cation occupies the body centered position (½, ½, ½) and oxygen atom occupies the face centered positions (½, ½, 0).

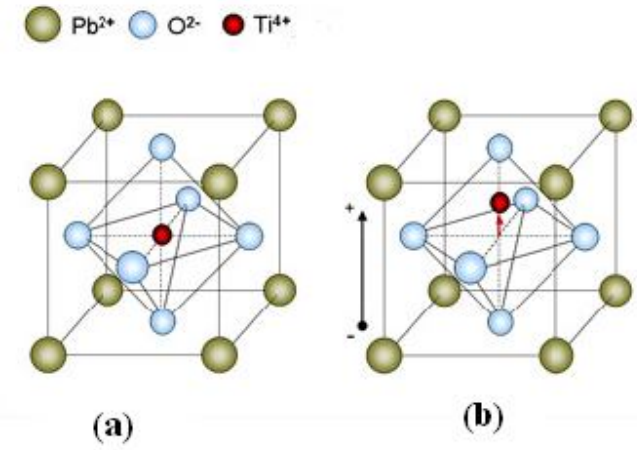

Figure 1.3. Structure of a perovskite with the chemical formula ABO_3. The green spheres are the 'A' atoms (a large metal cation, such as Pb^{2+}, Ba^{2+}), the red spheres are the 'B' atoms (a smaller metal cation, such as Ti^{4+}) and the blue spheres are the oxygen atoms. (a) Cubic structure and (b) tetragonal structure with Ti^{4+} displaced giving it an elongation along c axis.

Most of the useful ferroelectrics, such as BTO, PTO, strontium titanate $SrTiO_3$ (STO) etc., have the perovskite structure. The perovskite structure is very tolerant to the cation substitution into the 'A' and 'B' positions giving rise to many ferroelectric perovskite materials with wide properties. Compounds with such compositions as: $Pb(ZrTi)O_3$, $(LaNa)TiO_3$, $(BaCa)(TiZr)O_3$, $(BaSr)TiO_3$, $(BaSr)TiO_3$, $(NaBi)TiO_3$, $([NaBi]Ba)TiO_3$, etc., also belong to perovskite family.

The ideal cubic perovskite crystal structure has three triply degenerate zone-center modes, which are infrared (IR) active modes of F_{1u} symmetry. The first mode, called the Last-mode[26] (expected at the lowest frequencies in PTO) has the oscillation of A-cation

against the BO_6 octahedra framework. The second mode, called the Slater mode[27] corresponds to mutual B vs. rigid O_6 oscillations. The high frequency IR active mode called Axe mode[28] corresponds to the bending of the O_6 octahedra. Last, Slater and Axe modes are shown in figure 1.4 a, b and c respectively.[29]

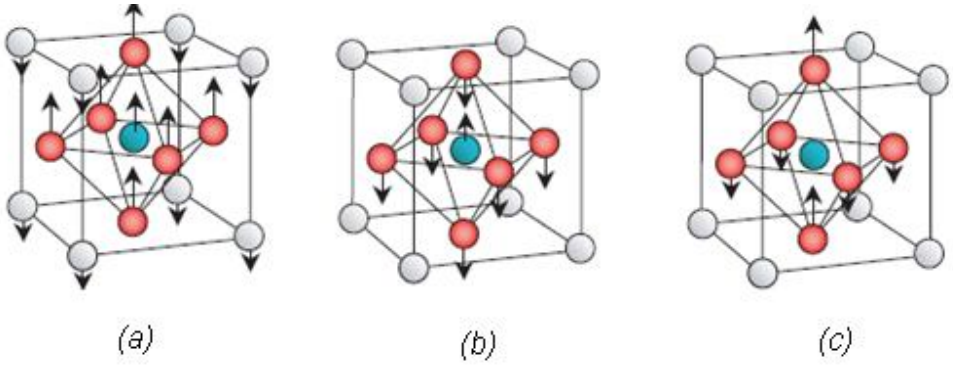

Figure 1.4. Eigen-displacements (normal co-ordinates) of (a) Last, (b) Slater and (c) Axe zone-center modes in $PbTiO_3$[29].

1.4 Overview of the Thesis

This doctoral work presents the report on investigations of phonon modes and domain structure in PTO ceramics, PTO thin films and PZT ceramics. The content is arranged as follows:

Chapter 2 is dedicated to the basic concepts regarding the IR active phonons, lattice vibrations, ferroelectricity, ferroelectric domains, thin film technology etc.

Chapter 3 describes the experimental techniques used for our investigation of the phonon modes and domain structure, such as IR spectroscopy, Raman spectroscopy and Piezoresponse Force Microscopy (PFM) imaging.

In Chapter 4 we present the attempts of detailed investigation of PTO ceramics using terms of PFM imaging, IR spectroscopy and domain structure.

Chapter 5 gives an overview and a preliminary report of PTO thin films epitaxially grown on different substrates namely LAO, LSAT, MgO, NGO, STO (100), STO (110) and STO (111) doped with 0.5% Nb.

Chapter 6 presents studies of PTO thin films grown on LAO substrates of two thicknesses, namely 250 nm and 110 nm, done using IR spectroscopy, Raman spectroscopy and PFM imaging. Among others, it includes description of data evaluation strategy and application of effective medium approximation.

Chapter 7 is devoted to investigations of the anisotropy appeared in PZT ceramics due to electric poling. The influence of poling and depoling on far-infrared response is studied using IR spectroscopy.

Chapter 8 concludes the observations and results reported in this work.

Chapter 9 takes the reader into the future, listing the future work that can be done on the above mentioned samples.

Figure 1.5 gives the schematic diagram on the layout of this work.

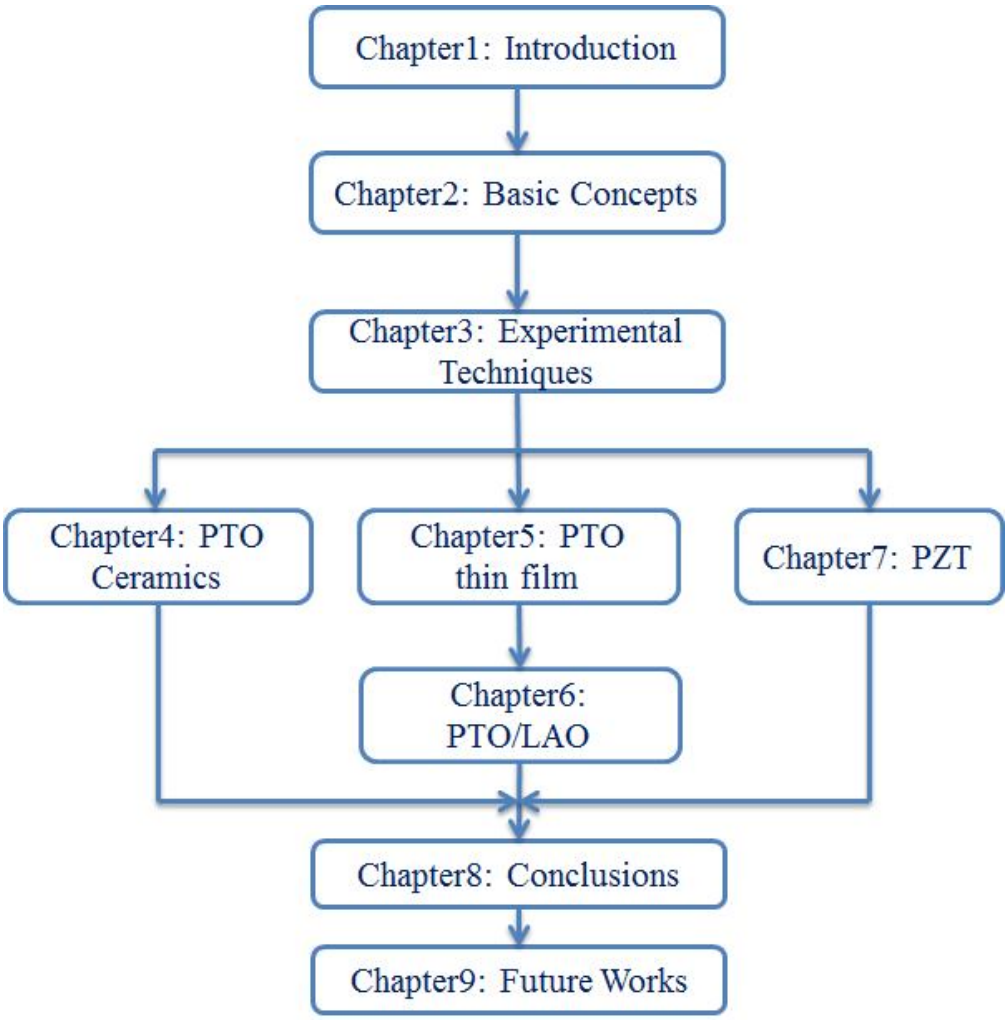

Figure 1.5: Schematic diagram on the overview of the thesis.

CHAPTER 2 Basic Concepts

2.1 Lattice Dynamics: Introduction

Crystals have a unique arrangement of atoms exhibiting long range order and symmetry. Lattice specifies the periodic array of the atoms. Any point in a lattice can be described by the vector $\boldsymbol{r}$,

$$\boldsymbol{r} = n_1\boldsymbol{a} + n_2\boldsymbol{b} + n_3\boldsymbol{c} \tag{2.1}$$

where n_1, n_2 and n_3 are the arbitrary integers and $\boldsymbol{a}$, $\boldsymbol{b}$ and $\boldsymbol{c}$ are the translation vectors.

A primitive unit cell is the smallest repeating unit of the lattice. It is characterized by the three lattice constants (in 3-dimensions) namely a, b and c which gives the length of basic vector and α, β and γ angles which separate these vectors from one another.[30] Figure 2.1 shows the structure of a unit cell where a, b, and c are the unit cell length and α is angle between b and c, β is angle between a and c and γ is angle between a and b.

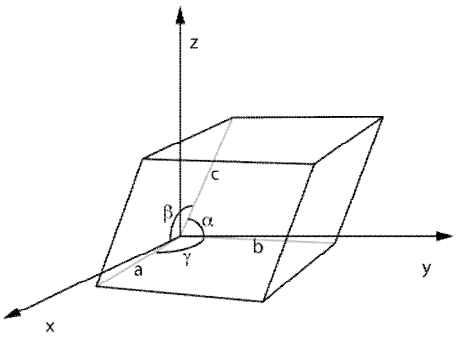

Figure 2.1. Unit cell with lattice parameters a, b, c and angles α, β, γ.

Lattice dynamics is the study of vibration of atoms in a crystal. This is the basis for many macroscopic properties like specific heat, dielectric properties, interaction with radiation (infrared absorption, Raman scattering), structural PT, etc.

Thermal excitation can induce interatomic motion in lattice which is a collective phenomenon. The lattice vibrations in which all atoms move with the same frequency and phase are called *normal modes*. Quantized lattice vibrations are called *phonons* that are bosons possessing zero spin and obey Bose-Einstein statistics like in the case of photons.

The modes that interact directly with light are called IR active. The phonon frequencies are related to the wavevector $\boldsymbol{K}$ through *dispersion relation* given as $\omega=\omega_i(\boldsymbol{K})$. This can be plotted in *Brillouin zone*. In a crystal with N unit cells, three branches of the dispersion relation are translational and zero for $\boldsymbol{K}$=0 are called acoustic branches and the remaining 3N-3 branches are called optical branches. For acoustic

branch the atoms in a unit cell vibrate in the same direction and for optical branch the atoms in the unit cell vibrate in opposite direction as in figure 2.2.[32]

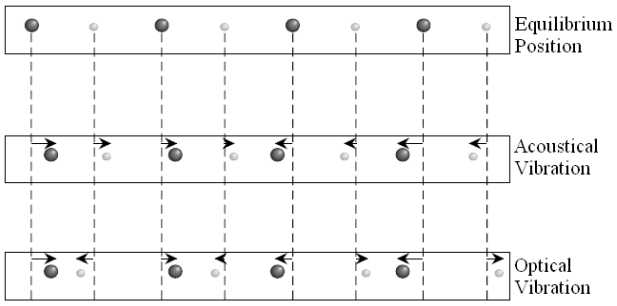

Figure 2.2. Schematic representation of acoustic and optical vibrations. In acoustic vibration atoms in a unit cell vibrate in the same direction, while for optical vibration the atoms in a unit cell will move in opposite directions.

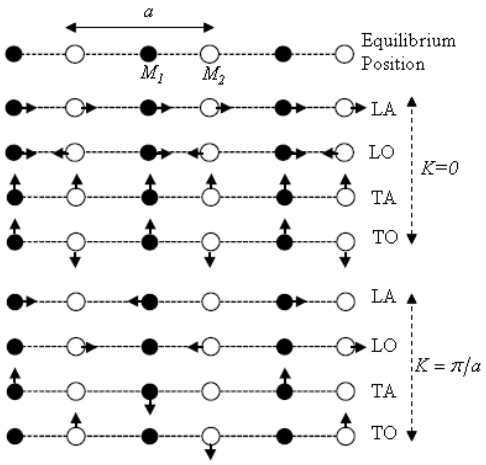

Figure 2.3. Atomic displacement pattern of a diatomic chain for transverse and longitudinal modes at Brillouin zone boundary.

Transverse and longitudinal motion of atoms are associated with acoustic and optical vibrational branches known as transverse acoustic (TA), longitudinal acoustic (LA), transverse optical (TO) and longitudinal optical (LO) modes. Figure 2.3 shows the atomic displacement pattern of a diatomic chain for transverse and longitudinal modes at Brillouin zone boundary.[33]

2.2 Infrared Active Phonons

In ionic crystals, the optical phonons may correspond to mode of vibration where the positive and negative charged ions move in opposite direction developing a macroscopic dipole moment in the crystal. Such modes couple directly with the electromagnetic field of IR radiation. Thus optical phonons are able to absorb and reflect light and become IR active. This process is shown in figure 2.4.

Here the dispersion of light showed by dotted lines has a constant slope given by $v = c/n$, where n is the complex refractive index. In order to have the same frequency and wavevector for photon and phonons, the dispersion curves must be intersect each

other. Since $c/n >> v_s$, where v_s is the velocity of sound in the medium, the only intersection point for the acoustic branch occurs at the origin, while for optical branch the interaction occurs at finite angular frequency shown by a circle in figure 2.4. As the optical branch is flat, for small *K* the resonance is equal to the frequency of the optical mode at *K*=0.[34]

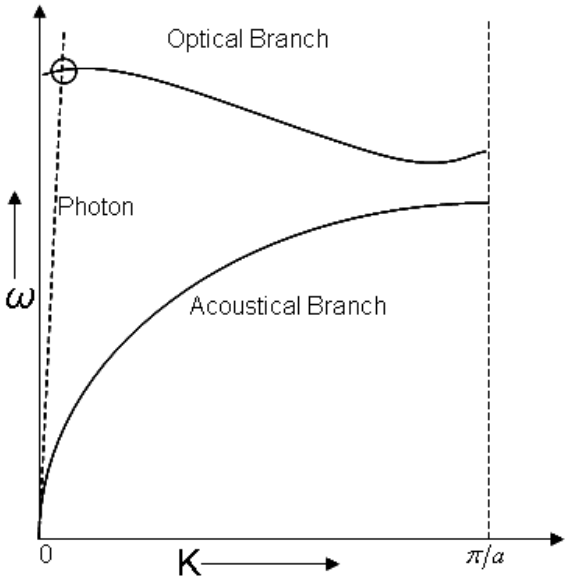

Figure 2.4. Dispersion curve for the acoustic and optical phonon branch in a typical crystal with a lattice constant a. The dispersion of the photon waves is shown by the dotted lines.

In reality the vibration modes are anharmonic. Consider the simple case of displacement of the positive and negative ions in TO mode in opposite direction. If *x* is the relative displacement of the positive and negative ions within their unit cell, the atoms sit in a potential well of the form[34]

$$U(x) = C_2 x^2 + C_3 x^3 + C_4 x^4 + \ldots \qquad (2.2)$$

In equation (2.2) the term with x^2 is the harmonic term, leading to harmonic oscillator equation of motion with a restoring force $-dU/dx$ proportional to $-x$. The anharmonicity allows the phonon-phonon scattering process. Thus phonons have finite lifetime (τ_p) and thus lattice vibrations are not travelling infinitely through the crystal. Thus lattice vibrations can be treated as damped harmonic oscillators due to anharmonicity, which accounts for the *damping* (γ) of the modes. The damping term has an effect of reducing the peak absorption coefficient and broadening the absorption line.

2.2.1 Transverse and Longitudinal Phonons

Considering an ionic crystal with two or more types of atoms in the unit cell, the magnitude of time varying dipole is given by:

$$p(t) = qx(t) \tag{2.3}$$

where *x(t)* is the time varying displacement of the ion (atom) from the equilibrium position and q is the (transverse) effective charge. The atom absorbs energy (IR absorption) when the oscillating dipole frequency ω_{TO} is equal to the frequency ω of the external electromagnetic wave.

The equation of motion for the displaced atom as the TO phonon interacts with the IR light is given as[34]:

$$\frac{d^2x}{dt^2} + \gamma \frac{dx}{dt} + \omega_{TO}^2 x = \frac{q}{\mu} E \tag{2.4}$$

where γ is damping, k is the restoring constant, μ is the reduced mass, $\omega_{TO} = (k/\mu)^{1/2}$ is the TO resonance frequency and E is the electric field due to the IR light. The complex dielectric function is given as:

$$\varepsilon_r(\omega) = \varepsilon_\infty + \frac{Nq^2}{\varepsilon_0 \mu} \frac{1}{\omega_{TO}^2 - \omega^2 - i\gamma\omega} \tag{2.5}$$

where ε_∞ is the high frequency dielectric constant and N is the number of unit cells per unit volume.

It is useful to introduce so-called *oscillator strength* f and a dimensionless quantity $\Delta\varepsilon$, usually called *dielectric contribution* or a *dielectric strength*,

$$\Delta\varepsilon = \frac{f}{\omega_{TO}^2} = \frac{1}{\omega_{TO}^2} \frac{Nq^2}{\varepsilon_0 \mu} \tag{2.6}$$

At zero frequency, we have thus

$$\varepsilon_0 = \varepsilon_\infty + \Delta\varepsilon \tag{2.7}$$

where ε_0 is the static dielectric constant. Thus the classical dielectric function becomes

$$\varepsilon_r(\omega) = \varepsilon_\infty + \Delta\varepsilon \frac{\omega_{TO}^2}{\omega_{TO}^2 - \omega^2 - i\gamma\omega} \tag{2.8}$$

In the medium with no free charges:

$$\nabla . D = \nabla . (\varepsilon_0 \varepsilon_r E) = 0 \tag{2.9}$$

where D is the electric displacement, $\boldsymbol{E}$ is the electric field strength, ε_o is the electric permittivity and ε_r is the relative dielectric constant. Equation (2.9) has two solutions:

i. for transverse waves that propagate in a direction perpendicular to $\boldsymbol{E}$, $\nabla.\boldsymbol{E} = 0, \varepsilon_r = 0$

ii. for longitudinal waves that propagate in a direction parallel to $\boldsymbol{E}, \nabla.\boldsymbol{E} \neq 0$, thus $\varepsilon_r = 0$. Thus the dielectric function (eq. 2.8) becomes zero for longitudinal waves.

$$\varepsilon_\infty + \Delta\varepsilon \frac{\omega_{TO}^2}{\omega_{TO}^2 - \omega_{LO}^2} = 0 \tag{2.10}$$

The TO-LO splitting of a polar vibrational mode is related to the oscillator strength as:

$$\frac{\omega_{LO}^2 - \omega_{TO}^2}{\omega_{TO}^2} = \frac{\Delta\varepsilon}{\varepsilon_\infty} \tag{2.11}$$

Combination of equations (2.7) and (2.9) gives the *Lyddane- Sachs- Teller (LST) relation*.

$$\frac{\varepsilon_o}{\varepsilon_\infty} = \frac{\omega_{LO}^2}{\omega_{TO}^2} \tag{2.12}$$

Summing up the ionic susceptibilities of independent oscillators that vibrate along a given polarization, gives the classical dispersion model as:

$$\varepsilon = \varepsilon_\infty + \sum_j \Delta\varepsilon_j \frac{\omega_{TOj}^2}{\omega_{TOj}^2 - \omega^2 - i\nu_{TOj}\omega} \tag{2.13}$$

The LST relation can be generalized for N atoms as[34, 35, 36]

$$\frac{\varepsilon_o}{\varepsilon_\infty} = \prod_j \frac{\omega_{LOj}^2}{\omega_{TOj}^2} \tag{2.14}$$

2.3 Ferroelectricity

Ferroelectric materials are polar materials that exhibit spontaneous polarization Ps which can be switched from one equilibrium state to another by applying suitable electric field. Switching of polarization and domain wall in ferroelectric materials by applying electric field gives ferroelectric ***P-E*** hysteresis loop. A Sawyer-Tower circuit[37] can give hysteresis loop for ferroelectric materials as shown in figure 2.5(a).

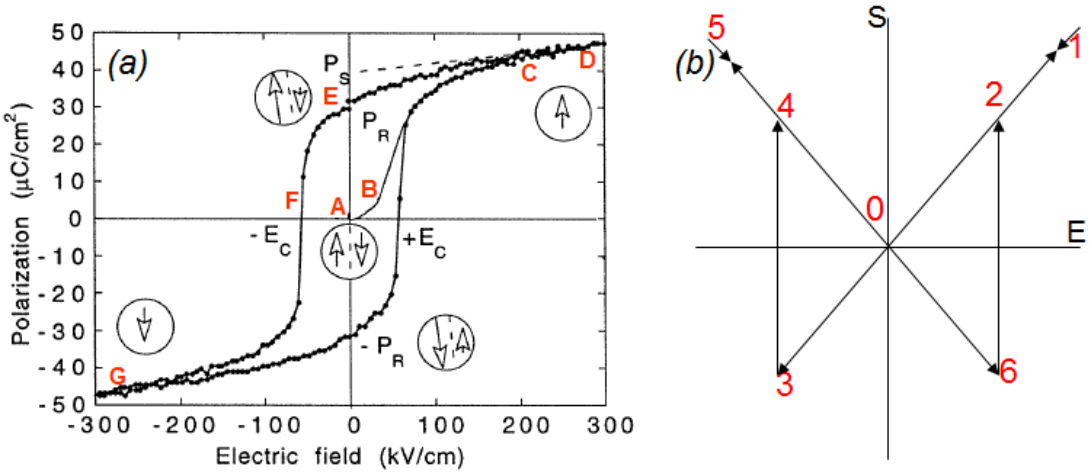

*Figure 2.5. (a) Ferroelectric **P**-E hysteresis loop. Circles with arrows represent the polarization state of the materials at the indicated fields. This loop is measured on a (111)-oriented 1.3 μm thick sol-gel $Pb(Zr_{0.45}Ti_{0.55})O_3$ film. (b) Idealistic strain-electric field (x-E) hysteresis loop in which polarization is reversed by 180°*[17].

By applying a small electric field, the segment AB in figure 2.5 shows linear growth of polarization with the field. In this region, the field is not strong enough to switch the domain states. IR field strengths fall in this region. As the field is still increased (the segment BC), the domains with unfavorable direction of polarization will start to switch along the crystallographic direction that is close to the direction of the field. All domains are aligned in the same pattern at the point C, further they follow a linear pattern as segment CD. When the field starts to reverse (point E), the domains tend to switch back. When the applied field is zero, the polarization is non-zero (point P_R) called the *remanent polarization* as some of the domains are switched back. The field necessary to bring the polarization to zero is called *coercive field* (E_c) (point F). Point G is reached as the field is still increased in the negative direction. Here the domains are aligned in the opposite direction as it was at point C. The field is increased in positive direction to complete the hysteresis loop.

In ferroelectric materials, the polarization switching by electric field is also related to strain-electric field (*S-E*) hysteresis loop, which resembles the shape of a butterfly as shown in figure 2.5(b). This is due to the converse piezoelectric effect of the lattice, and due to switching and movement of domain walls. The quadratic *S-E* hysteresis loop can be understood with respect to the *P-E* hysteresis loop. At point 0 the strain is taken as zero. The straight portions 1-3 and 5-6 are the true piezoelectric

component of strain and its slope gives the piezoelectric modulus, d_{33}. At points 3 and 6, the coercive field is reached and the field is large enough to switch the direction of polarization. During the field cycling the remanent strain is observed at zero field (point 0), if domains in general do not switch to their original position at zero field.[36,38] For the experimentally observed butterfly loop to be straight, nonhysteretic lines, the single–domain state must be reached by high electric field. As for polydomain crystals the strain from movement of domain walls is strongly nonlinear and hysteretic.

2.3.1 Phase Transitions

Ferroelectric materials undergo structural PT as they pass from high-temperature paraelectric phase to low-temperature ferroelectric phase. These PTs can be associated with changes in the dimension or shape of the crystal unit cell (cubic, tetragonal, rhombohedral, etc.), with strong anomalies in dielectric and thermal properties, domain formation, etc. The paraelectric phase has no spontaneous polarization (Ps) and is rarely polar. In this thesis we shall consider perovskite ferroelectrics where the paraelectric phase is cubic. Figure 2.6 shows the example of different structural transformations as the perovskite material passes from paraelectric to ferroelectric phases.

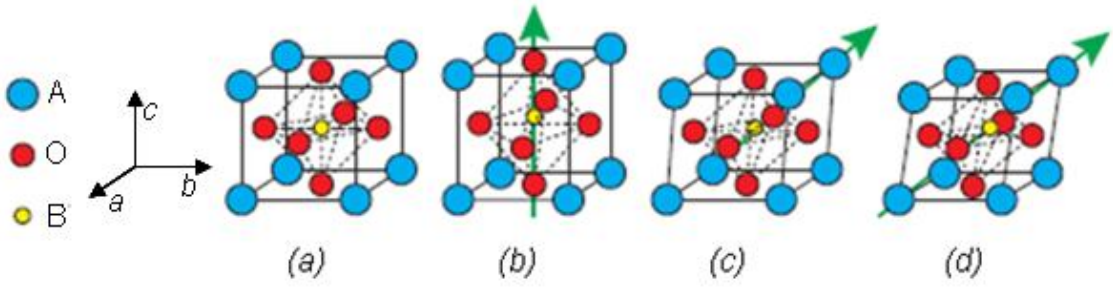

Figure 2.6: Perovskite unit cell in (a) cubic structure, (b) tetragonal structure, (c) orthorhombic structure and (d) rhombohedral structure.

In cubic structure $a = b = c$ and the angle α between axis b and c, angle β between axis a and c, and angle γ between axis a and b are 90^o. As the temperature is lowered, for instance, in BTO, it undergoes a series of PT like tetragonal, orthorhombic and rhombohedral. In tetragonal phase there is an elongation along c axis, i.e. [001] direction and the angle between the axes remains the same. In orthorhombic structure the

elongation is along the [110] directions and a = c>b. In rhombohedral phase $a = b = c$ with unit cell distorted along [111] direction.

The number of domain states in each ferroelectric phase varies according to the energetically equivalent directions of the Ps. The possible direction of Ps in tetragonal, orthorhombic and rhombohedral phases is given in figure 2.7.

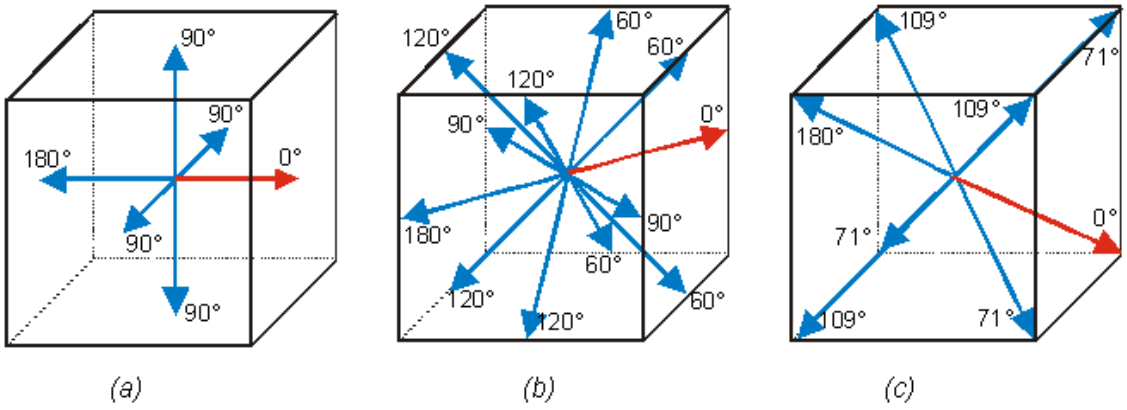

Figure 2.7. Directions of Ps in (a) tetragonal phase, (b) orthorhombic phase and (c) rhombohedral phase. Angles between polarization direction '0' and its symmetry equivalent ones are indicated[39].

2.3.2 Ginzburg-Landau Theory

The properties of ferroelectric materials can be treated on macroscopic scale considering the laws of thermodynamics. The simplest Landau theory at E=0 describes the ferroelectric material in terms of free energy F expanded in power of polarization $\boldsymbol{P}$ (primary order parameter), as a polynomial expansion given as:

$$F = F_0 + \frac{a}{2}P^2 + \frac{b}{4}P^4 + \frac{c}{6}P^6 + \ldots \tag{2.15}$$

where P is independent part of the free energy, b and c are constants and coefficient a is considered to be linear function of temperature:

$$a = \frac{T - T_0}{C} \tag{2.16}$$

where T is temperature, T_0 is transition temperature and C is Curie constant and b, c can be considered as temperature independent parameters. The equilibrium is determined by the condition $\frac{\partial F}{\partial P} = 0$ [40, 41, 42].

2.3.2.1 Second-Order Phase Transition

For the Landau coefficient $b > 0$, the c and higher terms in equation (2.15) may be neglected and the equilibrium condition:

$$\frac{T - T_0}{C} P + bP^3 = 0 \tag{2.17}$$

leads to a second-order PT. Indeed for $T > T_0$, the ferroelectric material is in paraelectric state with the free energy having only one stationary point at $P = 0$, as given in figure 2.8. In ferroelectric phase $T < T_0$, the state P=0 becomes a local maximum and there appears two degenerate minima with equal $P \neq 0$ states. The Ps is obtained in the absence of electric field as $P_s^2 = -a/b$, so that:

$$T > T_C,\ P_s = 0 \tag{2.18}$$

$$T < T_C,\ P_s = \sqrt{-a/b} \tag{2.19}$$

The dielectric susceptibility is given as:

$$\text{for } T > T_C,\ \chi = \frac{C}{T - T_0} \tag{2.20}$$

$$\text{for } T < T_C,\ \chi = \frac{C}{2(T_0 - T)} \tag{2.21}$$

Thus susceptibility diverges at T_0 as seen in the figure 2.8 (c).

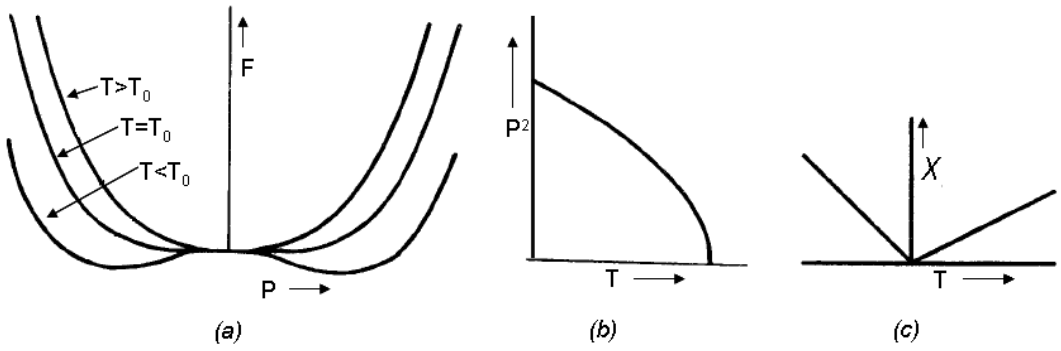

Figure 2.8. Summary of properties of second-order PT with respect to (a) free energy, (b) temperature dependence of polarization and (c) temperature dependence of reciprocal susceptibility[40].

2.3.2.2 First- Order Phase Transition

When the Landau coefficient $b < 0$ and $c > 0$, the equilibrium free energy expansion describes a first-order PT. The equilibrium condition can be written as:

$$\frac{T - T_0}{C} P + bP^3 + cP^5 = 0 \qquad (2.22)$$

The transition (Curie) temperature at which free energies of paraelectric and ferroelectric phases are equal occurs at:

$$T_c = T_0 + \frac{3b^2}{16ac} \qquad (2.23)$$

At $T = T_C$, $P_s^2 = \frac{-3b}{4c}$. Thus the order parameter and susceptibility are discontinuous at T_0 as shown in figure 2.9.

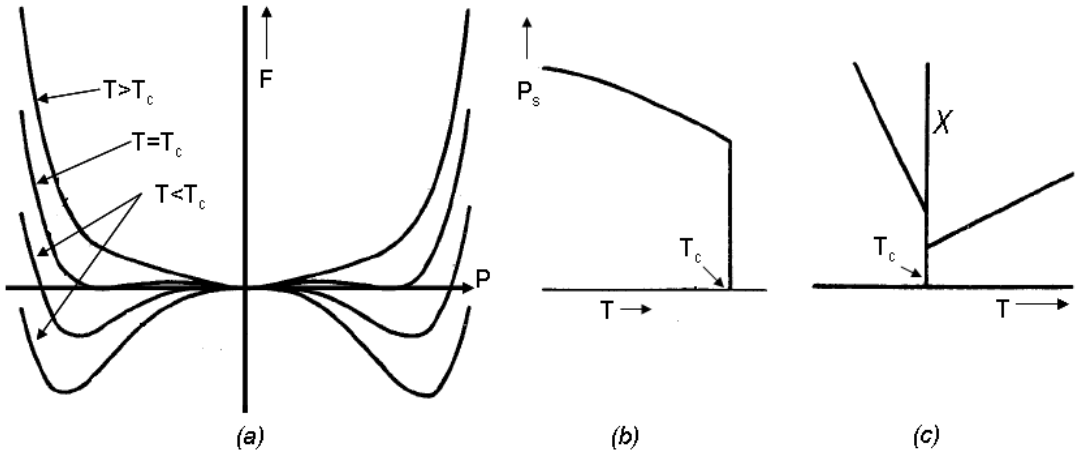

Figure 2.9. Summary of properties of first-order PT with respect to (a) free energy, (b) temperature dependence of polarization and (c) temperature dependence of reciprocal susceptibility[40].

2.3.3 The Concept of Soft Mode

Soft mode is the lowest optical mode whose eigen frequency approaches zero (softens) at a critical temperature as the temperature is reduced.[43] This happens e.g. if the short-range interaction force is compensated by the long-range Coulomb force, the frequency of the soft TO phonon converges to zero at T_c, leading to an instability of the crystal lattice with respect to the soft TO phonon. In this case, the phase transition is called a displacive phase transition. In cubic perovskite, one of the F_{1u}(TO) phonons is responsible for the *displacive ferroelectric* PT.[51] Due to the relative displacement of cations and anions, the soft mode induces a non-vanishing polarization ***P***. A divergence in static permittivity is also related to soft mode. Cochran law for soft mode frequency ω_{SM} is given as

$$\omega_{SM}^2 = A(T - T_c) \tag{2.24}$$

where T_c is the critical Curie temperature and A is a constant. The soft mode is IR active for proper ferroelectric transitions where the order parameter is polarization. Thus the IR oscillator strength assumed as

$$f_{SM} = \Delta\varepsilon_{SM}\omega_{SM}^2 \tag{2.25}$$

is temperature independent across the PT. The static permittivity of the ferroelectric is proportional to Curie-Weiss law, thus from LST relation (equation 2.14)

$$\varepsilon(0) = \varepsilon(\infty)\frac{\omega_{LO}^2}{\omega_{TO}^2} \propto \frac{1}{T - T_c} \tag{2.26}$$

Thus the temperature of ε(0) can be predicted from soft mode temperature dependence if the longitudinal frequency is temperature independent.

In order-disorder system the anharmonicity is higher. In paraelectric phase the atoms hop among different possible minima of the potential well. As the temperature is lowered across the PT temperature, the atoms stay in one of the minima giving a more ordered structure with lower entropy in ferroelectric phase.

The contribution of hopping of ions to dielectric relaxation below the polar phonon frequencies is explained by *Debye model*. The equation of motion of such dielectric relaxation process usually in the microwave (MW) or THz range is given by:

$$\frac{dp}{dt} + \frac{1}{\tau}p = fE \tag{2.27}$$

where f is the oscillator strength having effective charge and effective mass of the mode and τ is the relaxation time of the order parameter. The permittivity is given as:

$$\varepsilon_1(\omega) = \frac{\Delta E}{1 + iw\tau} + \varepsilon_\infty \tag{2.28}$$

In many cases the soft mode is coupled to an additional low energy mode is called *central mode*.[46] The central mode rises mainly due to the anharmonicity of the lattice.[47]

2.4 Ferroelectric Domains

In ferroelectric phase, domains are formed because the Ps can have at least two possible equivalent directions. Thus the energy degeneracy of different directions of Ps leads to the appearance of ferroelectric domain structure.[39] Inside a domain the polarization is homogeneous. The adjacent domains are separated by domain walls lets

consider tetragonal BTO. The 180° domain wall separates the domains with Ps of opposite direction. The 90° domain wall separates the domains which have their Ps at 90° and is accompanied by a rotation of the spontaneous strain tensor.[48] Thus the 90° domain wall is ferroelectric and ferroelastic, whereas 180° domain walls are only ferroelectric in character as they do not have spontaneous strain tensor rotation across the domain wall.[48] In some ferroelectric materials both 180° and 90° domains are seen simultaneously, for example the domain structure is called Herring- bone type structure. The different types of domains are shown in figure 2.10.

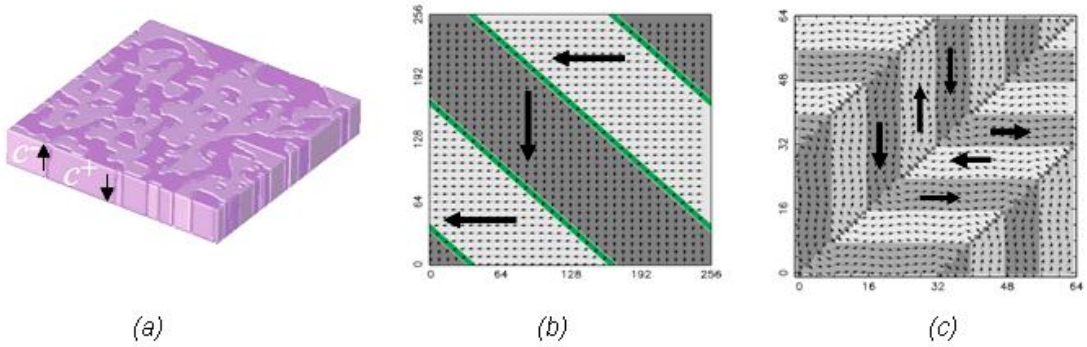

Figure 2.10. Types of domain structure (a) 180° domain, (b) 90° domain and (c) Herring-bone type structure both 180° domain and 90° domain

2.4.1 Domain Formation

Perovskite ferroelectric materials are generally ferroelastic also. Thus the angle by which the Ps rotates at the domain wall can characterize whether the domain wall is only ferroelectric or also ferroelastic. For a tetragonal crystal the domains can be ferroelectric and ferroelastic giving rise to four types of simple domain structures namely 180° *a-a* domain, 180° *c-c* domain, 90° *a-c* domain and 90° a_1-a_2 domain structure. The vertical and lateral Piezoresponse Force Microscopy (PFM) helps to visualize all types of domains.[49] As epitaxial thin film is strained and clamped by the substrate, ferroelastic domains are formed.[18,50] The different domain patters corresponding to ferroelectric crystals and thin films are shown in figure 2.11.

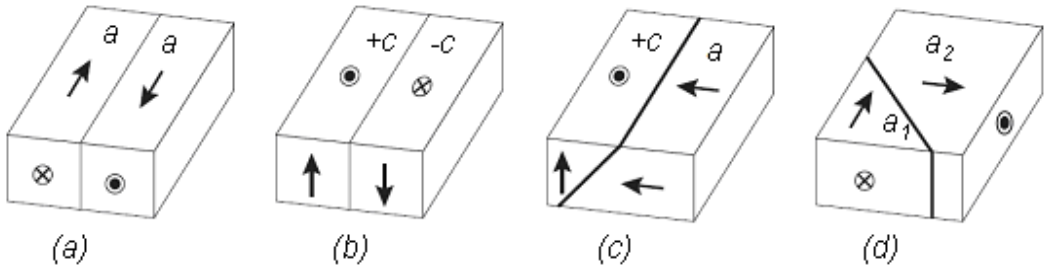

Figure 2.11. Domain structures formed in tetragonal crystals: (a) 180° a-a domain, (b) 180° c-c domain, (c) 90° a-c domain and (d) 90° a_1-a_2 domain structure [50].

In ferroelectric ceramics during PT the grains are clamped, thus the stress plays an important role in the domain formation and 90° domains are preferred. The domain width w is related to the grain size a_g in the case of fine grained ceramics as $w \sim \sqrt{a_g}$.[52] Similarly the domain width in thin films is obtained as $w = \sqrt{d_f}$ where d_f is the film thickness.[53]

2.4.2 Other types of Domain walls

In tetragonal phase 90° and 180° domain walls are found, while in orthorhombic and rhombohedral phases other angles are also possible. In orthorhombic phase, the domains can exist at 60°, 90°, 120° and 180°, while in rhombohedral phase the domains exist at 71°, 109° and 180°. This is because the Ps is oriented along the cubic face diagonals and body diagonals of the unit cell in orthorhombic and rhombohedral phase respectively (see fig 12). It is seen also from the Ginzburg-Landau expansion that there can be six equivalent domain positions in tetragonal phase, twelve in orthorhombic and eight in rhombohedral phase.[39]

Domain walls can appear only along planes on which the spontaneous deformation of two neighboring domains fit to each other. Planes satisfying this condition are known as permissible walls[54, 55]. There are different types of permissible domain walls namely $W\infty$ walls with arbitrary orientation, and crystallographically prominent domain walls W_f and S walls, whose indices depend on P_S and the electromechanical coefficient[54].

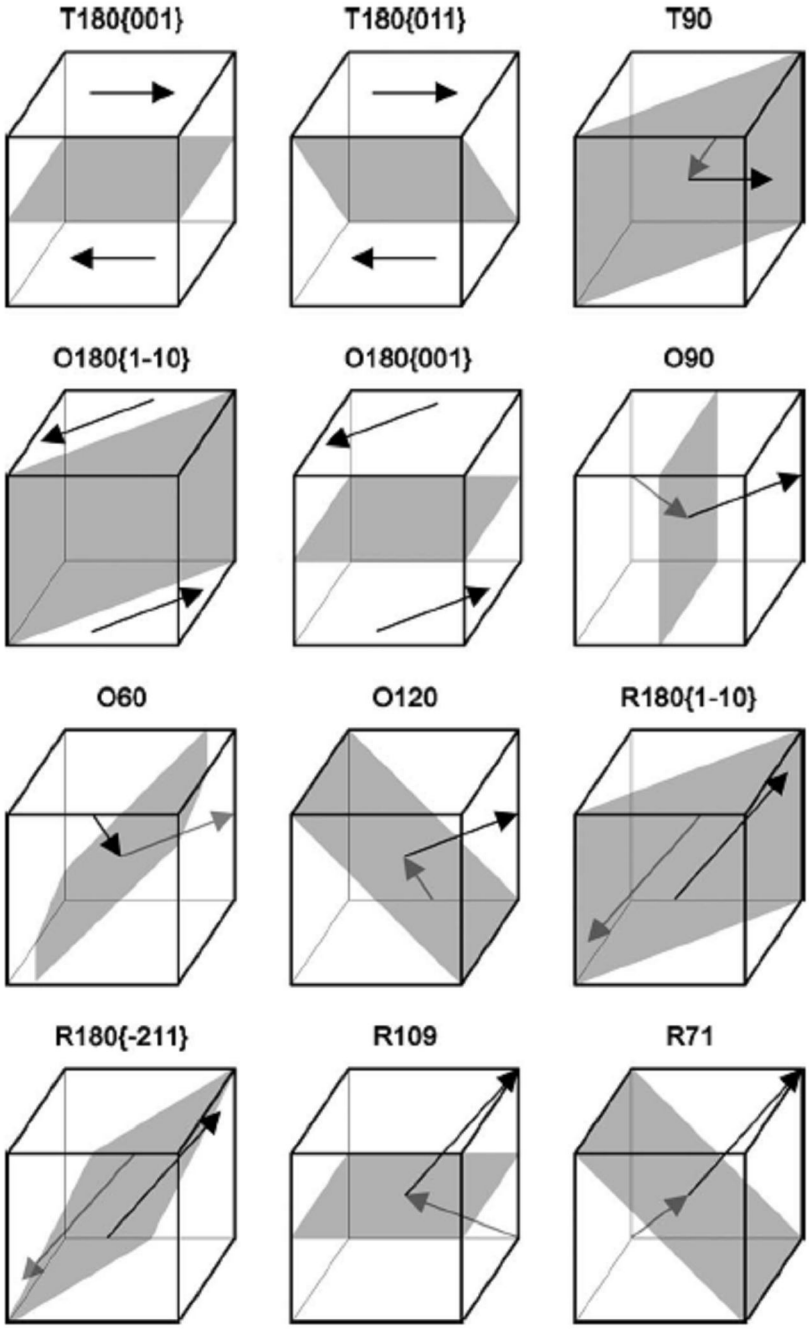

Figure 2.12. Set of mechanically compatible and electrically neutral domain walls in the three ferroelectric phases of $BaTiO_3$. In the case of 180^0 domain wall, where the orientation is not uniquely determined, walls with the most important crystallographic orientations are displayed[39].

The set of mechanically compatible and electrically neutral electric domain walls possible for tetragonal, orthorhombic and rhombohedral phases in BTO is given in figure

2.12. The mechanical compatibility obviously allows the 180° W_∞ walls in all three phases namely tetragonal, orthorhombic and rhombohedral. In addition to it, in tetragonal phase the 90° W_f-type domains exist, which are either neutral (head-to-tail) or charged (head-to-head or tail-to-tail). In orthorhombic phase, the domain walls can be formed at 60° with charged W_f -type walls and neutral S-type walls. The domain walls are formed also at charged or neutral 90° and 120° W_f walls and charged S walls in orthorhombic phase. In rhombohedral phase a pair of charged and neutral W_f-type domain walls can be formed with the angle between the polarizations as 109° or 71°.[39]

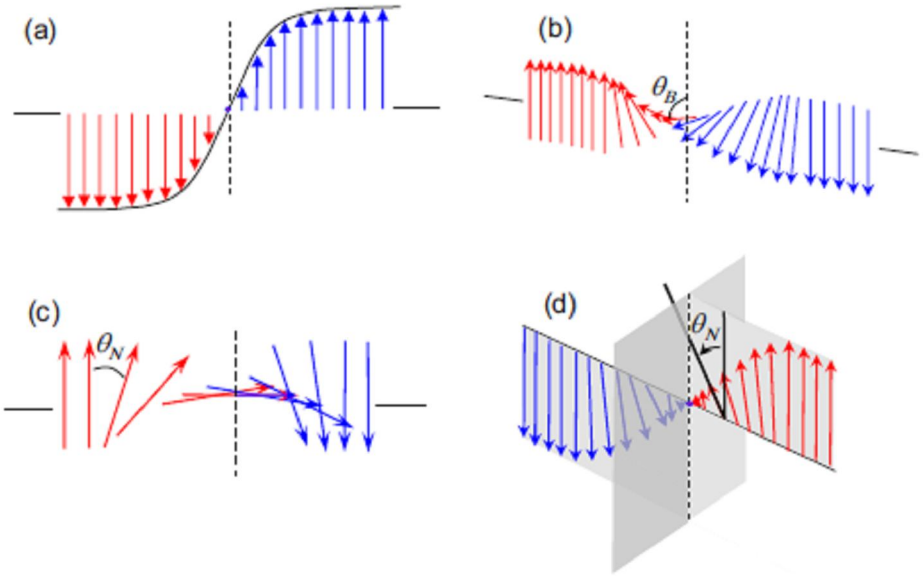

Figure 2.13. Different types of 180° domain walls: (a) Ising type, (b) Bloch type, (c) Neel Type and (d) mixed Ising-Neel type[56].

The polarization change is an interesting phenomenon that takes place at the domain wall. In the case of 180° magnetic domain walls the polarization reversal can be either rotated in the plane parallel to the domain wall called Bloch like or normal to the domain wall called Neel like. Here the domain wall thickness is >10nm. The ferroelectric 180° domain wall is predominantly Ising-type. Figure 2.13 show the different types of polarization reversal near 180° domain wall.

In the case of 90° domain wall the polarization reversal is expected as shown in figure 2.14.

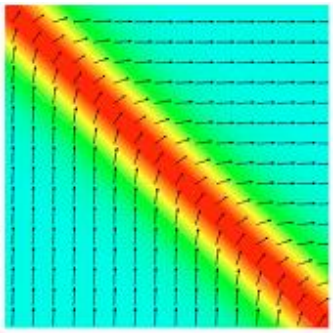

Figure 2.14. Polarization change at 90^o domain wall.

2.5 Thin Film Technology

The conventional belief that the best properties for ferroelectrics were obtained for single crystal was challenged by the synthesis of thin films on appropriate substrates. Ferroelectric thin films can exhibit properties like dielectric, pyroelectric, piezoelectric and electro-optic better than their bulk counterparts.[57] The strain induced in the thin film can tune the properties like ferroelectricity[58], transition temperature (up to few hundreds of degrees), etc.[28, 60] Ferroelectric thin films tend to form domains in order to reduce the strain.[33] Figure 2.15 shows the internal structure of a coherent epitaxial thin film. Here the substrate and the film have perovskite structure and the ferroelectric film is biaxially strained to match with the substrate giving a coherent epitaxial film.

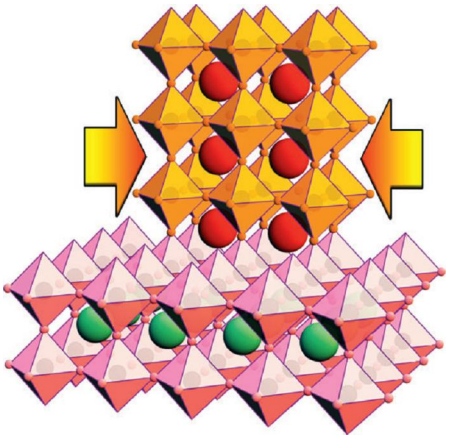

Figure 2.15. Schematic diagram showing the biaxial strain on the thin film to match the underlying [62].

2.5.1 Substrates

Substrates play a significant role in the thin film preparation as they are the platform to grow thin film. In epitaxial thin film, the mismatch between the lattice

constant of substrate and the thin film is responsible for inducing the desired strain. For the ferroelectric thin films with perovskite structure, the best way is to have perovskite substrate. Figure 2.16 shows commercially available perovskite substrates with their pseudocubic *a*-axis lattice spacing against the popular perovskite thin films. The lattice constant of rare-earth scandate (*Re*ScO_3) substrates are higher than the other available perovskite substrates.

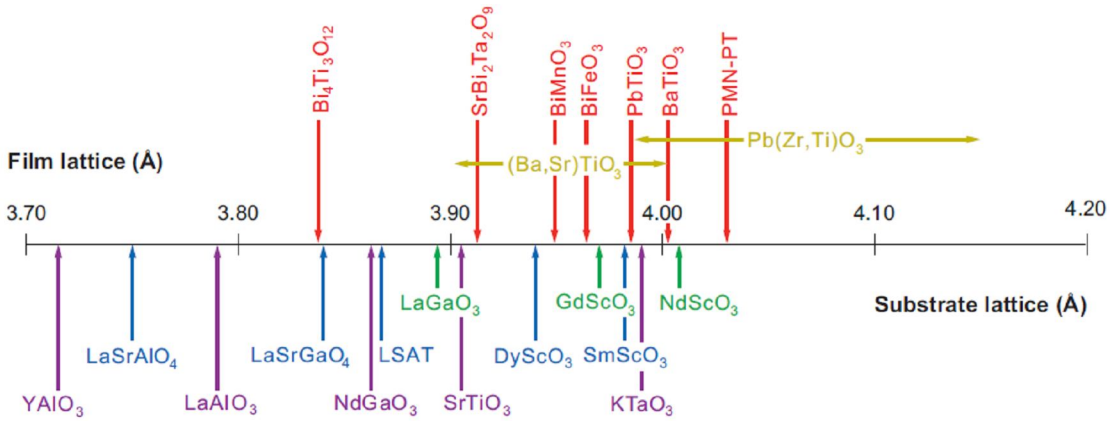

Figure 2.16. Comparison between the pseudocubic a-axis lattice spacing of thin films (above the number line) and substrates (below the number line).[62]

Ferroelectric thin film like PTO grown on different substrates like (001) $LaAlO_3$ [a_{LAO} = 3.789 Å], (001) STO [a_{STO} = 3.905 Å], (001) MgO [a_{MGO} = 4.212 Å], R-cut sapphire [a_{SAPH} = 3.5 Å], (110) $NdGaO_3$ [a_{NGO} = 5.431 Å], single crystal $KTaO_3$ [a_{KTO}=3.9885 Å], fused quartz substrate etc., show remarkable difference in their features like XRD, Raman spectra, domain structure, strain, etc .[61, 63, 64, 65, 66, 67, 68, 69, 70, 71, 72, 73]

2.5.2 Strain in Thin Films

Strain is developed in the thin film due to the mismatch in lattice constant, film deposition method and subsequent cooling, thermal properties, etc. Film strain has high influence on the domain structure formation, nature of PT, electrical, optical and mechanical properties. Strain is also sensitive to deposition methods and experimental conditions.

Epitaxial strain (also called misfit strain) results from the lattice mismatch between the substrate and the thin film.[70] The epitaxial strain can be given as

$$\varepsilon_s = \frac{(a_s - a_f)}{a_s} \tag{2.29}$$

where a_s and a_f are the lattice parameter of substrate and film, respectively. As the substrate is much thicker than the film, the film develops *tensile strain* in the $\varepsilon_s > 0$, and *compressive strain* if $\varepsilon_s < 0$, without considering structural relaxation. It is seen that the *tensile strain* in the PTO film shifts the *E*(TO) hard and soft modes towards lower wavenumber for different substrate.[70]

The transformation *strain* developed during the transition from high-temperature cubic phase to low-temperature tetragonal phase is given as:

$$\begin{aligned} \varepsilon_{xx} = \varepsilon_{yy} &= \frac{[a(T) - a(C)]}{a(C)} \\ \varepsilon_{zz} &= \frac{[c(T) - a(C)]}{a(C)} \end{aligned} \tag{2.30}$$

where *a(T)* and c*(T)* are the lattice parameters in tetragonal phase and *a(C)* is the lattice parameters in cubic phase.

The film experiences *thermal strain* due to the thermal expansion mismatch between the film and the substrate. At cubic phase, if T_p is the processing temperature and T_{FPT} is the ferroelectric PT temperature, the thermal strain can be given as

$$\varepsilon_T = [\alpha_f(C) - \alpha_s]\Delta T \tag{2.31}$$

where $\Delta T = (T_p - T_{FPT})$ and $\alpha_f(C)$ is the thermal expansion coefficient of film in cubic phase and α_s is the thermal expansion coefficient of the substrate. In tetragonal phase the thermal strain can be given as:

$$\varepsilon = [\alpha_f(T) - \alpha_s]\Delta T \tag{2.32}$$

Here temperature change $\Delta T = (T_{FPT} - T_{RT})$, such that T_{RT} is the room temperature (R*T*), $\alpha_f(T)$ is the thermal expansion coefficient of the film in tetragonal phase.[73]

Residual strain at room temperature, defined as the sum of all strains exerted by the substrate to film during the process of film preparation, is partially relaxed with increasing film thickness.[70] The thin film tries to relax the strain by domain structure formation, dislocations at and below paraelectric to ferroelectric PT.[75, 77]

2.5.3 Domains in Thin Films

Domain formation is a process of strain relaxation in the film. Strain relaxation by misfit dislocation is a temperature dependent process giving the temperature dependent stability map (figure 2.17).[12] The misfit dislocation formation becomes favorable as the film is grown beyond its critical thickness. Usually the film is grown on the substrate of thickness ranging from 1000 Å - 1 μm, this is much higher than the critical thickness given for different popularly used substrates given in figure 2.17. Considering the role of thermal expansion, if there is only misfit relaxation at growth temperature, *c*-domains are formed for $\alpha_b > \alpha_p$ (where α_b and α_p are the thermal expansion coefficient of the substrate and paraelectric film, respectively). On the other hand *a*-domains are formed as $\alpha_b < \alpha_p$. Among the different experimental techniques, voltage-modulated scanning force microscopy and PFM can be used to image ferroelectric domains to high resolution.[19, 78.]

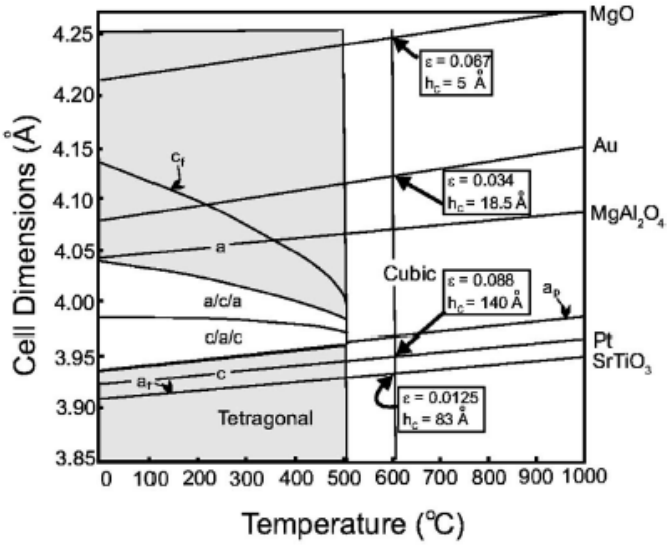

Figure 2.17. Coherent temperature dependent domain stability map for PTO including the cubic lattice parameter for several common single crystal oxide substrates. The misfit strain ε_m for epitaxial growth of PTO at 600^{0}C is included in the inset along with the critical thickness h_c for misfit dislocation formation[12].

2.6 Effective Medium Approximation

The IR reflectivity spectra of various ferroelectric materials can be better understood by considering the local anisotropy associated with the ferroelectric materials due to the domain formation. Since the domains have smaller wavelength than the IR radiation, the *Effective Medium Approach* can be used to analyze the anisotropy (ε_{33} parallel and ε_{11} perpendicular to local polarization) associated with the domain formation

in phonon dispersion region.[81,82] Thus the macroscopic permittivity associated with ferroelectric ceramics and thin films with grains and/or domains can be approximated using simple mixing formulas like Bruggeman effective medium approximation[83], Lichtenecker approach[84] and Arlt and Peusens model approximation[85, 86,87].

2.6.1 Bruggeman Effective Medium Approximation

The homogeneous (averaged) effective dielectric function ε_{eff} is given in terms of reflectivity as[88]:

$$R = \left| \frac{\sqrt{\varepsilon_{eff}} - 1}{\sqrt{\varepsilon_{eff}} + 1} \right|^2 \tag{2.33}$$

The effective medium approximation gives the ε_{eff} in terms of Bruggeman symmetrical formula for binary composite as:

$$\frac{2}{3}\frac{\varepsilon_{11} - \varepsilon_{eff}}{\varepsilon_{11} + \varepsilon_{eff}} + \frac{1}{3}\frac{\varepsilon_{33} - \varepsilon_{eff}}{\varepsilon_{33} + \varepsilon_{eff}} = 0 \tag{2.34}$$

The ε_{33} component can be calculated e.g. from the factorized form of the damped harmonic oscillator model:

$$\varepsilon_{33} = \varepsilon_{\infty 33} \prod_j \frac{\omega_{LOj33}^2 - \omega^2 + i\omega\gamma_{LOj33}}{\omega_{TOj33}^2 - \omega^2 + i\omega\gamma_{TOj33}} \tag{2.35}$$

where ω_{TOj33}^2 and ω_{LOj33}^2 are the transverse and longitudinal frequency of the j^{th} polar phonon, respectively, and γ_{TOj33} and γ_{LOj33} denote their corresponding damping constants. The second component ε_{11} in equation (2.34) can be defined similar by the equation (2.35).

$$\varepsilon_{11} = \varepsilon_{\infty 11} \prod_j \frac{\omega_{LOj11}^2 - \omega^2 + i\omega\gamma_{LOj11}}{\omega_{TOj11}^2 - \omega^2 + i\omega\gamma_{TOj11}} \tag{2.36}$$

The ε_{33} corresponds to A_1 mode and ε_{11} corresponds to E modes in tetragonal perovskites.[89]

The Bruggeman effective medium approximation can also be written in terms of complex permittivity function ε_{11} and ε_{33} as[87]:

$$\varepsilon_{eff} = \frac{1}{4}(\varepsilon_{11} + \sqrt{\varepsilon_{11}^2 + 8\varepsilon_{33}\varepsilon_{11}}) \quad (2.37)$$

2.6.2 Lichtenecker Mixing Formula

Lichtenecker mixing formula is used to obtain effective macroscopic properties in a range of composite materials. Here we use it to obtain the macroscopic permittivity of a ceramic or thin film having grains or domain structure, using the parameters obtained for the corresponding single crystal. Lichtenecker mixing formula is given as:

$$\varepsilon_{eff} = \sqrt[3]{\varepsilon_{33}\varepsilon_{11}^2} \quad (2.38)$$

Here ε_{11} and ε_{33} are the ordinary and extraordinary components of complex permittivity function.[84]

2.6.3 Arlt and Peusens Model Approximation

Arlt and Peusens (1980) suggest that the effective permittivity of coarse grain ceramics of BTO must have characteristics of 90^0 twinning, giving rise to Arlt and Peusens model approximation for macroscopic permittivity. This is applicable for so-called α-type domain configuration, where the 90^0 and 180^0 domains form a mixed wall of alternating stripes as shown in figure 2.20.[85, 86] The thin layered domains separated by 90^0 walls are piled up to form sloped stacks of kind S_1 and S_2. The characteristics of this α-structure are as follows.

1. Macroscopic strain is compensated.
2. Domains having polarization parallel to *z*-axis have half the thickness of the other domains.
3. The average polarization of the structure is $P_\alpha = \sqrt{2}P_s/3$, where P_α is the average polarization along $[\bar{1}10]$ direction.

Out of 24 possible domain states possible in α-type domain configuration, each grain is assumed to have only one domain configuration. Arlt and Peusens (1983) calculated the effective dielectric constants of stacks S_1 and S_2 separately, with the co-ordinate system rotated to x', y and z', with domain thicknesses d_1 and d_2, such that $d_1=d_2/2$.

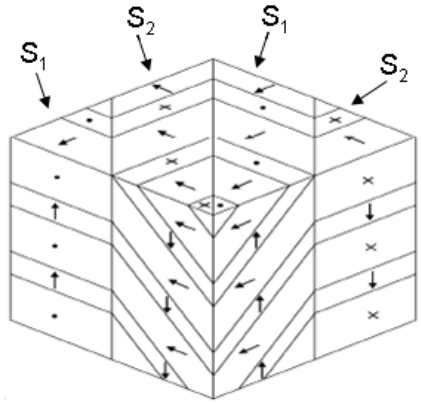

Figure 2.20. Spatial domain configuration (α-type) in large grains of $BaTiO_3$[85].

Now consider the stacks S_1 and S_2 as two homogeneous layers. The complex dielectric tensor is obtained as:

$$\varepsilon_{1\bar{1}0} = \frac{1}{9}\left[\frac{2\varepsilon_{33}^2 + 11\varepsilon_{11}\varepsilon_{33} + 5\varepsilon_{11}^2}{(\varepsilon_{11} + \varepsilon_{33})}\right] \tag{2.39}$$

and

$$\varepsilon_{111} = \frac{3\varepsilon_{11}\varepsilon_{33}}{2\varepsilon_{11} + \varepsilon_{33}} \tag{2.40}$$

Here $\varepsilon_{1\bar{1}0}$ and ε_{111} are the principal components of the effective dielectric tensor of the α-type domain configuration. Arlt and Peusens (1983) use an approximation, similar to Bruggeman effective medium approximation given as:

$$\varepsilon_{eff} = \frac{1}{4}(\varepsilon_{1\bar{1}0} + \sqrt{\varepsilon_{1\bar{1}0}^2 + 8\varepsilon_{1\bar{1}0}\varepsilon_{111}}) \tag{2.41}$$

giving the average dielectric constant ε_{eff} of the macroscopically isotropic ceramics.[85,87]

CHAPTER 3 Experimental Techniques

3.1 Introduction

The theoretical predictions and considerations about ferroelectricity, perovskite, phonons, domains, etc. need to be studied experimentally to understand the underlying facts more clearly. Experimental techniques like IR spectroscopy, Raman spectroscopy and PFM, used to study the thin film are discussed in details.

3.2 Infrared Spectroscopy

The IR spectral range can be divided as Far IR (FIR) in the range 10-200 cm^{-1}, Middle IR (MIR) in the range 200-3000 cm^{-1} and Near IR (NIR) in the range 3000-12800 cm^{-1}. The Fourier transform (FT) IR (FT-IR) spectrometer measures in the FIR and MIR spectral range.

3.2.1 Fourier Transform IR Spectrometer

The FT-IR spectrometer is a Michelson interferometer with two mirrors, one of the two fully reflecting mirror is movable, allowing a variable delay (in the travel time of the light) to be included in one of the beam. Figure 3.1 shows the outline of Michelson interferometers undergoing FT to get IR spectrum.

In FT interferometer each wavelength produces its own characteristic interference pattern when the difference of optical path changes as the movable mirror is shifting. The resulting signal called interferogram is the recording of the signal vs. path difference. By means of the FT, the spectrum is obtained in the output as signal vs. frequency. The effect of applying FT to interferogram is shown in figure 3.2.

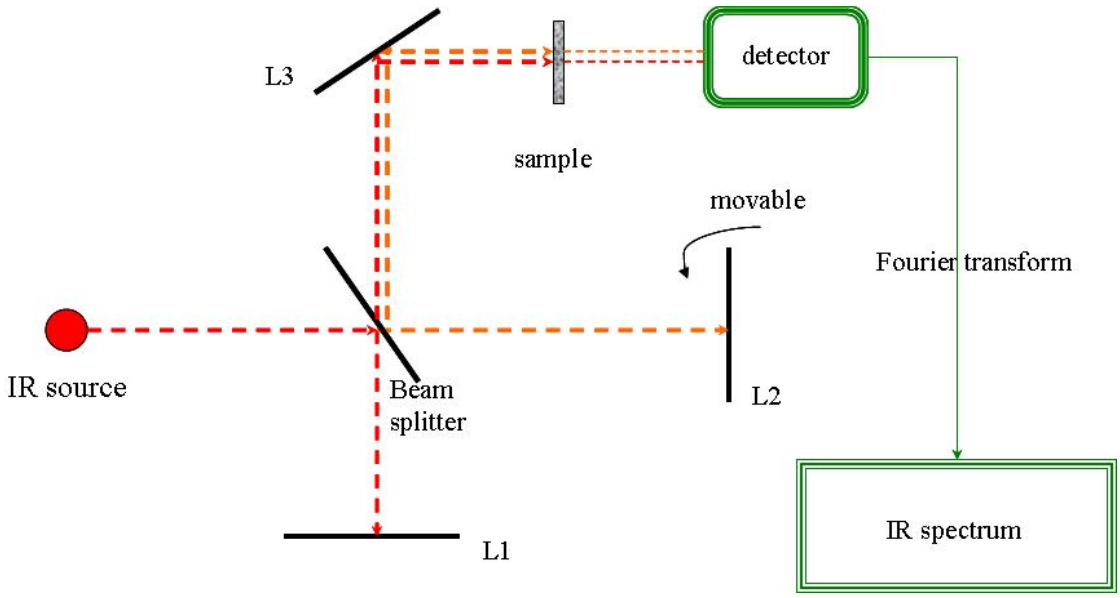

Figure 3.1. Schematic view of a simple Michelson interferometer. The beam from the source (Hg arc lamp) is divided by the beam splitter. One arm of the interferometer consists of a fixed mirror (L1) and the other arm consists of movable mirror (L2). The two beams are recombined at the beam splitter, and then proceed to the sample area and detector.

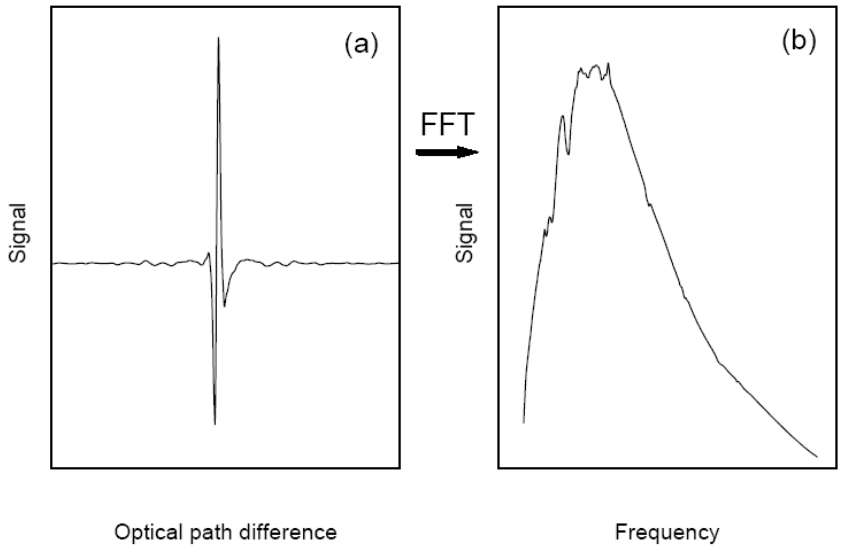

Figure 3.2. The characteristic frequency spectrum of the sample is obtained by converting the interferogram by Fourier transformation.

3.2.2 Experimental Setup

Fourier spectrometer Bruker IFS 113v has been used throughout this work for performing the IR measurements. Figure 3.3 shows the schematic diagram of the FT-IR spectrometer.

There are two sources namely the globar source *(1)* for measurements in the MIR range and Hg arc lamp *(2)* for the FIR range. The beam from the source passes to the main optical chamber through an aperture *(3),* which can be closed, or opened to different diameters namely 1 mm, 2 mm, or 3 mm. The beam then passes through the filter wheel *(4)* and reaches the beam splitter wheel *(5).* The purpose of beam splitter is to split the beam to two parts to move towards the mirrors *(6).* The beam splitter wheel has six beam splitters characteristics for different wavenumber. These are 3.5 μm mylar (160-700 cm^{-1}), 6 μm mylar (T222) (30-650 cm^{-1}), 12 μm mylar (80-220 cm^{-1}), 23 μm mylar (20-100 cm^{-1}), 50 μm mylar (10-55 cm^{-1}), and KBr (400-5000 cm^{-1}). The beam splitter 6 μm mylar (T222) (30-650 cm^{-1}) is usually used for FIR range and KBr (400-5000 cm^{-1}) is used for MIR range. After the beam is reflected by the moving mirror *(6),* it is reflected by different mirrors to the reflection path *(7)* and then to sample at position *(8).* Then the signal is collected by the detectors namely DTGS (deuterated triglycine sulphate) detector *(11)* or bolometer *(12).* If the sample is transparent, one can measure transmission with follows the transmission path *(9)* with sample at *(10).* Thus this spectrometer can be used in both reflection and transmission mode.

This spectrometer works in the FIR and MIR range that is from 15- 5000 cm^{-1}. For low temperature measurements from 300 K to 10 K, the sample is placed in Oxford CF cryostat in vacuum with polyethylene window. A continuous flow of helium (He) is let into the cryostat to cool down the sample. For low temperature transmission measurements, the sample holder is arranged such that the reflected beam from the optical chamber can pass through the sample. He-cooled Si bolometer operating at 1.6 K is used at low temperature. For high temperature measurements, a commercial high-temperature cell Specac P/N 5850 was used in the temperature range 300-900 K and DTGS detector is used as the detector. In the case of an anisotropic sample, the light is polarized in order to see the phonons in both polarizations. For FIR range, a polarizer made of metal mesh on polyethylene thin layer is used and for MIR range, homemade

kalomel polarizer is used. A resolution in the range of 0.5 cm^{-1} to 2 cm^{-1} is used mostly. The real spectrometer is shown in figure 3.4. [98, 99]

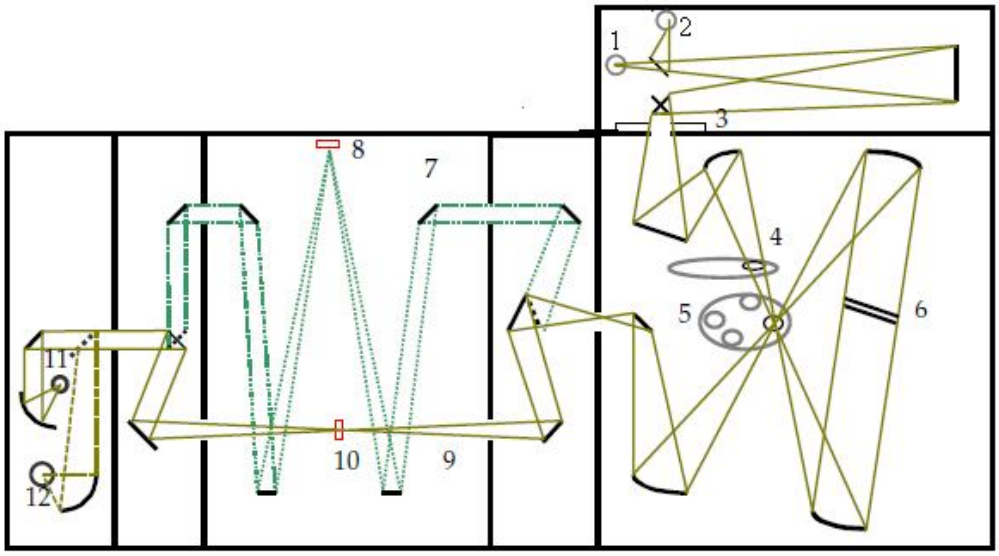

Figure 3.3. Schematic diagram of Fourier spectrometer Bruker IFS 113v. (1) globar source for MIR range, (2) Hg source for FIR range, (3) aperture, (4) Filter wheel, (5) Beamsplitter wheel, (6) scanning mirror, (7) reflection path, (8) sample position 1, (9) Transmission path, (10) sample position 2, (11) DTGS detector and (12) bolometer.

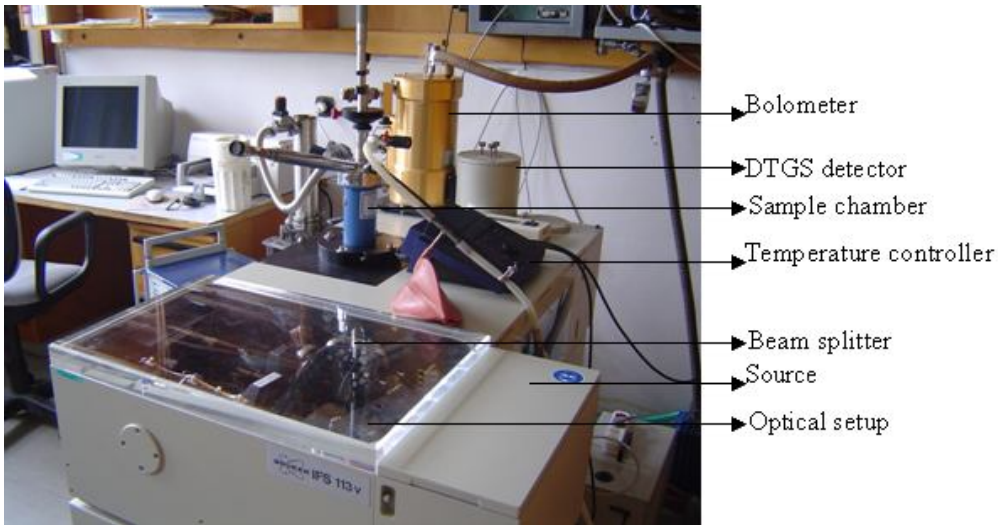

Figure 3.4. FT- IR spectrometer.

Advantages of FT-IR spectrometer

- As all the frequencies are measured simultaneously, the measurements can be done faster.
- Allows to measure both reflection and transmission mode.
- High resolving power (around 10^6 in MIR).
- FT-IR spectrometer is sensitive and has less noise.
- As the moving mirror is the only continuously moving part in the spectrometer, it is easy to simplify and has less chance of breakdown.
- High wavenumber accuracy.

3.2.3 Analysis of Data

Measurements are done with the help of Optics User Software (OPUS)- NT version 5.0, which is designed by Bruker. The software allows selecting settings for reflection and transmission mode according to the measurement to be carried out. Various functions like the opening and closing of aperture, selection of beam splitter, resolution, number of scans and etc., can be adjusted by the program. OPUS accumulates all the scans during the measurement and display as one corresponding spectra, reflection or transmission vs. wavenumber. OPUS also has various options to modify the spectrum like merging, cutting, multiplying etc.

Analysis of the reflectance spectra is also carried out by the program 'Wasf- Asf for windows', version 3.0. Wasf allows fitting the reflectivity spectra with *3*- or *4*-parameter models as given in section 3.2.3.1 and 3.2.3.2, respectively. This can be done in reflection and transmission mode, as well as for single crystals, bulk and ceramics. Fitting of double layer structure is described in section 3.2.3.4. The reflectivity fit, real and imaginary part of dielectric constant can be calculated directly from this program. Other parameters of interest like the conductivity, Im[1/ε], oscillator strength, etc. can be then calculated. Thus Wasf provides a whole picture of the sample measured. The real and imaginary part of dielectric constant can be obtained from the reflectivity spectra by KKR using OPUS as described in section 3.2.3.3.

The optical experiments generally measure the intensities of the incident (I_0), reflected (I_R) and transmitted (I_T) beams. From the energy conservation law:

$$I_0 = I_R + I_T + I_A \tag{3.1}$$

where I_A is the intensity absorbed by the sample. Equation (3.1) can be written as:

$$R + T + A = 1 \tag{3.2}$$

where $R = I_R / I_0$, $T = I_T / I_0$ and $A = I_A / I_0$ are the apparent reflectivity, transmission and absorptivity, respectively. Optical constants can be determined by measuring $\tilde{R}$ and $\tilde{T}$.

The complex dielectric function is given as:

$$\varepsilon(\omega) = \varepsilon'(\omega) - i\varepsilon''(\omega) \tag{3.3}$$

where ε' the real part reflects a dispersion of the *permittivity* and *ε"* the imaginary part is the *dielectric losses* caused by long-wavelength fluctuation of polarization of transverse character. The *complex refractive index* is given as:

$$\tilde{n}(\omega) = n(\omega) - ik(\omega) \tag{3.4}$$

where *n(ω)* is the refractive index and *k(ω)* is the extinction coefficient. In terms of *n(ω)* the permittivity and losses are given as:

$$\begin{aligned} \varepsilon' &= n^2 - k^2 \\ \varepsilon'' &= 2nk \end{aligned} \tag{3.5}$$

The experimentally measurable quantity is *reflectance R(ω)*, defined as the ratio of the reflected intensity to the incident intensity, is given as:

$$R(\omega) = \frac{I_R}{I_0} = \left| \frac{n(\omega) - 1}{n(\omega) + 1} \right|^2 = \left| \frac{\sqrt{\varepsilon(\omega)} - 1}{\sqrt{\varepsilon(\omega)} + 1} \right|^2 \tag{3.6}$$

The dielectric function model can be derived either by summing over independent (or coupled) oscillators or by factorizing over poles and zero, using the property of the LO modes.

3.2.3.1 Classical Oscillator Model

The classical method to fit the experimental spectra obtained by equation (3.6) is shown by oscillator model for dielectric function. This can be re-written as the sum of *n* damped harmonic oscillators:

$$\varepsilon(\omega) = \varepsilon_1(\omega) - i\varepsilon_2(\omega) = \varepsilon_\infty + \sum_{j=1}^{n} \frac{\Delta\varepsilon_j \omega_{TOj}^2}{\omega_{TOj}^2 - \omega^2 + i\gamma_{TOj}\omega} \tag{3.7}$$

Here $\varepsilon_\infty = n^2$ is the dielectric constant at high frequency, ω_j is the eigenfrequency of the j[th] phonon mode, γ_j is the corresponding damping, and $\Delta\varepsilon_j$ is the dielectric strength. The parameters namely, frequency, damping and dielectric strength can be adjusted to obtain the best possible fit for the experimental reflectivity. Thus it is also called 3-parameter model and was first introduced by Barker and Hopfield.[100,101] This classical oscillator model gives equal damping to the TO and LO modes for each single oscillator.[102] As the vibrational modes with different energy levels have different phonon decay and so different damping, the classical oscillator model generally fails for wide reflection bands.[102, 103]

3.2.3.2 *4*- Parameter Model

The *4*-parameter model is the factorized form of the dielectric function, introducing the LO damping constant (γ_{LOj}) as the fourth parameter for each TO-LO pair.

$$\varepsilon(\omega) = \varepsilon_\infty \prod_j \frac{\omega_{LOj}^2 - \omega^2 + i\gamma_{LOj}\omega}{\omega_{TOj}^2 - \omega^2 + i\gamma_{TOj}\omega} \tag{3.8}$$

The wide reflectivity spectra as obtained for ferroelectric crystals have its TO and LO frequencies located at low and high frequency edges of IR reflection bands and their damping corresponds to the slope of these edges. As the *4*-parameter model allows assigning different TO and LO damping, this is most appropriate for wide reflection bands. For a good and reasonable fit, the conditions like $\gamma_{LO} \geq \gamma_{TO}$ and $\gamma_{TO}/\gamma_{LO} \geq (\omega_{TO}/\omega_{LO})^2$ must be followed.[35, 103, 104]

The computer program 'WASF' is used to fit the reflectivity spectra. Based on the spectra, different fitting models like *3*-parameter or *4*-parameter model can be selected. Number of oscillators can be added based on the number of reflectivity bands. Giving values for ε_∞, specific for the particular crystal, the (*3*- or *4*-) adjustable parameters can be adjusted giving the best possible fit. The reflectivity fit, permittivity, dielectric loss and dielectric strength can be calculated directly by this program.

3.2.3.3 Kramers-Kronig Relation

The *Kramers-Kronig Relation* (KKR) was derived independently by Ralph Kronig and Hendrik Anthony Kramers. KKR connects the real and imaginary part of any complex function, which is analytic in the upper half plane.[105]

The dielectric constant models indicate the response of a wave packet (specifically its FT) in both dispersive and absorptive qualities with the real part corresponding to dispersion and the imaginary part corresponding to absorption.[106]

The real and imaginary part of dielectric constant is given by:

$$\varepsilon'(\omega) - \varepsilon_\infty = \frac{2}{\pi} P \int_0^{\omega_c} \frac{\varepsilon''(\omega')}{\omega' - \omega} d\omega'$$
$$\varepsilon''(\omega) = \frac{1}{\pi} P \int_0^{\omega_c} \frac{\varepsilon'(\omega')}{\omega' - \omega} d\omega' \qquad (3.9)$$

Here P is Cauchy principal value. The upper limit of frequency ω_c is such that $\omega << \omega_c$ where ω_c is above lattice vibration and below electronic frequency.[107]

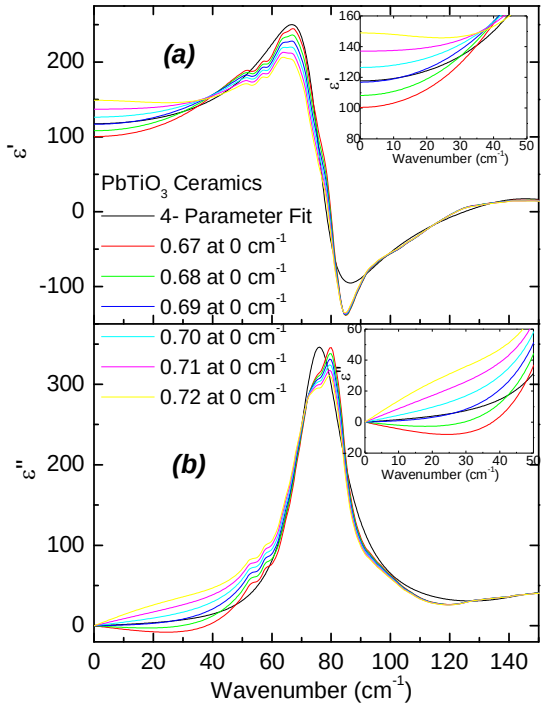

Figure 3.5. Permittivity (a) and dielectric losses of $PbTiO_3$ ceramics at T = 300 K fitted by 4-parameter model and Kramers-Kronig relations (KKR) extrapolated to different values at 0. Inset shows a detail picture around 0.

The computer program OPUS was used to apply KKR to reflectivity spectra to obtain the permittivity (real) and dielectric losses (imaginary). Conditions to apply KKR are:

1. The input spectra must have data till a higher frequency. Thus the FIR and MIR spectra are merged to have data from 0 to 3000 cm^{-1}.
2. The input spectra must have very less or no noise, as KKR is very sensitive to noise.
3. As the noise below 50 cm^{-1} cannot be avoided, cut the spectra below 50 cm^{-1}.
4. Extrapolate the spectra from 50 cm^{-1} to 0. The extrapolation value at 0 influences the static permittivity and losses as shown in figure 3.5. It is seen from the inset that extrapolation value, which holds the losses just above 0 is the most appropriate (0.69 in this case).

3.2.3.4 Thin film Fitting Model

Consider a thin film of refractive index n_1 and substrate of refractive index n_2 as the system is in air of refractive index n_0 as in figure 3.6. Assuming that the electric vector is parallel to the slab, Fresnel coefficient can be written as the ratio of the incident (*i*) and reflected (*r*) or transmitted (*t*) and electric field amplitudes at the interface between media air (*0*) and film (*1*).

$$\tilde{r}_{01} = r\exp(i\Phi_r) = \frac{E_r}{E_i} = \frac{Z_1 - Z_0}{Z_1 + Z_0} = \frac{n_0^* - n_1^*}{n_0^* + n_1^*} \quad (3.10)$$

$$\tilde{t}_{01} = r\exp(i\Phi_t) = \frac{E_t}{E_i} = \frac{2Z_1}{Z_1 + Z_0} = \frac{2\tilde{n}_0}{\tilde{n}_0 + \tilde{n}_1} \quad (3.11)$$

where the complex surface impedance of the medium *0* is defined as $Z_0 = (\frac{4\pi}{c})(\frac{E_0}{H_0})$. In vacuum $E_0=H_0$ and in vacuum $H_0 = (n_0^*/\sqrt{\mu_0})E_0$, where μ is the magnetic permeability.[76, 108, 109]

In the coherent case, (used in plane-parallel substrates where the optic waves, based on superposition of the amplitudes of the electromagnetic fields, include interference phenomena), the total reflectance and transmittance of the layer can be calculated by adding up all partial waves as these coefficients are known at the boundaries. Considering $\tilde{r}_1$ and $\tilde{t}_1$ as composite Fresnel coefficient for the film, the overall power reflectance and transmittance of the film (*1*) between the media *1* and *2* is given by

$$R_1 = |\tilde{r}_1|^2, T_1 = Re\left(n_2^*/n_1^*\right)|\tilde{t}_1|^2 \tag{3.12}$$

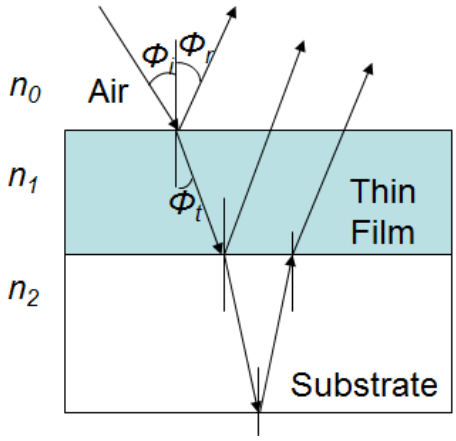

Figure 3.6. A two-slab thin film system surrounded by air.

When the film thickness d_1 or inhomogeneity of the film is small compared to the coherence length of the radiation (thin film) are

$$\tilde{r}_1 = \frac{\tilde{r}_{11} + \tilde{r}_{12}\exp(2i\tilde{\delta}_1)}{1 + \tilde{r}_{11}\tilde{r}_{12}\exp(2i\tilde{\delta}_1)}$$

$$\tilde{t}_1 = \frac{\tilde{t}_{11}\tilde{t}_{12}\exp(i\tilde{\delta}_1)}{1 + \tilde{r}_{11}\tilde{r}_{12}\exp(2i\tilde{\delta}_1)} \tag{3.13}$$

The complex phase shift $\tilde{\delta}_1 = 2\pi\tilde{n}_1 d_1/\lambda_0$, where λ_0 is the wavelength of the radiation in vacuum, accounts for both the real phase shift and the wave attenuation in the film due to absorption. These formulae include interference effects and depend upon coherence of the radiation over the optical path across the sample.

In second approach, consider the incoherent case, used for rough samples, where the reflection and transmission process at the front and back surface of the sample is added incoherently. For a thick film with thickness d_1, which is large compared to the coherence length of the radiation, and the complex refractive index $\tilde{n}_1 = n_1 + ik_1$, where $k_1 \ll 1$, the power reflection and transmittance coefficient at the film medium (*0*) interface are

$$R_{01} = R_{10} = \frac{(n_1 - n_0)^2 + (k_1 - k_0)^2}{(n_1 + n_0)^2 + (k_1 + k_0)^2} \tag{3.14}$$

$$T_{01} = T_{10} = \frac{4(n_1 n_0 + k_1 k_0)}{(n_1 + n_0)^2 + (k_1 + k_0)^2} \tag{3.15}$$

The overall power reflectance and transmittance of the film including multiple passage of the beam in the film are

$$R_1 = R_{01} + \frac{T_{01}^2 R_{01} \exp(-2\alpha_1)}{R_{01}^2 \exp(-2\alpha_1)}$$

$$T_1 = \frac{T_{01}^2 R_{01} \exp(-\alpha)}{1 - R_{01}^2 \exp(-2\alpha_1)} \qquad (3.16)$$

where $\alpha_1 = 4\pi k_1 d_1/\lambda_0$, and R_{01} and T_{01} are the reflectance and transmittance coefficient at the air-film interface respectively.

For fitting of the thin films using Wasf program, the IR optical properties of the bare substrate are first fitted in the whole temperature range using the 4-parameter model given in equation (3.8). The reflection of the system of film+ substrate is treated as a two-slab system, is fitted with *3*- or *4*-parameter model taking the substrate reflectance as the background. The thickness of the substrate and film can be specified in the Wasf program. Both reflection and transmission spectra can be well fitted by this model as a sum of harmonic oscillators.

3.3 Raman Spectroscopy

The inelastic scattering of light, predicted by Smekal (1923) was experimentally observed by Dr. C. V. Raman in 1928, is called *Raman Effect*. When a monochromatic light of frequency v_0 is directed on a crystal, the scattered light is of two types:

1. Rayleigh Scattering, having frequency the same as incident beam and is stronger.
2. Raman scattering has frequencies $v_0 \pm v_m$, where v_m is the vibrational energy of the scattered crystal. This is very weak effect. The line $v_0 + v_m$ is called anti-Stokes and $v_0 - v_m$ is called Stokes lines.

The process of interaction of monochromatic light with a crystal giving Rayleigh, Stokes and anti-Stokes lines are shown in figure 3.7.

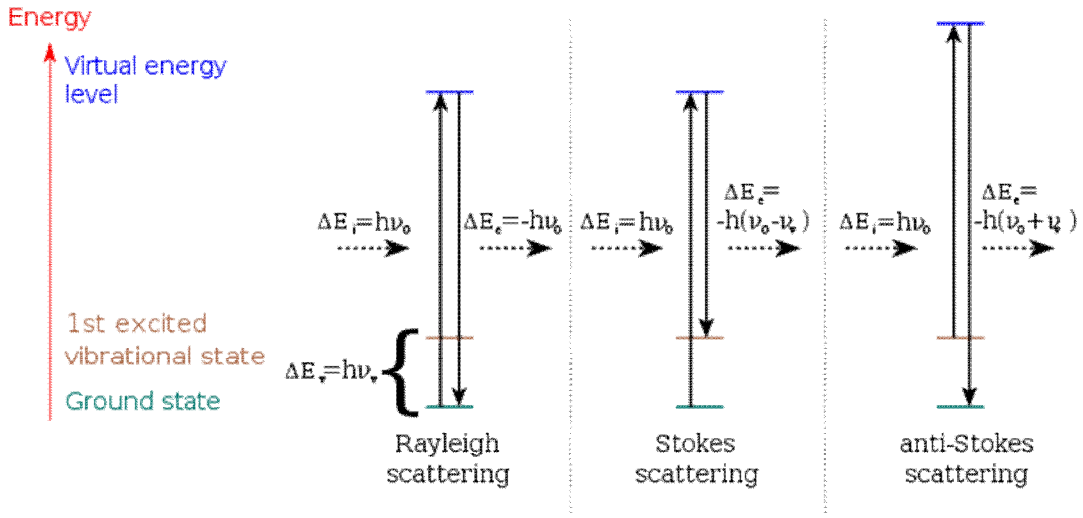

Figure 3.7. Inelastic scattering of light giving Stokes and anti-Stokes lines (Raman Effect) and Rayleigh scattering.

3.3.1 Origin of Raman Spectra: Classical explanation

The electric field strength E of the incident light fluctuating with time t is given as:

$$E = E_0 \cos 2\pi \nu_0 t \tag{3.17}$$

where E_0 is the vibrational amplitude and ν_0 is the frequency of the incident light (laser). Interaction of light with crystal develops a dipole moment in the crystal given as:

$$p = \alpha E = \alpha E_0 \cos 2\pi \nu_0 t \tag{3.18}$$

Here α is the polarizability (tensor), proportionality constant. The atomic vibrations due to the crystal vibrations are given by:

$$Q = Q_0 \cos 2\pi \nu_m t \tag{3.19}$$

where q_0 is the vibrational amplitude of the atomic vibration. Expanding α by Taylor series gives:

$$\alpha = \alpha_0 + \left(\frac{\partial \alpha}{\partial Q}\right)_0 Q_0 + \ldots \tag{3.20}$$

Thus using equation (3.20) and (3.19), equation (3.18) can be rewritten as:

$$p = \alpha_0 E_0 \cos 2\pi \nu_0 t + \left(\frac{\partial \alpha}{\partial Q}\right)_0 Q E_0 \cos 2\pi \nu_0 t$$

$$= \alpha_0 E_0 \cos 2\pi\nu_0 t + \left(\frac{\partial\alpha}{\partial Q}\right)_0 Q_0 E_0 \cos(2\pi\nu_0 t)\cos(2\pi\nu_m t)$$

$$= \alpha_0 E_0 \cos 2\pi\nu_0 t + \frac{1}{2}\left(\frac{\partial\alpha}{\partial Q}\right)_0 Q_0 E_0 \{\cos[2\pi(\nu_0 + \nu_m)t] + \cos[2\pi(\nu_0 - \nu_m)t]\} \quad (3.21)$$

The first term describes the elastic or Rayleigh scattering. The second term gives the Raman scattering of frequency $\nu_0 + \nu_m$(anti-Stokes) and $\nu_0 - \nu_m$ (Stokes).

The selection rule gives that when $(\partial\alpha/\partial Q)_0$ is zero; the vibration is not Raman-active. Thus for a mode to be Raman- active it should have change in polarizability associated with it.[107, 110, 111, 112]

Raman spectroscopy measures the quanta of energy shift associated with the scattering process due to either phonon emission (Stokes shift) or the absorption of phonon by the photon (anti-Stokes shift).The upward or downward transition in energy level is associated with energy transfer $\hbar\nu_0$ where ν_0 is the scattering frequency and scattering wavevector $\boldsymbol{q}$ corresponding to momentum transfer $\hbar\boldsymbol{q}$.(Figure 3.8) The conservation laws follows such that[112, 113]:

$$\nu_I - \nu_s = \nu_0 \quad (3.22)$$

$$\boldsymbol{K_I} - \boldsymbol{K_S} = \boldsymbol{q} \quad (3.23)$$

The detection of the Stokes component of the spectrum is given by spectral differential cross section defined as the rate of removal of energy from the incident beam as a result of its scattering in a volume V into a solid-angle element $d\Omega$, with a scattered frequency between ν_S and $\nu_S + d\nu_S$. (figure 3.9). The spectral differential cross section is given as:

$$\frac{\partial^2\sigma}{\partial\Omega\partial\nu_s} \approx \nu_S^4 \left|\sum_{i,j} e_{Si}\frac{\partial\alpha_{ij}(\nu_I)}{\partial Q_j(\boldsymbol{q})}e_{Ij}\right|^2 (1+\eta(\nu,T))\frac{\hbar}{\pi}\operatorname{Im}T_j(\nu,\boldsymbol{q}) \quad (3.24)$$

Here the scattered beam has frequency ν_S and polarization e_S and incident beam has frequency ν_I and polarization e_I.

The term $\partial\alpha_{ij}(\nu_I)/\partial Q_j(\boldsymbol{q})$ is the *Raman tensor*, which gives the relation between incoming and outgoing electric field for a given vibrational mode j. Here Q_j is the displacement and $\boldsymbol{q}$ is the quasi-momentum. For a crystal to be Raman active the Raman tensor must have non-zero elements, i.e. there must be a change in polarizability.

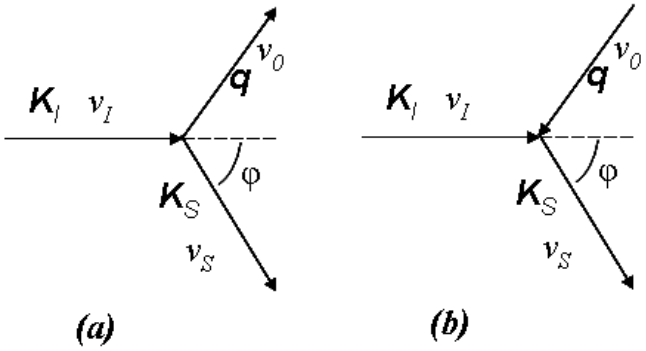

Figure 3.8. Geometry of wavevector and momentum conservation involved in Stokes (a) and Anti-Stokes (b) inelastic scattering process.

The term $1+\eta(\nu,T)$ is specific for Stokes and this becomes $\eta(\nu,T)$ for anti-Stokes process. Here Bose- Einstein factor is given as:

$$\eta(\nu,T)=\frac{1}{e^{\hbar\nu_0/k_BT}-1} \tag{3.25}$$

Such that T is the absolute temperature and k_B is Boltzmann constant.

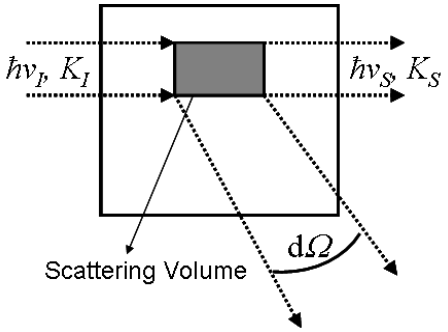

Figure 3.9. Raman scattering geometry.

In equation (3.24) the term T_j is called *response function* defined as the response of the system to harmonic force. The imaginary part of the response function gives the shape of the spectral line:

$$\mathrm{Im}\,T_j(\boldsymbol{q},\omega)=\frac{\omega\gamma_{j,\boldsymbol{q}}}{(\omega^2(\boldsymbol{q})-\omega^2)^2+\omega^2\gamma_{j,\boldsymbol{q}}} \tag{3.26}$$

3.3.2 Raman Spectrometer

Raman Effect was observed by Dr. C. V. Raman with a very simple setup. He used sunlight as the source, complementary filters and eye as detector. With the discovery of lasers Raman spectroscopy started to grow. The basic setup for a Raman spectrometer is shown in figure 3.10.

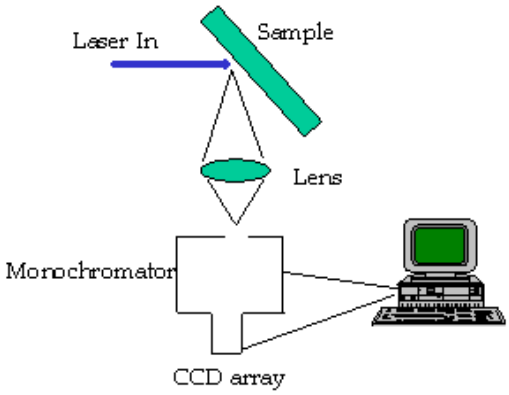

Figure 3.10. Schematic view of Raman spectrometer.

A typical Raman spectrometer consists of excitation source (laser), sample illumination and collection system, monochromator and detector. As Raman Effect is a weak effect, laser proved to be ideal source due to its high power, monochromaticity, small diameter and ease to focus.

Sample Geometry: The excitation and collection from the sample can be done in various ways as shown in figure 3.11.

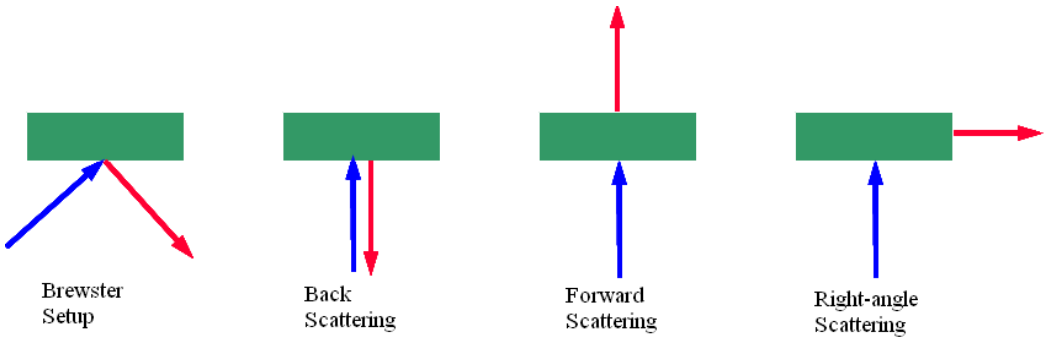

Figure 3.11. Examples of sample geometry. Incident and reflected ray at Brewster angle results in maximum light penetration into the sample. Back scattering is used with opaque samples or Raman microscopy, forward and right-angle scattering geometries can be used with transparent samples. Different samples geometries may bring in different spectra due to the selection rules.

Porto notation: Porto notation is a conventional method of representation of experimental scattering geometries. For example, *x(zx)y* indicates that the excitation light is incident on the sample along *x*-axis, polarized along *z* direction and the scattering light was detected along *y*-axis, polarized along *x* direction.[114]

3.3.3 Experimental Setup

Raman spectra are collected using a RENISHAW RM 1000 micro-Raman spectrometer using back scattering geometry. The different excitation source that can be used are 633 nm He-Ne line (red), 514.5 nm Ar line (green), 488 nm (blue) and 325 nm (Ultra violet) lines. They have power ≈10mW, which can be focused to a spot size of 1-2 μm. The objectives are of magnification 5x, 50x and 100x. A spectral resolution better than 2 cm^{-1} can be obtained by proper calibration. Holographic NOTCH filters with additional NExT filter are used to filter the Rayleigh lines down to ≈10 cm^{-1} from the laser line. The instrument is characterized by a single-grating monochromator, multichannel charge-coupled devices (CCD) detection and simple optical path. The sample can be measures in the temperature range 80-870 K with a temperature stability of ± 0.1 K using LINKAM THMS 600 cell. A Renishaw RM 100 Raman microscope is shown in figure 3.12. Raman spectroscopy is non-destructive analysis requiring little or no sample preparation. Raman spectroscopy has a wide range of application in other fields of science also.

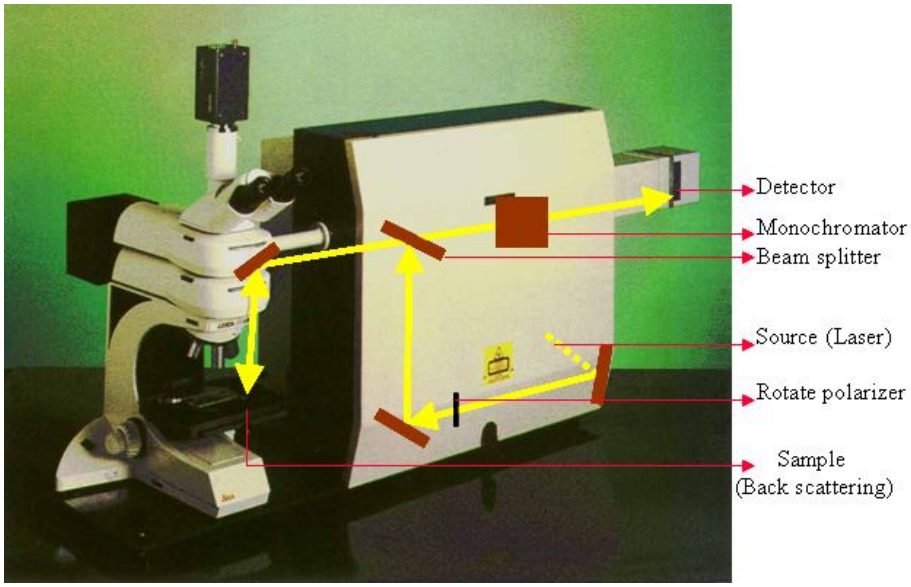

Figure 3.12. Renishaw RM 100 Raman microscope.

3.3.4 Analysis of Data

The experiment is carried out with the software Wire 1.3 with Galactic GRAMS/32 package, which is provided by the manufacturer. With the software the microscope allows the selection of regions of good optical quality, measure topology and in depth Raman spectra etc. The data are obtained as intensity vs. wavenumber. To analyze the results, the spectra were fitted by a sum of independent harmonic oscillators, Lorentzians, Gaussians superimposed on a suitable baseline, using a routine developed by Ivan Gregora and Jan Pokorny within the Igor Pro graphing software. The peak frequencies, amplitudes and width were left as adjustable parameters.[115, 116]

The *VV* and *VH* polarization configuration refer to the input and output light polarization corresponding to situation where polarization are parallel and crossed, respectively. Raman selection rules for thin films like PTO/LAO, with domains measured on the film surface and cross section is given in figure 3.13. The spectra on film surface consist of *E(TO)* mode in *VH* configuration and $A_1(TO)$ mode in *VV* configuration originating from *a*-domains and $A_1(LO)$ mode in *VV* configuration origination from *c*-domain. In the spectra from cross section, *E(TO)* mode in *VH* configuration originate from *c*-domain and 50% *a*-domains. *VV* spectra consist of $A_1(LO)$ modes origination from *c*-domain and $A_1(TO)$ modes from *c*-domain and 50% *a*-domains. Following these selection rules the *E(LO)* modes cannot be measured directly.[64]

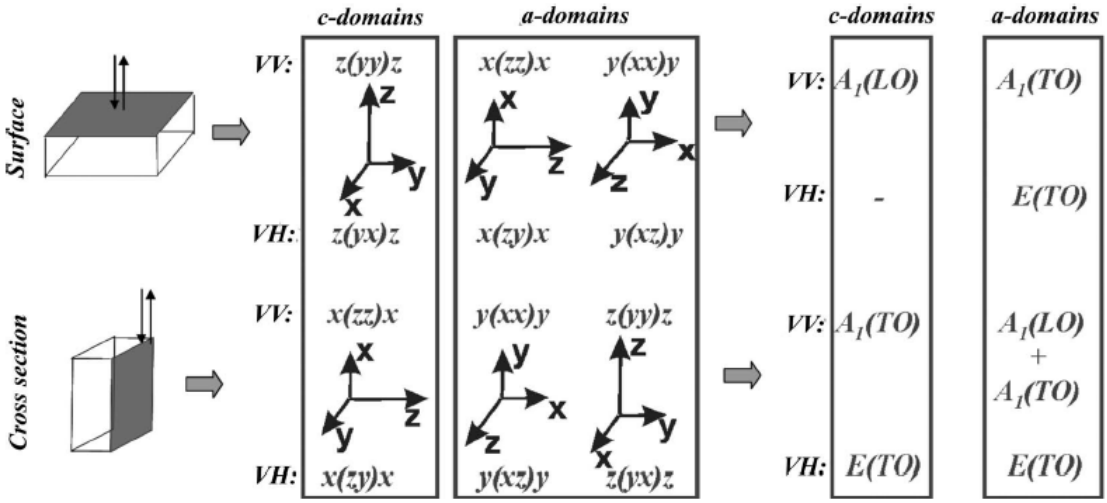

Figure 3.13. Raman scattering geometries and polarization configurations used for the Raman mode assigned in a- and c-domains PTO/LAO films.

3.4 Piezoresponse Force Microscopy (PFM)

Piezoelectricity is the phenomenon in which the electric charge is created on the sample surface by applying mechanical stress. Piezoelectric effect does not change the total charge of the sample but induces surface charge density.

Piezoelectric effect is a reversible process. *Direct piezoelectric effect* is the phenomenon of creating positive and negative electric dipole moment on the sample surface by applying mechanical stress. This can be given as:

$$P = d.X \tag{3.27}$$

where X is the mechanical stress and P is the polarization charge density. Here d is the piezoelectric strain coefficient.

The *reverse piezoelectric effect* is the phenomenon in which an applied electric field produces a mechanical strain in the same material. This can be written as:

$$S = d.E \tag{3.28}$$

Here S is the mechanical strain and E is the applied electric field.

When electric field is applied to the sample, the material expands if the field is parallel to the material's polarization and contracts if it is anti-parallel. This response of the sample to electric field is called *piezoresponse*.[117, 118]

3.4.1 Basic Principle of PFM

PFM based on the reverse piezoelectric effect, is used to measure the mechanical response when an electric field is applied through conductive tip of Atomic Force Microscopy (AFM). The voltage applied to the conductive tip is given as:

$$V_{tip} = V_{dc} + V_{ac}\cos(\omega_{ac}T) \tag{3.29}$$

where V_{dc} is the DC bias, V_{ac} is the AC bias and ω_{ac} is the AC bias frequency. With the application of electric voltage, the probe can move up or down based on the piezoelectric strain induced due to the charge on the sample surface as shown in figure 3.14.

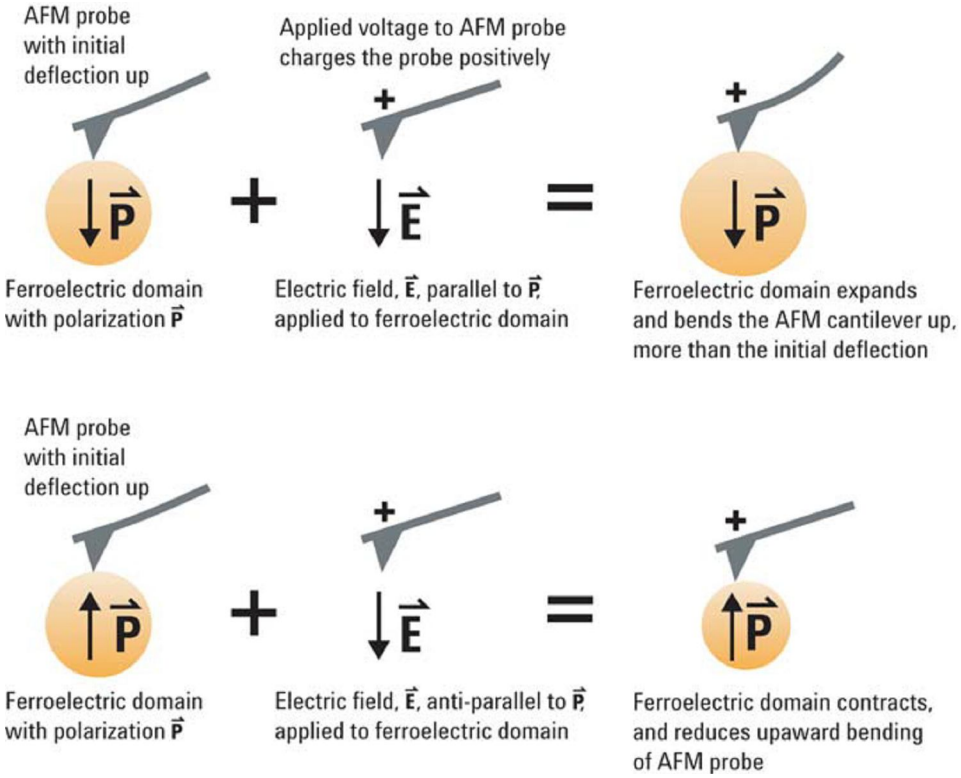

Figure 3.14. The basic idea behind PFM imaging.

The cantilever displacement due to such piezoelectric strain is given as:

$$z = z_{dc} + A(\omega_{ac}, V_{ac}, V_{dc})\cos(\omega T + \varphi) \tag{3.30}$$

where z_{dc} is the static surface displacement and φ is the phase shift between the driving voltage V_{ac} and the voltage induced deformation. Between domains of opposite polarities the phase shift is 180^0 as seen in figure 3.16. In equation (3.30), the first harmonic component is given as:

$$A(\omega_{ac}, V_{ac}, V_{dc}) = d_{33}V_{ac} + \left(\partial C_p / \partial z\right)(V_{dc} - V_s)V_{ac} \tag{3.31}$$

Here the first term on the right hand side gives the true Piezoresponse, where d_{33} is the *effective piezocoefficient*. In the second term V_s is the surface potential and C_p is the total capacitance of the cantilever- sample system, which gives the local electrostatic deformation caused by local and non-local stress.

In reverse piezoelectric effect the relationship between the strain and the applied electric field is given by a tensor of rank 3. In figure 3.15 if direction *x*, *y*, *z* is given by the subscript *1*, *2* or *3* and the corresponding strain is given by subscript *4*, *5* or *6*,

respectively. The first subscript of *d* in the tensor gives the direction of the polarization generated by the electric field and the second subscript gives the direction of applied stress.

Thus piezocoefficient d_{33} have induced strain in direction *3* per unit electric field applied in direction *3*. The piezocoefficient d_{15} will have induced shear strain about direction *2* per unit electric field applied in direction *1*[119,120,121].

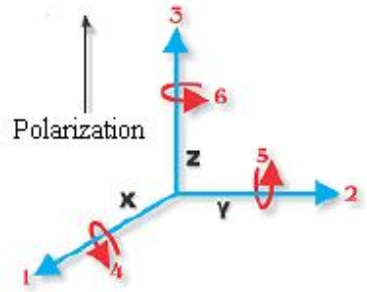

Figure 3.15. Direction of forces in the piezoelectric material.

3.4.2 PFM Imaging Modes

PFM images give the piezoelectric topography, and three typical PFM imaging modes based on the displacement of cantilever namely Vertical PFM (VPFM), Lateral PFM and Vector PFM.

Figure 3.16 (a) and (b) shows vertical PFM due to out-of-plane piezoresponse caused by d_{33} coefficient. When the applied electric field is parallel to polarization (a) the piezoelectric will expand and the signal will be in phase with V_{ac}. The piezoelectric will contract and cantilever will lower when the applied electric field is antiparallel to the polarization (b). Figure 3.16 (c) and (d) shows lateral PFM due in-plane piezoresponse caused by d_{15} coefficient showing the lateral motion of cantilever.

Vector PFM image is obtained by acquiring all three components of the piezoresponse, namely vertical PFM and at least two orthogonal lateral PFM components. This helps to reconstruct the polarization orientation.

The topography of the piezoelectric sample can be obtained by applying large field, such that patterns like single domain, domain array and other complex patters can be imaged without changing the surface topography.[119.120.121.122]

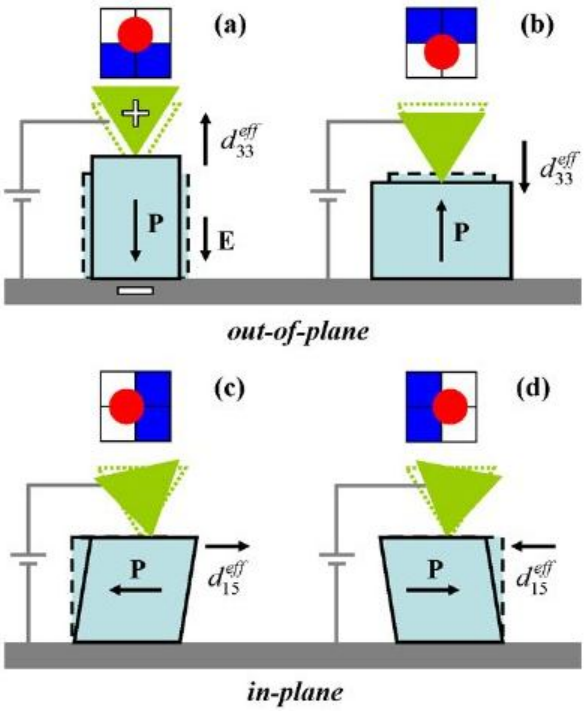

Figure 3.16. Vertical and lateral PFM imaging modes. (a) Applied electric field and spontaneous polarization are parallel, thus the cantilever is lifted up. (b) Applied electric field is anti-parallel to the spontaneous polarization, thus the cantilever lowers leading to the vertical contraction and horizontal expansion of piezoelectric sample. (c) and (d) shows shear movement when the applied electric field is orthogonal to the polarization.

3.4.3 Piezoresponse Force Microscope

PFM helps to see and study the domain structure in ferroelectric materials. PFM gives both surface topology images and distributions of lateral and normal oscillations. The information about phase distribution of lateral and normal oscillations helps to study the domain structure of the sample. The topology, its corresponding normal and lateral peizoresponse and normal and lateral phase lag is shown in figure 3.17.[123]

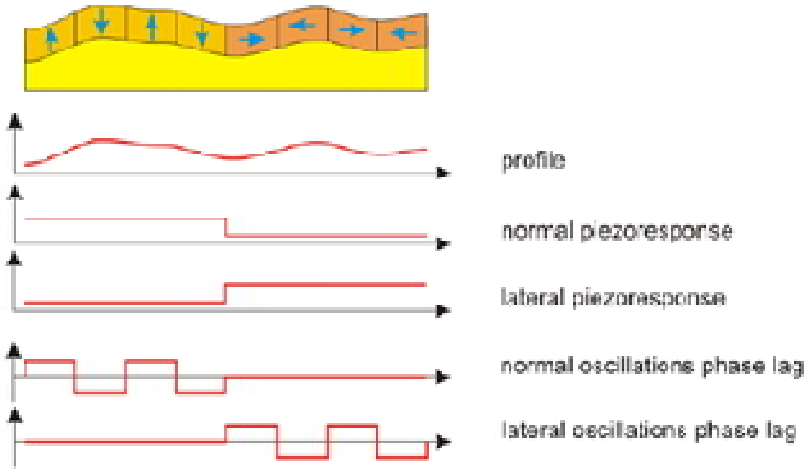

Figure 3.17. The different information obtained for a sample using PFM.

The basic structure of PFM microscope is shown in figure 3.18. As PFM is very sensitive to noises and vibrations, the microscope is fixed on a vibration isolation system. In order to reduce external perturbations and for safety reasons a protective hood is used to cover the sample on the measuring head. The optical viewing system helps to see the sample through the microscope and as the system is connected to a computer, the sample and the cantilever position is also seen in computer.

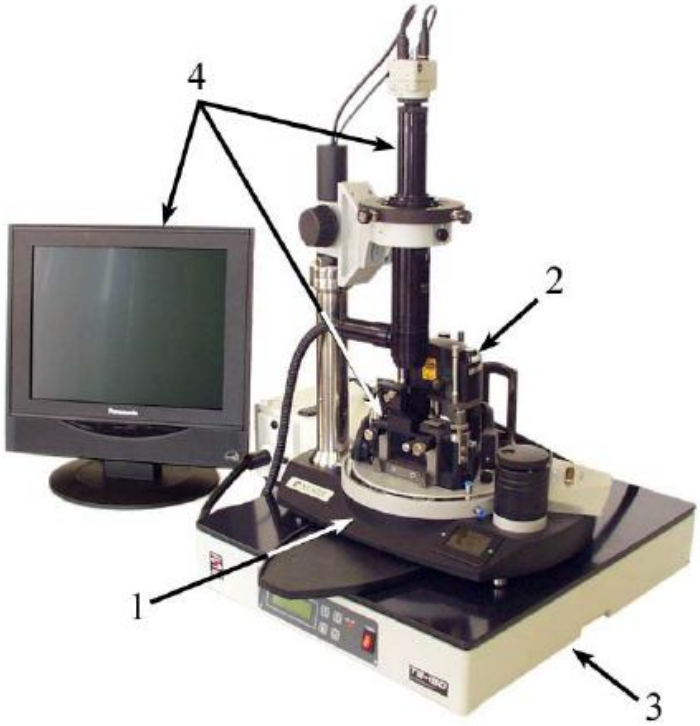

Figure 3.18. Piezoresponse force microscope. (1) Base unit, (2) measuring head, (3) vibration isolation system and (4) optical viewing system.

A software Nova by the manufacturer is used to work with this instrument. This is very user friendly, which gives the output as three images of 2D visualization of the scanning data. The figure 'Height' gives the topography, 'Magnitude' gives the amplitude of normal oscillations and 'Phase' gives the distribution of normal phase. The normal oscillations of the cantilever are obtained for signal DFL (the difference signal between top and bottom halves of the photodiode). For measuring lateral oscillations, signal LF (the difference signal between left and right halves of the photodiode) is measured.[124,125,126]

CHAPTER 4 Lead Titanate Ceramics

4.1 Introduction-$PbTiO_3$

PTO is a typical member of perovskite family with ABO_3 structure, with Pb^{2+} at A position, Ti^{4+} at B position and oxygen (figure 1.3), with unit cell volume 62.8 Å[132].

PTO single crystal has lattice parameters a_{PTO} = 3.899 Å and c_{PTO} = 4.153 Å at room temperature, with *c/a* ratio equal to 1.065. This tetragonal distortion is higher than in BTO, and also the Ps is higher (15 C/m^2)[31]. PTO undergoes first-order PT from paraelectric-to-ferroelectric PT at T_0 = 490° C.[132,134,135] In cubic phase the lattice parameter of PTO is given as a_{PTO} = 3.974 Å.[132]

Unlike BTO and many other similar materials, PTO has only paraelectric-to-ferroelectric PT and remains in tetragonal phase below *Tc* for a wide temperature range.[136, 137] The ferroelectric distortion in PTO at R*T* leads to a net dipole moment per unit volume, or polarization. XRD and neutron diffraction study show that the O^{2-} ions are shifted with respect to Pb^{2+} by 0.47 Å and Ti^{4+} is shifted by 0.30 Å, along the *z* axis.[80]

Cohen (1992) used first-principle calculation within the local density approximation (LDA) to interpret that the stability of tetragonal phase in PTO is due to the covalent nature of Pb 6*s* and O 2*p* states.[60] Experimental evidence for Pb-O covalency using maximum-entropy method analysis on the synchrotron-radiation powder date was given be Kuroiwa *et al*. (2001).[59]

In the cubic phase (space group O^1_h) the factor group analysis gives twelve optic modes comprising of $3T_{1u}$ and T_{2u} triply degenerate modes. T_{2u} is silent, which is neither IR nor Raman active. The T_{1u} modes are IR active. Tetragonal phase (below T_c) belongs to space group *P*4*mm* (C_{4v}). Here the $3T_{1u}$ modes split into $3A_1$+$3E$ modes and the T_{2u} splits into B_1+E modes. The $3A_1$+$4E$ modes are IR and Raman active and B_1 is only Raman active.[138] IR active lattice vibrations along the *c*-axis belong to A_1(TO) modes and lattice vibrations along the *a*-axis to *E*(TO) modes.[139]

Soft mode

In cubic and tetragonal phase, an underdamped temperature dependent soft mode was seen by Raman spectroscopy and inelastic neutron scattering.[139, 140] Two distinct transverse optic modes, namely A_1(TO) and *E*(TO) soften near $T_0 \sim T_c$ in PTO.[138,139,141]

The soft mode E(1TO) wavenumber approaches 55 cm^{-1}. Jang *et al*. (2009) discussed why the A_1(TO) mode frequency approaches finite frequency of 65 cm^{-1} near the Curie temperature T_c=693 K.[51]

$PbTiO_3$: Raman and IR spectra

The A_1(TO) modes and E(TO) modes were observed by different techniques like Raman spectroscopy[138,139,] IR spectroscopy[137,142,] neutron scattering[44,45,140] etc. Raman spectroscopy has been extensively used in 1970s for PTO single crystal studies by Burns *et al*. (1973), Cerdeira *et al*. (1975), Frey *et al*. (1976), etc.[139, 143, 144] Foster et al. (1993)[138] studied the detailed Raman spectra of PTO on high quality single-domain PTO crystal (with removed 90° and 180° domains).

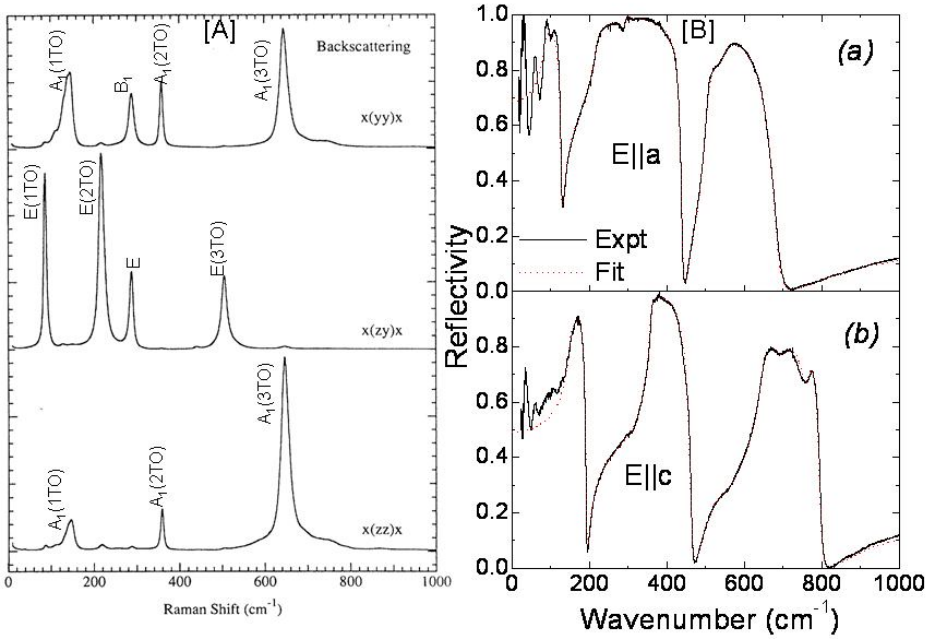

Figure 4.1. [A] Polarized Raman spectra of a single crystal PTO at T = 300 K recorded in parallel x(yy)x, x(zz)x and crossed x(zy)x polarization configuration[39]. [B] Reflectivity spectra obtained PTO single crystal (a) polarization along a-axis giving the E modes and (b) polarization along c-axis giving the A_1 modes. Red dotted lines give the corresponding fit using 4-parameter model[138,141].

Figure 4.1[A] shows the Raman spectra as obtained by backscattering geometry. Parallel and cross polarization configuration helps to obtain all the Raman active modes

specified for PTO single crystal. The parallel polarization configuration $x(zz)x$ gives the A_1(TO) modes, $x(yy)x$ gives the B_1+A_1(TO) modes and cross polarization $x(zy)x$ gives the E(TO) modes.

Table 4.1. Mode frequencies obtained for PTO single crystal using Raman spectroscopy by Burns et al. (1973)[139], Cerdeirs et al. (1975)[143], Frey et al. (1976)[144], Foster et al. (1993)[138] and using IR spectroscopy by Ostapchuk et al. (2011)[142].

	Burns *et al.* (1973) Raman Spectroscopy	**Cerdeirs *et al.* (1975)** Raman Spectroscopy	**Frey *et al.* (1976)** Raman Spectroscopy	**Foster *et al.* (1993)** Raman Spectroscopy	**Ostapchuk *et al.* (2011)** Infrared Spectroscopy
E(1TO)	89	85	88	87.5	86.4
E(2TO)	221	205	220	218.5	219
E(3TO)	508	502	505	505	505
E(1LO)	128	-	128	128	128
E(2LO)	445	-	439	440.5	440.5
E(3LO)	717	-	723	687	682
A_1(1TO)	127	117	147	148.5	149.5
A_1(2TO)	364	350	359	359.5	357
A_1(3TO)	651	634	646	647	642
A_1(1LO)	215	-	189	194	193
A_1(2LO)	445	-	465	465	464
A_1(3LO)	797	-	796	795	795
B_1+E	-	289	289	289	286

Perry et al. (1964) tried to investigate the optical phonons in PTO using IR spectroscopy. The transmission and reflectivity spectra were obtained on polycrystalline PTO.[137] Ostapchuk *et al*. (2011) obtained the polarized reflectivity spectra for PTO single crystal along *a*- and *c*-axis.[142] Figure 4.1 [B] gives the polarized reflectivity spectra for PTO single crystal for both polarization obtained with Fourier Transform IR spectrometer Bruker IFS 113v as described in section 3.2.2. The ε_∞ along *a*-axis is 6.6301 and along *c*-axis is 6.6419 showing almost a negligible anisotropy in the near IR range.[138] Table 4.1

gives the TO and LO phonon frequencies in cm^{-1} obtained for PTO single crystal by Raman and IR spectroscopy.

4.2 $PbTiO_3$ Ceramics

The PTO ceramic pellet for our study was prepared at Ecole Centrale Paris. The commercially available micrometric lead titanate powder was ball milled and the strain was relieved by annealing this nanopowder. A pellet of 20 mm diameter was formed by uniaxial and subsequent isostatic pressure application before being sintered at 1100 ^{0}C. The pellet was cooled very slowly with a very slow ramp around PT. Even though the whole thermal process took 30 hours in order to prevent strain that can break the pellet. X-ray studies were used to verify the perovskite phase. A specimen of 7x7x2 mm^3 dimensions was prepared from the inner part of pellet and polished carefully to perform various experiments.[87]

4.2.1 PFM Measurements

The PFM images, recorded on PTO ceramics using the AFM microscope of the Ntegra spectra apparatus of NT-MDT as described in section 3.4.3 are given in figure 4.2. Figure 4.2(a1), (a2), and (a3) represent the vertical height, magnitude and phase of the PFM response obtained from about 50x50 μm^2 sized area of the polished surface of the pellet. To get a better picture of the grains the area was reduced to 10x10 μm^2 sized area in figure 4.2(b1), (b2), and (b3). The PFM image could be zoomed still into 3.7x3.7 μm^2 sized area fig. 4.2(c). The grains of size 1-3 microns are well seen.

The domains formed in the PTO ceramics are not seen very well by this method. Thus additional experiment and theoretical calculations are performed to identify the presence of domains in PTO ceramics.

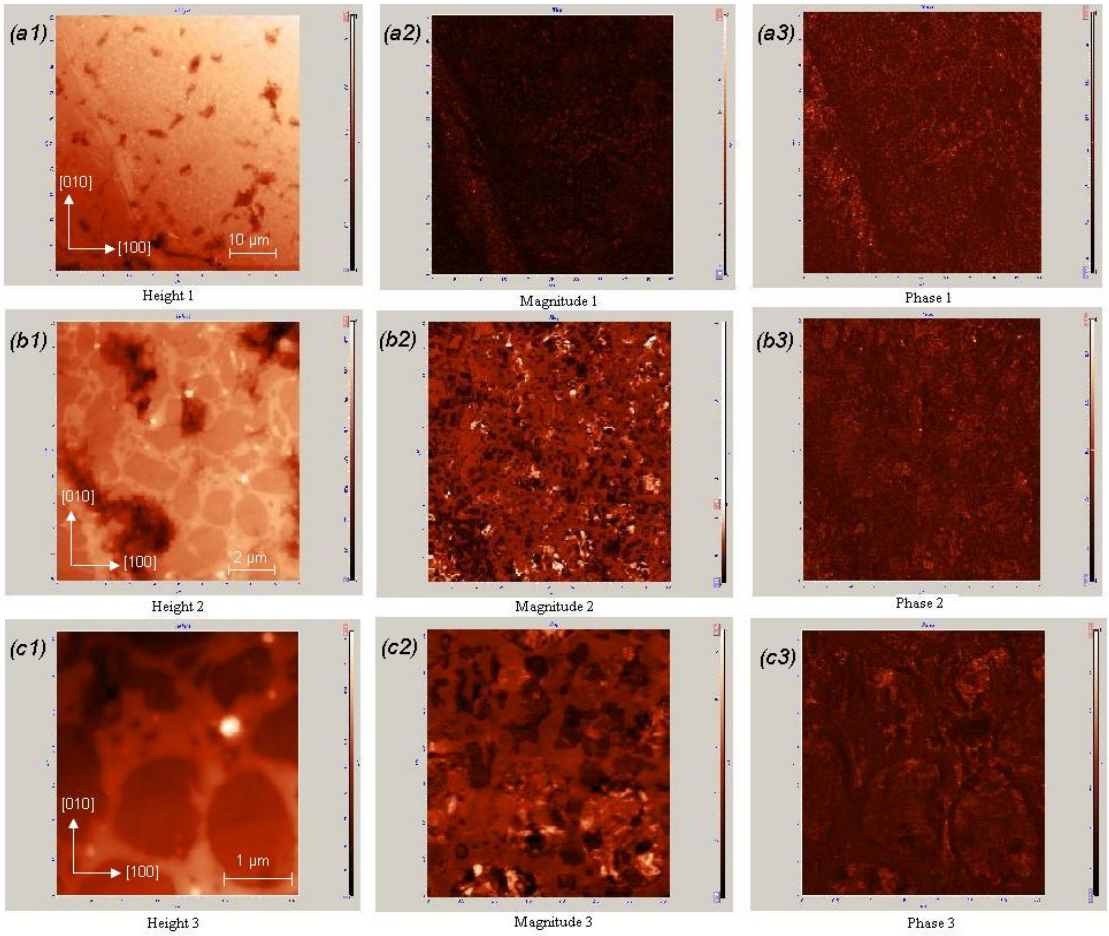

Figure 4.2. PFM images of PTO ceramics vertical (a) Height, Magnitude and Phase in an 50x50 µm^2 sized area (b) Height, Magnitude and Phase in an 10x10 µm^2 sized area and (c) Height, Magnitude and Phase in an 3.7x3.7 µm^2 sized area.

4.2.2 IR measurements

The near normal incident far-IR reflectivity measurements were performed as described in section 3.2.2 at R*T*. The unpolarized reflectivity spectra obtained from PTO ceramics along with the fit are given in figure 4.3. The unpolarized reflectivity spectra of macroscopically isotropic PTO ceramics remind of the polarized reflectivity spectra of PTO single crystal. There are, however, some additional features, marked by arrows.

The experimental data are evaluated using KKR as given in section 3.2.3.3 and also fitted to a "*4*-parameter"-type model as described in section 3.2.3.2. This reflectivity spectrum is fitted using 11 damped harmonic oscillators in order to fit all the details.

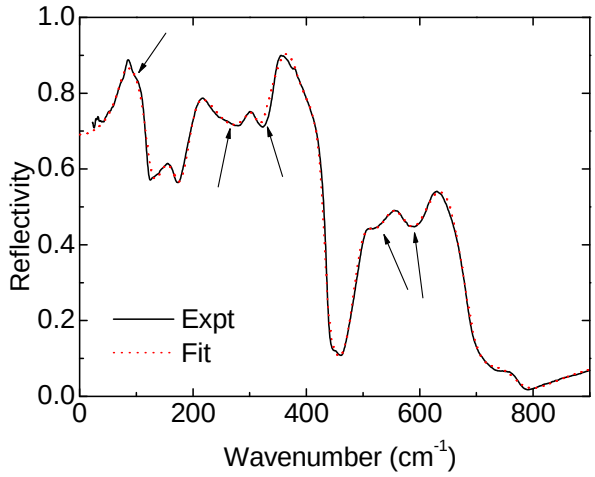

Figure 4.3. Unpolarized reflectivity spectra obtained for PTO ceramics at RT. The solid line (black) gives the experimentally obtained data and dotted line (red) shows the corresponding 4-parameter fit.

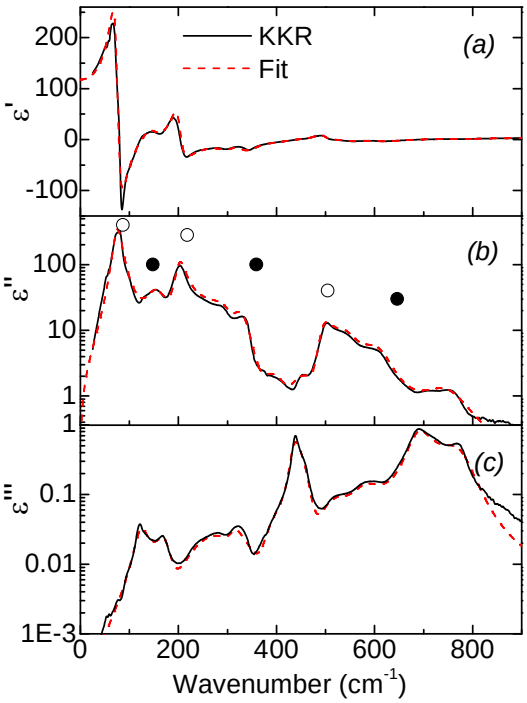

Figure 4.4. (a) Real and (b) imaginary part of permittivity and (c) Im[1/ε] obtained for PTO ceramics at RT. Open and full circle symbols mark positions of E and A_1 modes in the stress-free single-crystal bulk PTO respectively as given by Foster et. al. (1993).

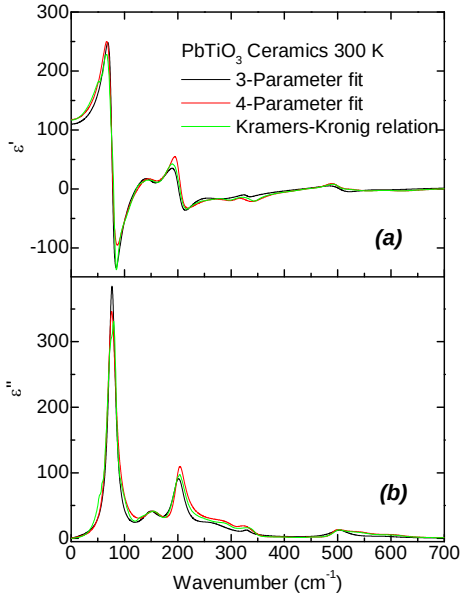

Figure 4.5. Permittivity (a) and dielectric losses (b) of PTO ceramics T =300 K fitted by 2 different models namely 3-parameter model (Classical oscillator), 4-parameter model in comparison with direct evaluation using Kramers-Kronig relations.

Table 4.2. The list of the 11 TO and 11 LO polar mode frequencies and damping parameters (in cm^{-1}) obtained from the adjustment to RT IR reflectance spectra of PTO ceramics (ω_∞=6.35). Values printed in bold correspond approximately to the intrinsic phonon modes of PTO. Results were compared with the permittivity spectra obtained with the help of KKR (see 3.2.3.3)

m	ω_{TOm}	Γ_{TOm}	ω_{LOm}	Γ_{LOm}
1	**76**	**20**	**125**	**32**
2	**153**	**46**	**175**	**37**
3	**202**	**24**	268	172
4	309	42	312	29
5	**333**	**62**	383	69
6	403	114	**436**	**24**
7	447	88	**463**	**42**
8	**494**	**31**	524	74
9	542	56	576	81
10	**610**	**73**	**689**	**55**
11	751	108	**775**	**76**

Figure 4.4 shows the real and imaginary part of permittivity, and –Im[1/ε] of PTO ceramics obtained from the fitting. The *E*(TO) and A_1(TO) mode frequencies given by Foster *et al.* (1993)[138] are shown as open and full circles. The peak positions in figure 4.4 (b), showing the imaginary part of permittivity, give the effective TO mode positions. The LO mode positions are apparent from figure 4.4 (c), showing the response function ε''=-Im[1/ε].

PTO ceramics is fitted using different parameters namely within the *3*-parameter fitting model and *4*-parametter fitting model. Figure 4.5 shows the real and imaginary part of permittivity spectra obtained by using these different fitting models. The agreement is satisfactory. The TO and LO frequencies and damping are obtained directly as fitting parameters in the *4*-parameter fit. Table 4.2 gives the corresponding parameters obtained by fitting the PTO ceramics using 11 damped harmonic oscillators. The

frequencies and dampings obtained for TO and LO modes corresponding approximately to TO and LO modes obtained by Foster *et al*. (1993) are highlighted.[87]

4.2.3 Effective Medium Approximation-Theoretical Approach

Effective medium approximation gives the macroscopic permittivity and effective dielectric function of the PTO ceramics from permittivity of the PTO single crystal. The ceramics effective permittivity is obtained by averaging the single crystal dielectric tensor by different mixing formulas as Bruggeman effective medium approach or Lichtenecker approach.

The tetragonal symmetry of PTO allows two independent non-zero components of the permittivity tensor, corresponding to the permittivity parallel and perpendicular to the tetragonal axis, ε_{33} and ε_{11}, respectively. The complex permittivity ε_{33} is determined by the A_1-symmetry polar modes as given in equation (2.35). The second component ε_{11} is determined by the 4 *E*- symmetry modes that can be similarly obtained from equation (2.36).

In order to apply different mixing formulas for PTO ceramics, the phonon frequencies were taken from Raman measurements by Forster *et al*. (1993) as given in table 4.1.[138] The high frequency dielectric constants along tetragonal axis were taken as $\varepsilon_{\infty 11}$ = 6.6301 and $\varepsilon_{\infty 33}$ = 6.6419 and for simplicity, all damping factors were set to be 25 cm^{-1}. The real (permittivity) and imaginary (losses) parts of the complex permittivity along ε_{11} and ε_{33} symmetry are given in figure 4.6.

The effective dielectric permittivity of the isotropic PTO was obtained from the intrinsic dielectric response of PTO single crystal using the mixing formulas described in section 2.6. Let the first model be the Bruggeman Effective medium approximation (called Model A) described by equation (2.37). Here *E* and A_1 responses are given the statistical weights 2 and 1, respectively.

The second model, Lichtenecker formula (called Model B) employs the expression for a geometric mean, given by equation (2.38). The third model used is the Arlt and Peusens model (called Model C), which takes into account explicitly the anticipated, so-called α-type domain configuration, having periodic repetition of two particular variants of the 90^0 twin patterns. This model leads to the formula (2.41).

The real and imaginary parts of the resulting effective dielectric function for the above mentioned three models are compared in figure 4.7. All three mixing models show clear peaks at mode positions that correspond to the 3 *E*(TO) and 3 A_1(TO) mode positions of the anisotropic PTO single crystal. The open circles given in figure 4.7 (b) give the 3 *E*(TO) positions and the closed circles give the 3 A_1(TO) mode positions of the PTO single crystal.

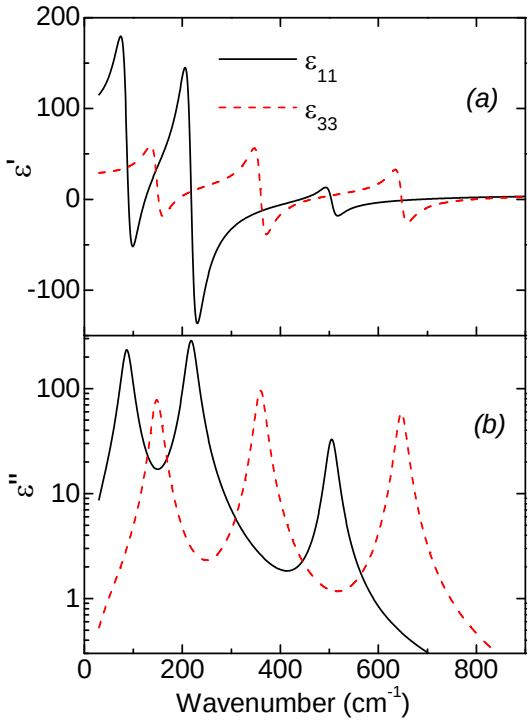

Figure 4.6. Real (a) and imaginary (b) part of the principal components of intrinsic permittivity tensor of a single domain PTO crystal, as derived through the equation (2.69) from the available RT Raman scattering study by Foster et al. (1993).

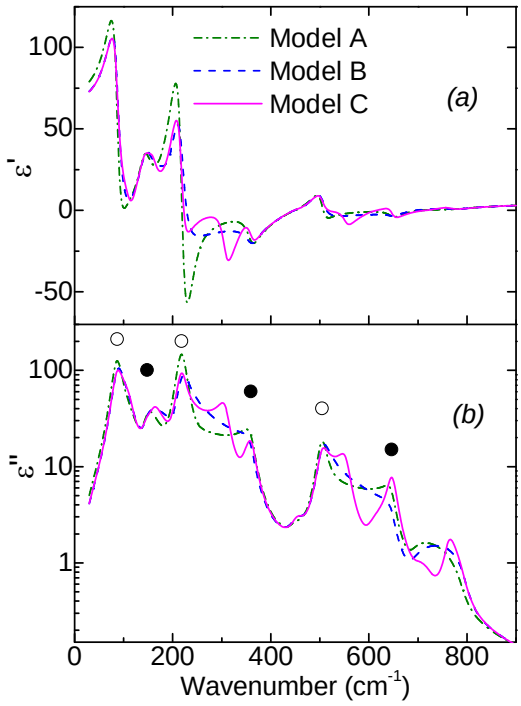

Figure 4.7. Real (a) and imaginary (b) part of the permittivity of isotropic PTO ceramics, predicted by three different effective medium approximations based on the single crystal permittivity as given in figure 4.5. The Model A (Bruggeman) is given by equation (2.50), Model B (Lichtenecker) is given by equation (2.51) and Model C (Arlt and Peusens) is given by equations (2.52-54). Open and full circle symbols mark positions of E and A_1 modes in the stress-free single-crystal bulk PTO, respectively, as given by Foster et. al. (1993).

However the loss spectra show more bands than expected from PTO single crystal. We have concluded that these extra bands are so called geometric resonances.[82] Geometric resonances are hybrid excitations resulting from the bulk polar modes as a result of coupling with the dynamical depolarization field. Loss spectra of Model C show geometric resonance at many positions like 300 cm^{-1}, 500 cm^{-1} etc. Some of these peaks are commonly seen in Model A, B and C like the weak mode around 450 cm^{-1}. These are the extra peaks seen in figure 4.7 (b) (other than those specified by Foster et al (1993) in PTO).

Comparing figures 4.4 and 4.7 showing the real and imaginary part of complex permittivity as obtained from our spectra of PTO ceramics and by the mixing formulas, it is seen that the Model C yields the spectra most similar to that obtained experimentally. The presence of additional peaks in the loss spectra of PTO ceramics, other than the expected 6 strong IR active phonon modes of PTO single crystal, shows the presence of geometric resonances. This allows us to draw the conclusion that the internal domain structure of grains in PTO ceramics is most likely similar to the so- called α-type domain configuration with 90^0 twin domains.

4.3 Discussion

The PFM images of PTO ceramics show the grain size 1-3 μm. The reflectivity spectra obtained for PTO ceramics have features belonging to both polarization of PTO single crystal. The reflectivity spectra are fitted with *4*-parameter model, which gives all *E* and A_1 mode positions. Geometric resonances give additional bands, other than the *E* and A_1 modes, which originate from the grain structure in the ceramics. Model calculations show the reflectivity, real and imaginary part of the permittivity for Bruggeman effective medium approach (Model A), Lichtenecker approach (Model B) and Arlt and Peusens model (Model C). Arlt and Peusens model (called Model C) is the most similar to the experimental reflectivity spectra obtained for PTO ceramics, indicating the presence of α-type domain configuration with 90^0 twin domains within the grains. These results suggest that the IR spectroscopy could be used as an effective tool to identify the domain structure present in the ceramic grains.

Publication Related to this work:-

J. Hlinka, E. Simon, C. Bogicevic, F. Karolak and P. E. Janolin, Geometric resonances in Far-infrared reflectance spectra of $PbTiO_3$ ceramics. Phys. Rev. B. 84, 092104 (2011)

CHAPTER 5 Lead Titanate Thin Films

5.1 Introduction

Basic ferroelectric and vibrational properties of PTO single crystal and ceramics have been resumed in Chapter 4. Such features as high Curie temperature, high piezoelectric coefficient and low dielectric constant makes PTO thin films quite much interesting for many day-to-day applications. The properties of the PTO thin films grown on different substrates vary from one another depending on the strain and domain structure induced in the film during the process of their growth. The lattice mismatch between the lattice parameters of the PTO film and the substrate is responsible for inducing the strain and domain structure.

Pertsev *et al.* (1998) tried to obtain the strain-phase diagram for PTO using Landau-Ginsburg-Devonshire-type thermodynamic theory by assuming single homogeneous domain state for all possible ferroelectric phases in thin film.[74] The strain-phase diagram was improved by considering two-domain states with a priori fixed domain-wall orientation.[147] This phase diagram contained single- or double- domain states with domain walls orientations restricted to be 45^o from the film/substrate interface.

Koukhar *et al.* (2001) developed the Landau-Ginsburg-Devonshire-type theory taking into account the mechanical substrate effect on the polarizations and lattice strain in dissimilar elastic domains.[14] The strain phase diagram (figure 5.1(a)) shows a small region of direct transformation from paraelectric to ferroelectric *c*/*a*/*c*/*a* domain pattern when the misfit- strain ranges near $S_m = 0$. At negative in-plane strain region occurs a homogeneous *c* phase at temperature near paraelectric phase, which allows the nucleation of *a*-domains forming *c*/*a*/*c*/*a* pattern of domains. At positive in-plane strain region, the $a_1/a_2/a_1/a_2$ polarization configuration is most favorable in PTO films. At critical temperature in this region, the *c* domains nucleate into the $a_1/a_2/a_1/a_2$ regions. The transformation from *c*/*a*/*c*/*a* to $a_1/a_2/a_1/a_2$ state is a first order transformation. The ferroelectric-to-paraelectric transformation is second order in the positive and negative misfit region except near $S_m = 0$.

Li et al. (2001) tried phase-field numerical approach to obtain domain stability phase diagram for (001) PTO thin films in three-dimension. Figure 5.1(b) shows the effect of substrate constraint and temperature on the domain volume fraction. Large compressive strain can form 180° *c*-domains in the film where as high tensile strain favors a_1/a_2 domains. Thus, depending on the mismatch strain and the temperature, the domain structure can be single *c*-domain or *c*/*a*/*c*/*a* or $a_1/a_2/a_1/a_2$ pattern. [16,148]

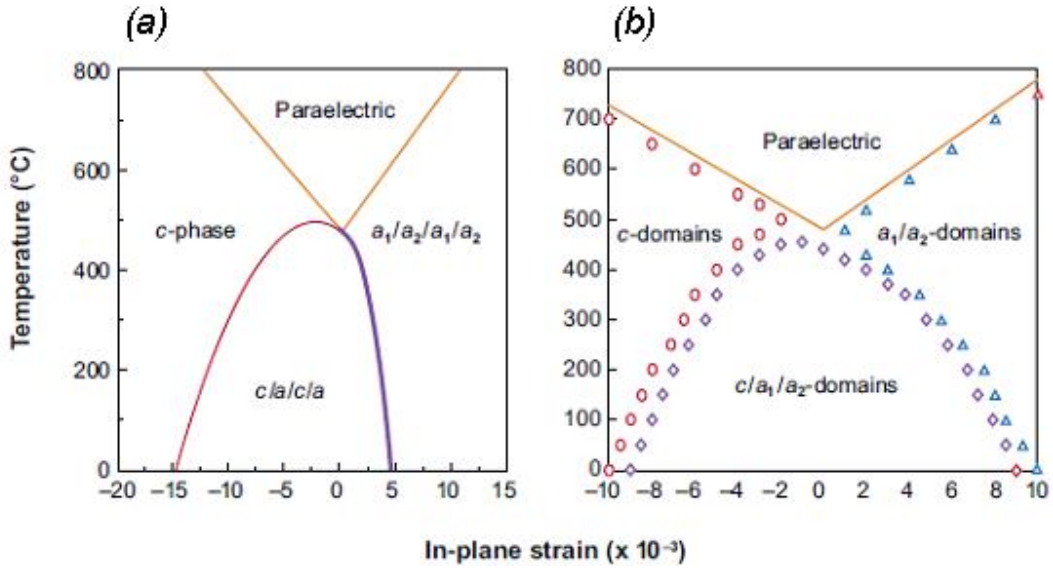

Figure 5.1. Strain-phase diagram of $(001)_p$-oriented PTO on cubic substrate. (a) Single- and double-domain states with domain-wall orientations restricted to be either 45° or 90° from the film/substrate interface[14]. (b) From 3D phase field simulations that automatically predict the possible multidomain states without assuming the domain-wall orientations[16].

5.2 Preparation of Epitaxial Thin Films

The epitaxial PTO thin film can be grown by different methods like Metalorganic Chemical Vapour Deposition (MOCVD)[68, 90, 91, 92, 93], sol-gel[94], Pulse Laser Deposition (PLD)[95] and rf-magnetron sputtering[96]. Among this different growth process MOCVD has an advantage in terms of preparing larger epitaxial film with high growth rate and good conformal step coverage. The PTO thin film samples used for the present study are prepared through pulsed liquid injection MOCVD technique.

Pulsed liquid injection MOCVD technique uses a vertical hot wall reactor for deposition[97]. A computer controlled injector is used to inject micro-doses of an organic solution containing a mixture of metal-organic precursors into a hot evaporation zone.

The evaporated vapour mixture (precursors + solvent) is carried to a deposition zone by an Ar+O_2 gas flow. Here the precursor feeding rate, vapour and film deposition can be easily controlled. Among the different precursors widely available, $Pb(thd)_2$ and $Ti(thd)_2(O^iPr)_2$ have been used here. The deposition conditions are summarized in table 5.1.

The various deposition conditions like deposition temperature, partial oxygen pressure, deposition pressure, injection frequency, solution concentration and solution composition influence the film growth. SEM and AFM were used to study the morphology of the film. The film thickness is determined by taking the cross sectional image of the film by SEM. Film composition was studied by wavelength dispersion spectroscopy (WDS) using Camera Sx-50. XRD in Bragg-Brentano and Schulz geometries using a SIEMENS D5000 diffractometer with monochromatic CuKα1 radiation (λ = 0.15406 nm) was used to study the crystallization, phase purity, in-plane and out-of plane orientation of the films.[69]

Table 5.1. Deposition conditions for PTO layers grown by PI-MOCVD.

Substrates	$SrTiO_3$(100), $LaAlO_3$(001- in a pseudo-cubic setting)
Substrate temperature (T_{Dep}), ^{0}C	550-750
Evaporation temperature, ^{0}C	280
Transport gas	Ar+O_2
Total gas flow rate, 1/h	60
Oxygen fraction (F_{ox}), %	7 - 50
Total pressure (P_T), Torr	2 - 10
Precursors	$Pb(thd)_2$, $Ti(thd)_2(O^iPr)_2$
Solvent	Toluene
Solution concentration (total, c_T), mol/l	0.02-0.08
Injection frequency (ν_{inj}). Hz	1 or 2
Thickness, nm	100-300

5.3 Substrates used for PTO Thin Films

Substrates have a significant role in determining the properties of thin film as the difference in lattice mismatch determine the strain and domain structure. As it is seen in figure 2.16, a wide variety of substrates are available, which can be selected according to the different applications of the film. The tensile or compressive strain induced by the substrate in the thin film can be determined by comparing the lattice parameters of different substrate and PTO. If the substrate has higher lattice parameters than the film, the film will be under tensile strain and if the lattice parameter of substrate is smaller than the film, the film will have compressive strain. As it is seen in figure 5.1, the tensile strain favors *a*-domains and compressive strain favors *c*-domains formation. IR reflection spectra are used here to characterize the polar phonons in ferroelectric thin films in a broad spectral range. The substrates were provided by CrysTec (Germany) that were grown by Czochralski method.[168]

5.3.1 Lanthanum Aluminate, $LaAlO_3$ (LAO) (100)

Crystalline $LaAlO_3$ (LAO) is a popular substrate used for ferroelectric thin films and high–T_c superconductors.[98,149,150] LAO is a distorted perovskite with cubic-to-rhombohedral PT around 813 K with lattice parameter a_{LAO}=3.789 Å.[151]

PTO thin film on LAO (PTO/LAO) favors the formation of *c*-domains as there is a compressive strain between the film and the substrate. XRD studies show the growth of film in *c*-axis oriented growth plane. The cubic-to-rhombohedral PT of the substrate and the cubic-to-tetragonal phase transformation of the PTO film induce *c*-axis tilt and 90^o domains. The volume of 90^o domains formed indicates the lattice mismatch strain and varies according to different substrates.[73]

The Raman spectra of PTO/LAO of different thicknesses varying from 30 to 460 nm showed the presence of compressive misfit stress. Splitting of the A_1(TO) modes shows the presence of *a*- and *c*-domains in the thin film.[64] Evaluation from the Raman shift of *E*(3TO) mode shows that *a*-domains are more stressed that *c*-domains. High temperature measurements show the vanishing of *a*-domains at 753 K and of *c*-domains at 853 K.[146]

IR reflectance spectra of 55 nm thick PTO/LAO are given in figure 5.2. As the reflectivity spectrum measures the overall reflectivity from the surface, the sample is measured with electric field (E) parallel to [001] and [110] directions. The *E*(TO) and A_1(TO) positions of PTO/LAO are compared with the *E*(TO) and A_1(TO) frequencies of stress-free bulk PTO single crystal given by Foster *et al.* (1993).[138]

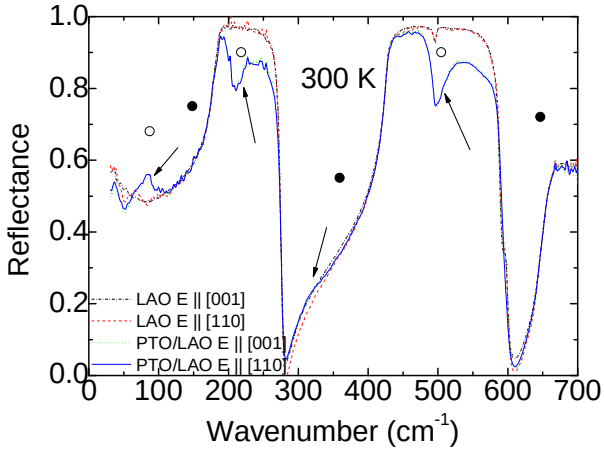

Figure 5.2. Comparison of reflectance spectra of LAO and PTO/LAO when the polarization is parallel to [001] and [110] at RT. Bands related to E-modes of PTO film are shown by arrows. Open and full circle symbols mark positions of E and A_1 modes in the stress-free single-crystal bulk PTO respectively as given by Foster et. al. (1993).

Figure 5.2 shows that the reflectivity of LAO substrate is the same when the E is parallel to [001] and [110] directions. The additional features obtained as a signature of PTO on the reflectance spectra of PTO/LAO are shown by arrows. These features are obtained at *E*(1TO), *E*(2TO), *E*(3TO) and A_1(2TO) positions. Traces of A_1(TO) modes along with the *E*(TO) modes show the presence of *a*-domains in PTO thin film along with the expected *c*-domains.

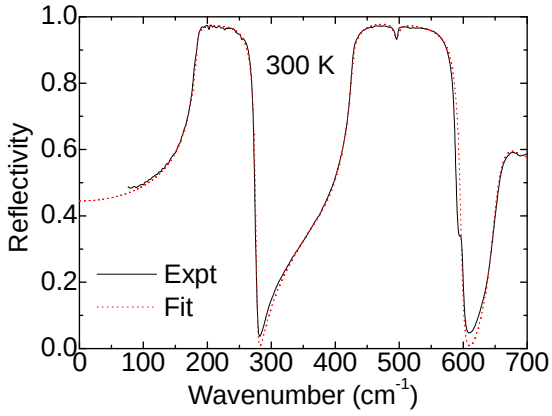

Figure 5.3. Experimental reflectivity data and the corresponding 4-parameter fit of the LAO at RT.

In order to fit the PTO/LAO spectra, the substrate has to be fitted at all temperatures. The reflectivity spectra of LAO were fitted with 4-parameter model using six modes. R*T* reflectivity and the corresponding fit are shown in figure 5.3.

Table 5.2: TO frequencies of LAO at RT obtained by the 3-parameter and 4-parameter fitting models by different authors

	Morel *et al.* (1991)[149]	Calvin *et al.* (1991)[150]	Zhang *et al.* (1994)[169]	Present work
	ε_∞= 2.47	ε_∞= 4.2	ε_∞= 4.0	ε_∞= 4.12
	3-parameter model	3-parameter model	3-parameter model	4-parameter model
ω(1TO)	188	182	184	183.2
ω(2TO)				374.6
ω(3TO)	429	429	428	426.1
ω(4TO)	500	501	496	495.4
ω(5TO)	678	657	652	648.3
ω(6TO)		695	692	710.6

Table 5.2 shows the TO frequencies obtained by different authors by fitting the RT reflectivity of LAO using different fitting models. Zhang et al. (1994) has compared the fits by Morel et al. (1991) and Calvin et al. (1991).149, 150, 169 As compared to the 3-parameter model, which estimates the LO frequencies based on the dielectric strength and damping, the 4-parameter model gives more accurate LO frequencies. As the modes in LAO are broad, it is recommended to use the 4-parameter model.

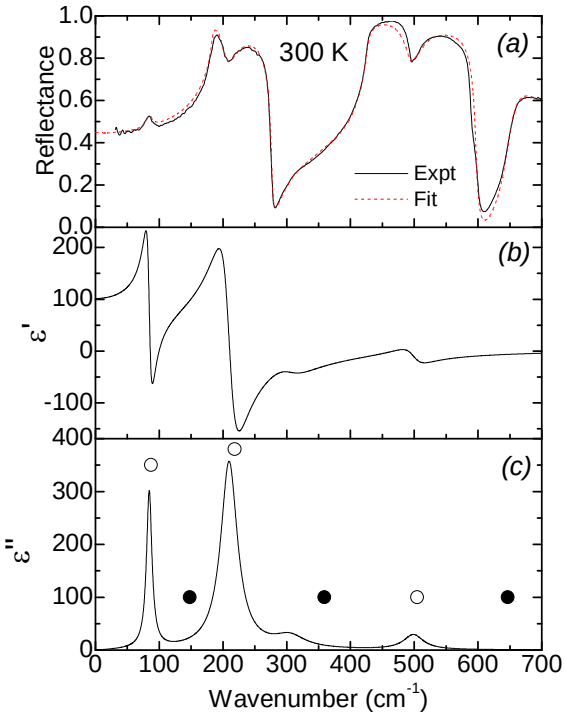

Figure 5.4. PTO thin film on LAO (55 nm) (a) experimental data and fit (b) permittivity and (c) losses. Open and full circle symbols mark positions of E and A_1 modes in the stress-free single-crystal bulk PTO respectively as given by Foster et. al. (1993).

The PTO data were fitted using the 3-parameter model with four modes. The fit, permittivity and dielectric losses obtained are given in figure 5.4. Comparing the TO frequencies obtained by the 55 nm thick PTO/LAO and bulk PTO single crystal frequencies in figure 5.4(c), the TO frequencies are shifted to the lower frequencies at higher modes. Also along with the prominent *E*(TO) modes, traces of A_1(TO) modes are also visible. This gives evidence of the domain structure formed during the thin film formation. Presence of both *E* and A_1 modes indicates formation of c- and a-domains respectively as the thin film passes the paraelectric-to-ferroelectric PT.

5.3.2 (La,Sr)(Al,Ta)O_3 (LSAT) (100)

(La, Sr)(Al, Ta)O_3 (LSAT) is a popular perovskite substrate used for ferroelectric and antiferromagnetic thin films.[152] The lattice parameter is given as a_{LSAT} = 3.869 Å.[155] The powder XRD data show a low temperature structural PT from cubic-to-tetragonal or cubic-to-orthorhombic phase at 150 K.[153] The reflectance spectra of a 55 nm thick PTO/LSAT are compared with the LSAT reflectivity spectra with polarization parallel to [001] and [110] direction in figure 5.5.

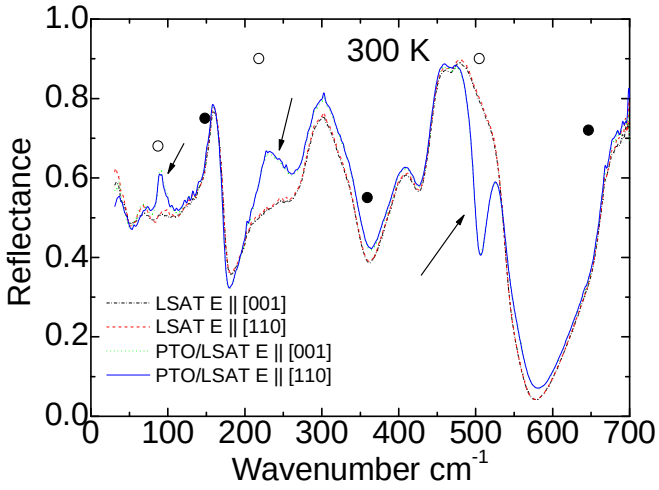

Figure 5.5. Comparison of the reflectance spectra of LSAT and PTO/LSAT (55 nm) when the polarization is parallel to [001] and [110] direction at RT. Bands related to E-modes of PTO film are shown by arrows. Open and full circle symbols mark positions of the E and A_1 modes in the bulk stress-free single-crystal, PTO respectively, as given by Foster et al. (1993).

As the lattice parameter of LSAT is very close to that of PTO, the film has very small misfit strain at R*T*. Thus the reflectance spectra of PTO/LSAT show features that are characteristic of the stress-free bulk PTO single crystal modes. The reflectance spectra are also independent of the polarization.

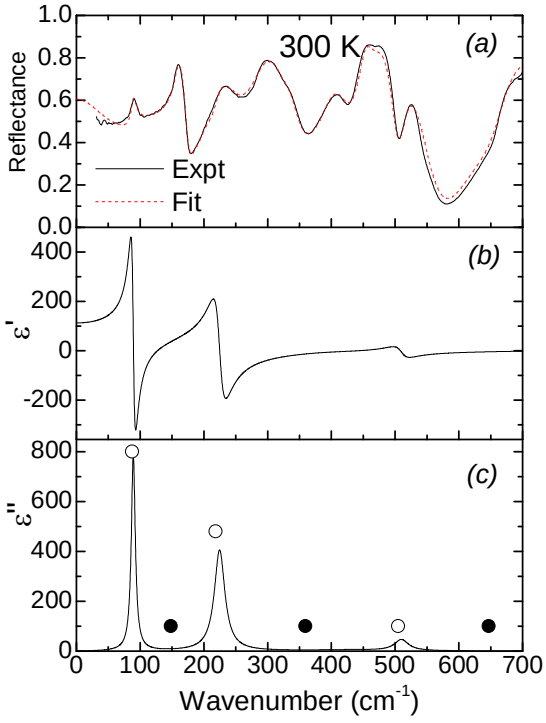

Figure 5.6. PTO/LSAT (55 nm) (a) experimental reflectance data and fit (b) permittivity and (c) losses. Open and full circle symbols mark positions of the E and A_1 modes in the stress-free single-crystal bulk PTO, respectively, as given by Foster et al. (1993).

The fit and the corresponding permittivity and losses of PTO/LSAT are given in figure 5.6. The TO mode positions of the 55 nm thick PTO/LSAT closely resemble the *E*(TO) mode frequencies obtained for stress free bulk PTO single crystal. Thus this film is mainly dominated by *c*-domains.

5.3.3 Magnesium Oxide (MgO) (100)

Magnesium oxide (MgO) is a cubic substrate with the lattice parameter a_{MgO} = 4.212 Å.[63] The PTO/MgO has tensile strain and favors the formation of *a*-domains for thinner films and has compressive strain favoring *c*-domains in thicker film. XRD studies on 250 nm thick PTO/MgO showed *a*-domains and *c*-domains. The lattice parameters in *a*- and *c*-domains are estimated as a_c = 3.92 Å and c_c = 4.13 Å in *c*-domain and a_a = 3.91 Å and c_a = 3.92 Å in *a*-domains. The decrease in tetragonality (*c*/*a*) of thin film as compared to the single-crystal PTO is due to the stress induced by the substrate. Tetragonality of *a*- and *c*-domains are 1.003 and 1.050, respectively. This shows that *a*-domains are more stressed than *c*-domains.

The IR reflectance spectra of 55 nm thick PTO/MgO are compared with the reflectance spectra of MgO in [001] and [110] direction. As MgO has higher lattice parameters than PTO, the PTO thin film will experience tensile stress and will favors the formation of *a*-domains. MgO substrate is transparent below 100 cm^{-1} even at R*T*.

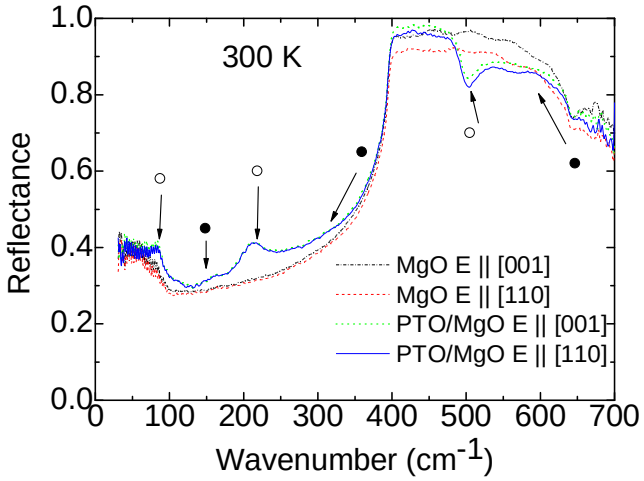

Figure 5.7. Comparison of reflectance spectra of MgO and PTO/MgO (55nm) when the polarization is parallel to (100) and (011) at RT. Bands related to E-modes of PTO film are shown by arrows. Open and full circle symbols mark positions of E and A_1 modes in the bulk stress-free PTO single-crystal respectively, as given by Foster et al. (1993).

In figure 5.7, the signature of *a*-domains are well seen around 150 cm^{-1} and 300 cm^{-1} as there is more contribution from the A_1(TO) modes. This shows the effect of tensile stress. The shift in frequencies is due to the stress experienced by the substrate but the domain structure might be quite complicated.

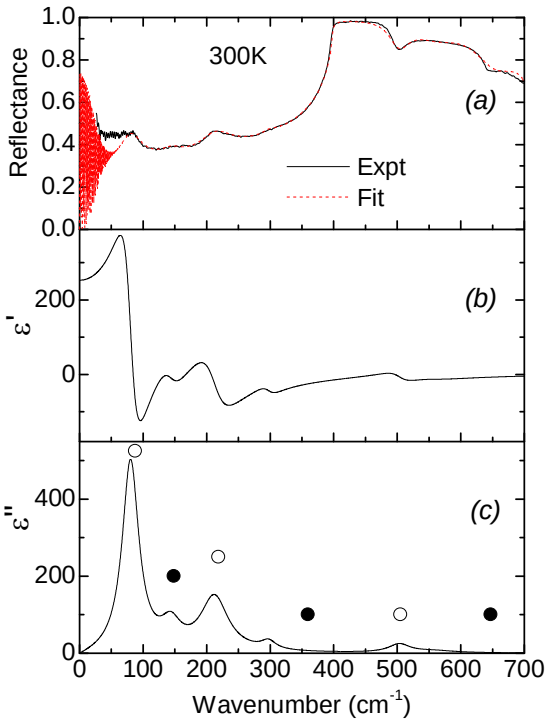

Figure 5.8. PTO/MgO (55 nm) (a) experimental data and fit (b) permittivity and (c) losses. Open and full circle symbols mark positions of E and A_1 modes in the bulk stress-free single-crystal PTO, respectively, as given by Foster et al. (1993).

The MgO substrate reflectivity is fitted with two oscillators and the corresponding PTO/MGO by six modes. Additional modes are used to fit the features related to A_1(TO) modes of the PTO/MgO. Figure 5.8 shows the reflectance fit along with the real and imaginary part of the permittivity. The reflectance fit of PTO/MgO shows clear evidence of the *E*(TO) and A_1(TO) modes. This shows the possibility of formation of both *a*- and *c*-domains.

5.3.4 $NdGaO_3$ (NGO)

$NdGaO_3$ (NGO) is a popular substrate due to its low losses. At R*T* NGO has orthorhombic structure with the space group *Pbnm*. The in-plane lattice constants are found to be $a_{NGO} = b_{NGO} = 3.865$ Å and out-of-plane lattice spacing $c_{NGO} = 3.3.857$ Å in NGO (110) .[155, 156]

The in-plane compressive strain favors the formation of *c*-domains in this PTO thin film. In Raman spectra of PTO/NGO all the Raman peaks show phonon-mode hardening behavior as compared with the PTO single crystal (Burns *et al.* (1970)[139]). Thus for an epitaxial thin film the shifts in phonon modes give evidence of a remnant stress[65]

IR reflectance spectra of the 55 nm thick PTO/NGO are given in figure 5.9. The IR anisotropy of the NGO substrate is very pronounced as is well seen in the reflectance spectra. Signature of the *E*(TO) modes, characteristic for PTO bulk single crystal, is also well seen in the reflectance spectra of PTO/NGO.

Nuzhnyy *et al*. (2011) have fitted the reflectivity spectra of NGO for E ‖ (001) with the 4-parameter model using 10 modes at low temperature and 9 modes at R*T* and higher. The reflectivity spectra of NGO for E ‖ (110) are fitted using 17 modes at low temperature and 15 modes at R*T*.[156] PTO/NGO for E ‖ (001) and E ‖ (110) plane are fitted using 4 modes that correspond to the PTO. The fits of permittivity and losses along the (001) and (110) polarization are given in figure 5.10 [A] and [B] respectively.

The TO mode frequencies obtained by fitting the PTO/NGO along E ‖ (001) and E ‖ (110) correspond well to the *E*(TO) modes observed by Foster *et al.* (1993). The contribution from A_1(TO) modes is hardly seen. Thus the *c*-domains formation during the PT is prominent.

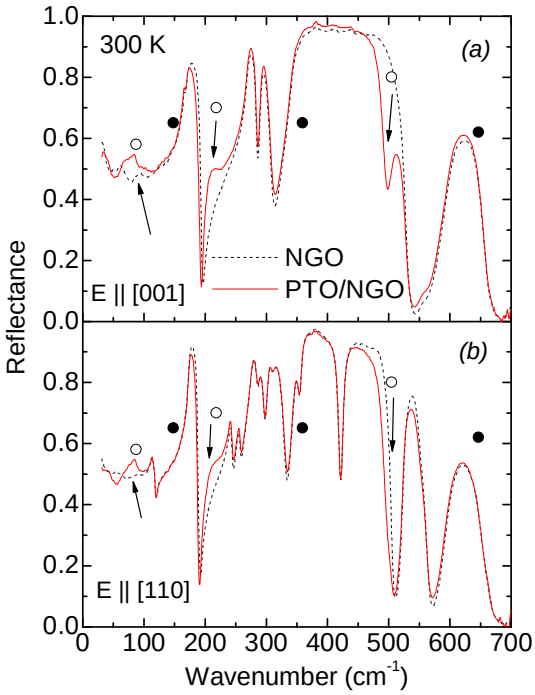

Figure 5.9. Comparison of reflectance spectra of NGO and PTO/NGO (55nm) (a) the polarization is parallel to (001) and (b) the polarization is parallel to (110) at RT. Bands related to E-modes of PTO film are shown by arrows. Open and full circle symbols mark positions of E and A_1 modes in the bulk stress-free single-crystal PTO, respectively, as given by Foster et al. (1993).

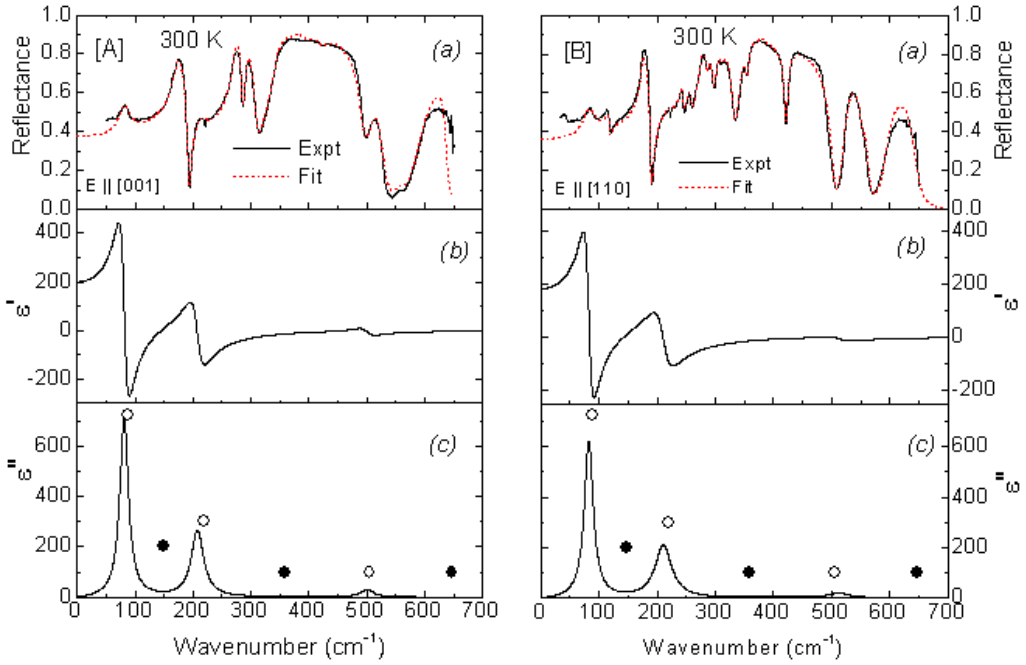

Figure 5.10. PTO thin film on [A] NGO (001) and [B] NGO (011) at T = 300 K (55 nm) (a) experimental data and fit (b) permittivity and (c) losses. Open and full circle symbols mark positions of E and A_1 modes in the stress-free single-crystal bulk PTO, respectively, as given by Foster e. al. (1993).

5.3.5 Strontium Titanate $SrTiO_3$ (100), (110) and 0. 5 % Nb doped (111)

$SrTiO_3$ (STO) is a cubic perovskite structure at R*T* with space group $Pm3m(O^1_h)$. The lattice parameter is a_{STO} = 3.905 Å. STO undergoes a structural PT from cubic-to-tetragonal phase at 105 K.[158] STO surface is widely used as a substrate for ferroelectric thin films, high temperature superconductor thin films and in photoelectrolysis.[159, 160, 161, 162] Studies of same film on different STO surfaces have shown difference in their properties.[161, 162] Doping STO(111) with 0.5 % Nb introduces conductivity in the substrate, without changing the lattice parameters.[52] STO being paraelectric at R*T* is a good candidate for studying the defects by doping as the domain formation is avoided.
XRD studies of PTO thin film grown on insulating STO substrate have revealed periodic 180^0 stripe domains with film thicknesses from 12 to 420 Å.[164, 165] For PTO grown on conductive Nb-doped STO substrate, the XRD studies show a decrease in tetragonality for film thickness below 200 Å. This is marked as a signature of progressive suppression of the ferroelectricity in ultrathin films.[166] In the 250 nm PTO/STO(001), Raman studies show that the PT temperature is shifted to 923 K. At R*T* this film is tetragonal with c/a/c/a domain pattern.[71]

IR reflectance spectra of 55 nm thick PTO film on STO substrates of different orientations at *T* = 300 K are given in figure 5.11. Figure 5.11 (a) shows the reflectance spectra of 55 nm thick PTO/STO(100) plane and the reflectivity spectra from the STO(100) substrate at R*T*. There is no significant difference in the substrate and the film when the polarization is along (001) and (110) direction. *E*(2TO) and *E*(3TO) modes from the PTO are seen as compared to the STO(100) substrate.

The reflectance spectra of PTO/STO(110) substrate and the reflectivity spectra of STO(110) substrate are given in figure 5.11 (b). Here the reflectivity spectra of the substrate are independent of the polarization. The corresponding reflectance spectra of the PTO thin film are anisotropic. For the polarization along (001) the *E*(2TO) mode is much broader and shifted towards higher frequency. The *E*(TO) modes are prominent for the polarization along the (110) direction. Here the *E*(2TO) mode is shifted towards lower frequency as compared to PTO/STO(100).

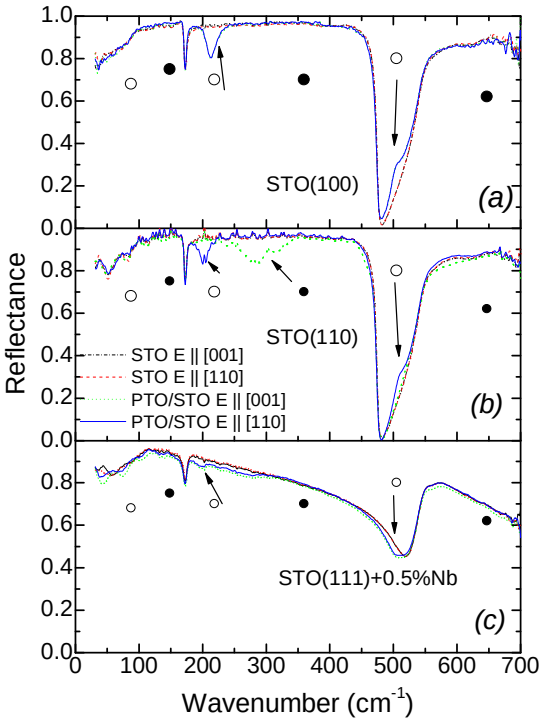

Figure 5.11. Reflectance spectra of 55 nm PTO thin film (a) on STO(100), (b) on STO(110) and (c) on STO(111) doped with +0.5% Nb when the polarization is parallel to (001) and (110) directions at RT. Bands related to E-modes of PTO film are shown by arrows. Open and full circle symbols mark positions of E and A_1 modes in the stress-free single-crystal bulk PTO, respectively, as given by Foster et al. (1993).

The comparison of reflectance spectra of the PTO/STO(111)+0.5 % Nb and reflectivity spectra of the STO(111)+0.5% Nb substrate is given in figure 5.11(c). From figure 5.11 (a) and (b), it is seen that the reflectivity spectra of STO(100) and STO(110) are the same, as expected. But in figure 5.11(c) the reflectivity spectra of STO(111) doped with 0.5 % Nb are very different. The thin film has only a weak signature of *E*(TO) modes, which are very broad.

The STO substrates were fitted with the *4*-parameter model using four oscillators, appreciably broader in the case of doped STO. Figure 5.12 shows the fit of PTO/STO(100) and the corresponding permittivity and loss spectra.

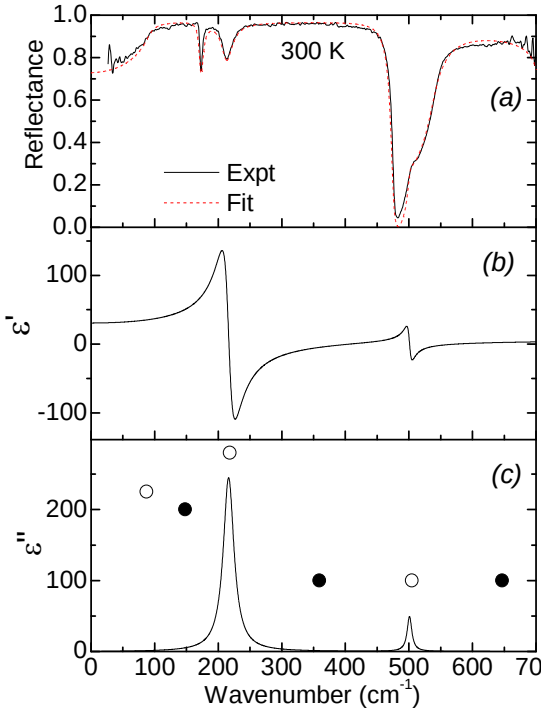

Figure 5.12. PTO/STO(100) (55 nm) at T = 300 K (a) experimental data and fit (b) permittivity and (c) losses. Open and full circle symbols mark positions of E and A_1 modes in the stress-free single-crystal bulk PTO, respectively, as given by Foster et al. (1993).

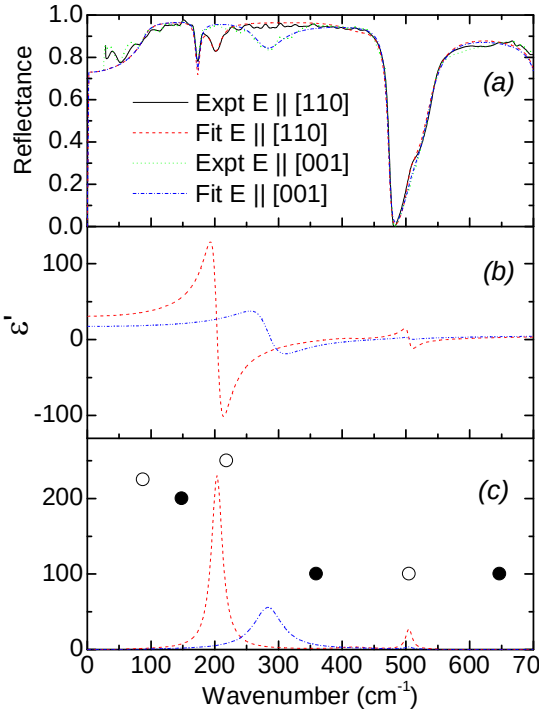

Figure 5.13. PTO/STO(110) (55 nm) at T = 300 K along E || (110) and E || (001) direction (a) experimental data and fit (b) permittivity and (c) loss spectra. Open and full circle symbols mark positions of E and A_1 modes in the bulk stress-free single-crystal PTO, respectively, as given by Foster et al. (1993).

The reflectance spectrum of PTO/STO(100) show prominent feature from *E*(2TO) and *E*(3TO) modes that correspond to those of PTO single crystal. These spectra are fitted with the *3*-parameter model and shown in figure 5.12. A_1(TO) modes are not seen, thus the possibility of finding *a*-domains is very small at R*T*. Although the *c*/*a*/*c*/*a* pattern of domains is observed in the 250 nm thick PTO/STO(100) at R*T*, the 55 nm thick film is favoring *c*-domains as they are more strained than the thicker film.[71]

As seen in figure 5.11 (b), there is an anisotropy of the PTO/STO(110) for polarization parallel and perpendicular to the *c*-axis. Spectra of the PTO/STO(110) along both directions together with their fits are shown in figure 5.13. The difference between these two spectra mainly exist in the position and strength of the *E*(2TO) mode. For the

polarization along (110) the *E*(2TO) mode is stronger and is shifted to lower frequency as compared to the *E*(2TO) mode position given by Foster *et al*. (1993). The *E*(2TO) mode obtained for polarization along the *c*-axis is shifted almost by 60 cm^{-1} as compared to *E*(2TO) mode of the bulk PTO single crystal. This shift in the mode frequency can be due to the influence of the A_1(2TO) mode. Thus for the PTO thin film on STO(110) a complex domain pattern is expected with both *a*- and *c*-domains.

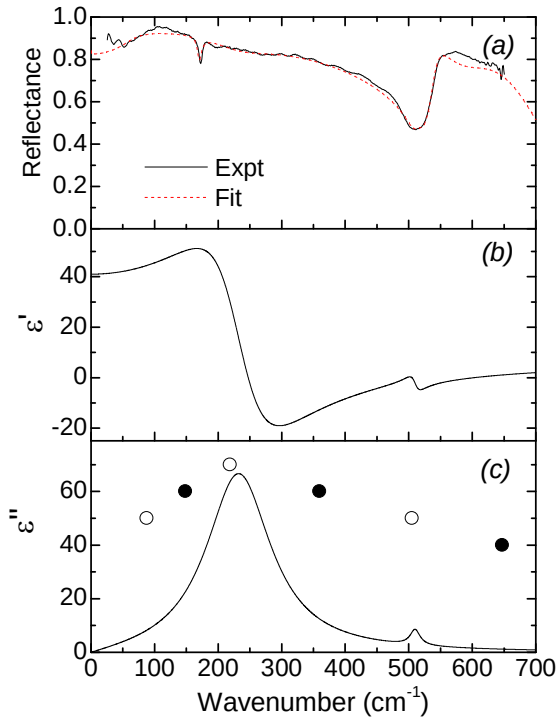

Figure 5.14. PTO/STO(111) (55 nm) doped with 0.5 % Nb at T = 300 K (a) experimental data and fit (b) permittivity and (c) losses. Open and full circle symbols mark positions of the E and A_1 modes in the bulk stress-free single-crystal PTO, respectively, as given by Foster et al. (1993).

The features seen in the PTO/STO(111) + 0.5 % Nb are broader and weaker as compared to above mentioned PTO thin films, as shown in figure 5.14. These features are fitted using the *3*-parameter model. This film has a lower static permittivity and mode strength as compared to the other PTO thin films. Thus the features are not so prominently seen as in the above discussed PTO thin films. The loss spectra show signature of *E*(2TO) and *E*(3TO), but they are difficult to analyze.

5.4 Film Thickness

Thin films can be prepared of different thicknesses. Film thickness plays a significant role in determining the properties of thin film. The thinner films could be

more stressed than the thicker films. The residual stress due to the mismatch with the substrate relaxes as the film thickness increases. Film thicknesses above 125 nm are less substrate dependent and the tensile stress relaxes by forming the *a*-domains. The thin films are further relaxed by dislocations as the thickness approaches 460 nm and the *a*-domain fraction decreases.[71]

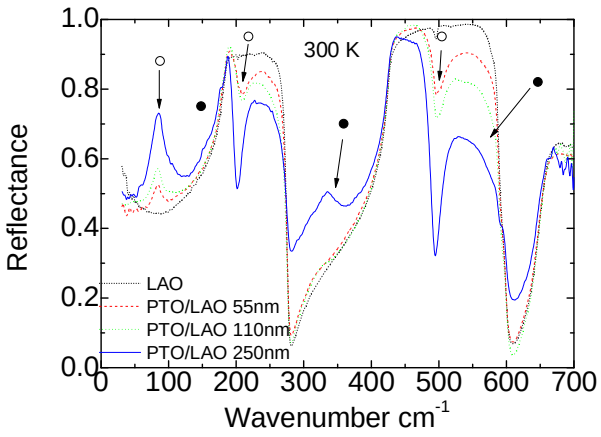

Figure 5.15: Comparative study of the unpolarized reflectance spectra of PTO thin films of different thicknesses on the LAO substrate , namely of 55 nm, 110 nm and 250 nm. Bands related to E-modes of PTO film are shown by arrows. Open and full circle symbols mark positions of E and A_1 modes in the bulk stress-free single-crystal PTO, respectively, as given by Foster et al. (1993).

Figure 5.15 shows the comparison of LAO substrate reflectivity and reflectance of PTO/LAO of three different thicknesses, namely 55 nm, 110 nm and 250 nm. The signature of *E*(TO) and A_1(TO) modes is seen, they correspond to the PTO bulk single crystal and are more prominent as the film thickness increases. This indicates the complex domain pattern developing in the thin film as the thickness increases when the film starts to relax resulting in a higher volume percentage of the *a*-domains.

5.5 Discussion

The above sections give an overview of the PTO thin films prepared on different substrates, namely LAO, LSAT, MgO, NGO, STO(100), STO(110) and STO(111) doped with 0.5 % Nb. PTO thin films on LAO, LSAT, MgO, STO(100) and STO(111) + 0.5 % Nb are isotropic. IR spectroscopy shows anisotropy for the PTO thin films on NGO and STO(110). In the PTO/NGO, the anisotropy is due to the difference in lattice parameters of the NGO substrate. In the case of PTO/STO(110), the anisotropy in the thin film exists due to the anisotropic film growth character on the STO(110) plane.

The main characteristics including the lattice parameters, misfit strain, thermal strain etc., for each substrate and bulk PTO are summarized in table 5.3. Based on the

lattice mismatch between the thin film and the substrate, the maximum misfit strain is reported for PTO/MgO and the minimum for PTO/LAO. The PTO thin films on LSAT, NGO and STO substrates are less strained than PTO thin film on MgO and LAO by comparing their misfit strains. Thermal strain is characteristic for each substrate. LSAT has the smallest thermal strain compared to other substrates.

Table 5.3. Characteristics of all substrates and of bulk PTO single crystal along with misfit strain and thermal strain for all film substrate system.

Material	Crystal structure	Surface cut parallel to	Lattice Parameters (Å)		Misfit strain at R*T* (%)		Misfit strain at T_{dep}(%)	Thermal strain (%)
			At R*T*	At T_{dep}	With PTO *a*-axis	With PTO *c*-axis		
PTO	Cubic-to-tetragonal at 763 K		a=3.899 c=4.153	3.974				-1.9 +4.5
LAO	Cubic-to-rhombohedral at 813 K	(001)	3.789	3.814	-2.9	-9.6	-4.2	-0.659
LSAT	Cubic-to-tetragonal or orthorhombic at 150 K	(100)	3.869	3.890	-0.7	-7.3	-2.1	-0.542
MGO	Cubic	(001)	4.212	4.251	+7.4	+1.4	+6.5	-0.925
NGO	Orthorhombic at R*T*	(110)	a=3.865 c=3.857	a=3.89 c=3.9	-0.8 -1.0	-7.4 -7.6	-1.9 -1.8	-0.87 -1.11
STO	Cubic-to-tetragonal at 105 K	(100) (110)	3.905 3.905	3.932 3.932	+0.1 +0.1	-6.3 -6.3	-1.1 -1.1	-0.691 -0.691
STO +0.5% Nb	Cubic to tetragonal at 105 K	(111)	3.905	3.932	+0.1	-6.3	-1.1	-0.691

The mode positions obtained for all PTO thin films on different substrates are compared with the mode frequencies of bulk PTO single crystal in table 5.4. The TO mode positions are obtained from the peak in imaginary part of the complex permittivity. The LO positions are calculated from the -Im[1/ε] response function. The TO and LO mode positions are assigned based on stress free bulk PTO single crystal obtained by Foster *et al.* (1993). Some extra modes were found, which could not be accommodated to the mode frequencies of PTO single crystal. These extra modes are contribution due to a complex domain structure formed in PTO thin films as the films pass the PT temperature.

Table 5.4. Mode frequencies obtained for bulk PTO single crystal and 55 nm thick PTO thin films on LAO, LSAT, MgO, NGO, STO (100), STO (110) and STO (111)+ 0.5 % Nb.

	PTO (Foster et al. 1993)	PTO/LAO	PTO/LSAT	PTO/MgO	PTO/NGO		PTO/STO (100)	PTO/STO (110)		PTO/STO (111) +0.5% Nb
					[001]	[110]		[001]	[110]	
E(1TO)	87.5	84.261	89.16	80.29	80.99	82.16	-	-	-	
E(2TO)	218.5	209.60	224.54	211.70	207.50	210.3	215.90	283.5	203.5	232.2
E(3TO)	505	498.56	509.77	503.70	500.66	512.1	502.76	504.4	504.6	509.7
E(1LO)	128	101.53	127.44	128.61	145.18	142.1	170.85	128.3	108.5	
E(2LO)	440.5	459.12	441.38	460.05	453.51	461.4	477.09	480.5	442.0	488.9
E(3LO)	687						660.08			611.5
A_1(1TO)	148.5									
A_1(2TO)	359.5	299.93		142.14						
A_1(3TO)	647									
A_1(1LO)	194									
A_1(2LO)	465			168.99						
A_1(3LO)	795									
B_1+E	289	299.93 (TO) 298.06 (LO)		295.96 (TO) 289.66 (LO)						
Extra				554.585 (LO)				526.3 (LO)	388.1 (LO) 573.7 (LO)	

Mode frequencies and their shift show that the PTO thin films on LAO and MgO have contribution from both *E*(TO) and A_1(TO) modes indicating a complex domain pattern. As the MgO is transparent even at R*T* below 100 cm^{-1}, PTO thin film on MgO needs a detail measurements in reflection and transmission modes to study the position of the *E*(1TO) mode. PTO thin films on LSAT, NGO(001), NGO(110) and STO(100) have mainly the *c*-domains as the contribution from A_1(TO) modes is negligible. PTO thin film on STO(110) for *E* along the (001) and (110) directions show a shift in the *E*(2TO) mode frequency. Irrespective of the wide possibility of investigating the details of each film substrate system, this work concentrates on the PTO/LAO, as these films have high misfit strain and a complex *a*- and *c*-domain pattern.

Publication Related to this work:-

A. Bartasyte, S. Margueron, J. Santiso, J. Hlinka, E. Simon, I. Gregora, O. Chaix-Puchery, J. Kreisel, C. Jimenez, F. Weiss, V. Kubilius, A. Abrutis, Domain Structure and Raman modes of $PbTiO_3$, Phase Transition, 84 509-520 (2011).

CHAPTER 6 Lead Titanate Thin Film on Lanthanum Aluminate Substrate

6.1 Introduction

PTO thin films are typically grown above paraelectric-to-ferroelectric PT. As the film passes from high-symmetry phase to low symmetry phase, domain formation helps to relax the thermal strain and misfit strain during the PT.[61, 167] Formation of domains, therefore, is inevitable in most cases. Obviously, domain structure significantly influences the properties of films.

The aim of this chapter is to check to which extend the spectroscopic and PFM techniques can be useful for inspecting the presence of domain patterns in PTO/LAO in detail. Previously, PTO/LAO were investigated using XRD and Raman spectroscopy by Bartasyte *et al*., (2007, 2008, 2009, 2011).[63, 64, 68, 69, 70, 116] Our work was dedicated to study of 250 nm and 100 nm thick PTO thin films grown epitaxially on LAO substrate using IR spectroscopy, Raman spectroscopy and PFM. Theoretical interpretation is also tried using the effective medium approximation.

6.2 Analysis of IR spectra of the 250 nm thick film

Here 250 nm thick PTO/LAO film is measured in the temperature range 10 to 873 K. Its R*T* reflectance spectra are compared with the LAO substrate reflectivity in figure 6.1. The *E*(1TO) mode is seen as a peak around 90 cm^{-1}, while the *E*(2TO) and *E*(3TO) mode positions show a dip in the reflectance spectra around 200 cm^{-1} and 500 cm^{-1}, respectively. The broad peak around 325 cm^{-1} corresponds to A_1(2TO) and A_1(3TO) is given by a reflectance suppression near 550 cm^{-1}. The reflectance spectra on PTO/LAO are quantitatively analyzed using the Fresnel Formulas (section 3.2.3.4) to determine the mode position and understand the domain patterns in more detail.

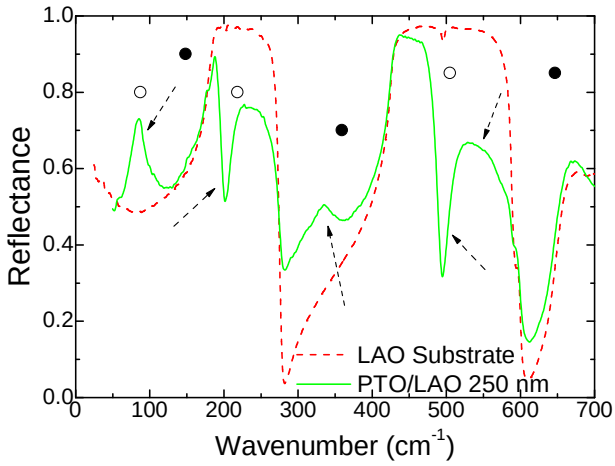

Figure 6.1. RT reflectance spectra of 250 nm thick PTO/LAO and reflectivity spectra of the LAO substrate. Bands related to E-modes of PTO film are shown by arrows. Open and full circle symbols mark positions of E and A_1 modes in the stress-free single-crystal bulk PTO, respectively, as given by Foster et al. (1993).

6.2.1 Fit using Classical Oscillator Model

To fit the reflectance spectra of the 250 nm thick PTO/LAO, classical oscillator (*3*-parameter) model is tried as described in section 3.2.3.1. The film was fitted using 9 damped modes, specifying the frequency, damping and dielectric strength. Figure 6.2 shows the reflectance along with the *3*-parameter fit. The *E*(TO) and A_1(TO) frequencies obtained are in good agreement with the TO mode positions on PTO single crystal. But the fit around 450 cm^{-1} is not perfect. Thus the *4*-parameter model was also tried to obtain a better fit for this thin film.

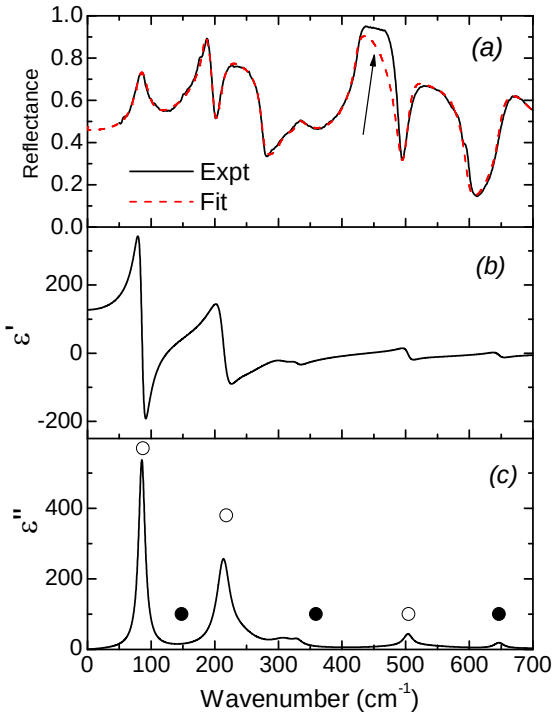

Figure 6.2. 3-parameter fit for 250 nm PTO/LAO. (a) Reflectivity and 3-parameter fit (b) real and (c) imaginary part of the permittivity. Open and full circle symbols mark positions of E and A_1 modes in the stress-free single-crystal bulk PTO, respectively, as given by Foster et al. (1993).

6.2.2 Fit using *4*-Parameter Model

PTO thin film was tried to be fitted using 9 generalized damped harmonic oscillators. The fit along with the real and imaginary part of permittivity is given in figure 6.3. The fit at T = 300 K was good. The peaks in the loss spectra given in figure 6.3(c) correspond to the *E*(TO) modes of the PTO single crystal. Along with *E*(TO) modes, traces of A_1(TO) modes are also seen, which indicates a presence of the *a*-domains in the film.

The fitting parameters at T = 300 K are given in table 6.1. As compared to the 55 nm thick thin film, higher number of modes are required to fit the thicker film, to fit the features related to the domain structure, other than the pure *E* and A_1 modes given by Foster *et al.* (1993).

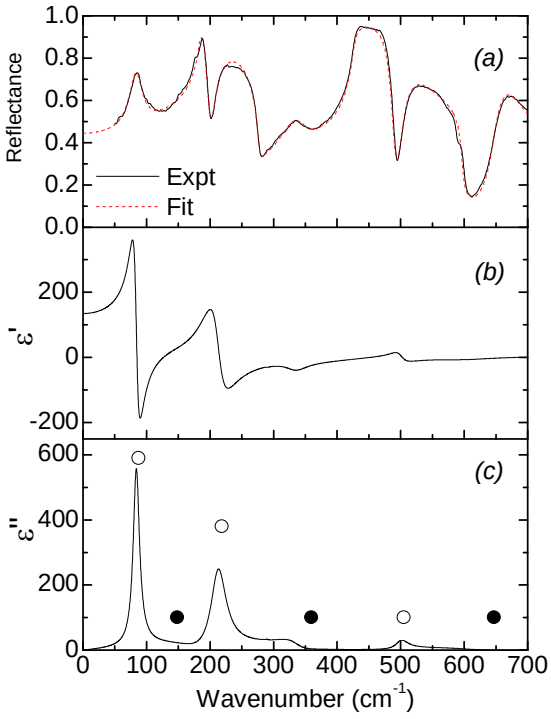

Figure 6.3. 4-parameter fit for the 250 nm PTO/LAO. (a) reflectivity and 4-parameter fit (b) real and (c) imaginary part of permittivity. Open and full circle symbols mark positions of E and A_1 modes in the bulk stress-free single-crystal PTO respectively, as given by Foster et al. (1993).

6.2.3 *4*-Parameter fitting model using parameters of PTO ceramics

The PTO thin film was tried to be fitted using the fitting parameters obtained for PTO ceramics in table 4.2. The corresponding fit is given in figure 6.4(a) and it is seen that the fit is not good. Various parameters like film thickness, dampings (TO and LO) and frequencies (TO and LO) were modified to fit the reflectance spectra in the best possible way, giving the fit as in figure 6.4(b).

The presence of domains in PTO/LAO was studied using XRD and Raman spectroscopy.[116] A detail XRD using two-dimensional (2-D) ω-2Θ mapping showed the presence of *c*-, a_1- and a_2-domains, giving rise to *c*/*a*/*c*/*a* and $a_1/a_2/a_1/a_2$ domain pattern (Section 2.4.1). The effect of *c*-, a_1- and a_2-domains can be seen in the reflectivity spectra, as the overall spectra from the area specified by 3 mm aperture are obtained.

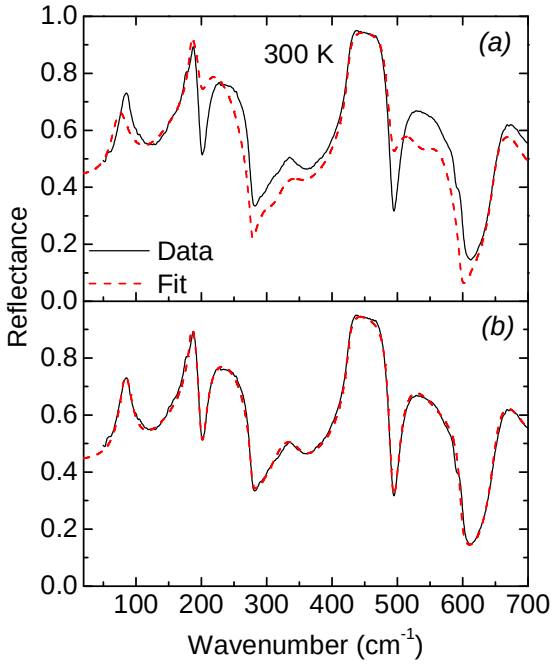

Figure 6.4. 250 nm PTO/LAO at RT (a) fitted with the fitting parameters of the PTO ceramics and (b) fitted using modified parameters (like damping and frequency) of the PTO ceramics.

6.2.4 Temperature Dependence

The temperature dependence of the 250 nm thick PTO/LAO film in the temperature range 10-873 K was studied as described in section 3.2.2. The obtained reflectance spectra were fitted using the *4*-parameter model as descried in section 3.2.3.4 for thin films. The reflectance spectra along with the corresponding fits at various temperatures, namely 10 K, 300 K, 573 K and 773 K are shown in figure 6.5.

Comparing the different reflectance spectra, it is seen that the low frequency peak around 80 cm^{-1} at 10 K moves smoothly down to 60 cm^{-1}. This shows the signature of softening of the soft mode in PTO.

High temperature measurements show that in 250 nm thick PTO film the PT is seen around 773 K. At this temperature in reflectance spectra the traces of A_1 mode around 330 and 550 cm^{-1} are diminishing. This is due to the ferroelectric tetragonal-to-cubic PT. The close resemblance between the T_0 in PTO single crystal and 250 nm thick film gives evidence for the stress relaxation in thicker thin films.

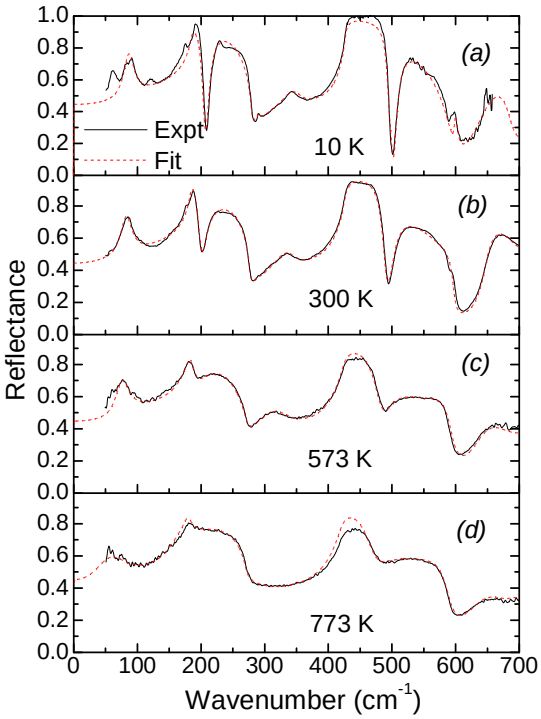

Figure 6.5. Reflectance spectra of the 250 nm thick PTO/LAO along with the fit at (a) 10 K, (b) 300 K, (c) 573 K and (d) 773 K.

The reflectance spectrum at 10 K shows the traces of silent mode at 289 cm^{-1}. The silent mode is seen even in R*T* reflectance spectrum, but at high temperatures this mode vanishes. The real and imaginary part of the permittivity is given in figure 6.6. In figure 6.6 (b), at low temperature *E*(TO) and A_1(TO) mode positions are seen. As the temperature increases, the signature of A_1(TO) mode gets weaker and at 773 K it almost vanishes. This is due to the ferroelectric-to-paraelectric PT. Also the lowest mode, namely the soft mode corresponding to *E*(1TO) mode is softening as the temperature is increased. A shift up to 25 cm^{-1} is seen as the temperature moves from 10 to 773 K.

In figure 6.6(a), the static permittivity appears to be increasing with temperature. Figure 6.9 shows the static permittivity from 10 to 873 K. The drop in the static permittivity at 773 K shows the PT.

The fit of reflectance spectra gives the TO and LO frequency and damping. The TO frequencies obtained for selected temperatures from 10 to 873 K is given in figure 6.8. A smooth change of each mode towards lower frequency is seen as the temperature increases. The silent mode, around 289 cm^{-1}, is seen only till 300 K. At high temperatures, above 623 K, an additional mode appears around 650 cm^{-1}.

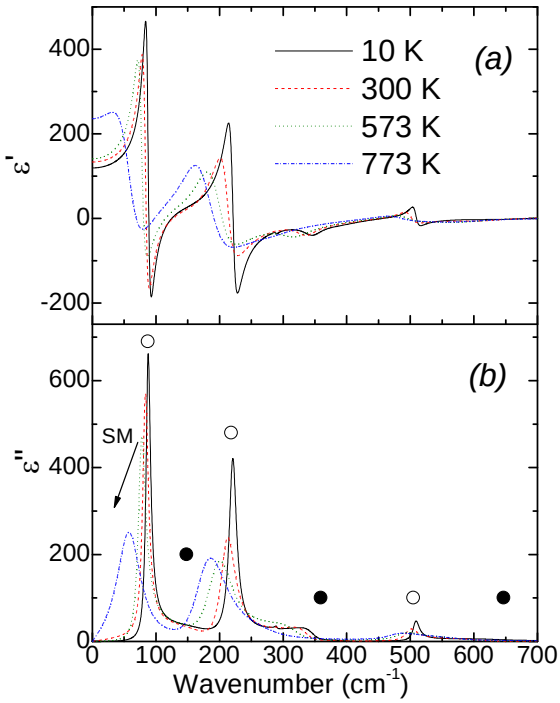

Figure 6.6. (a) Real and (b) imaginary part of permittivity obtained for the 250 nm thick PTO/LAO film at 10 K, 300 K, 573 K and 773 K. Open and full circle symbols mark positions of E and A_1 modes in the stress-free single-crystal bulk PTO, respectively. as given by Foster et al. (1993).

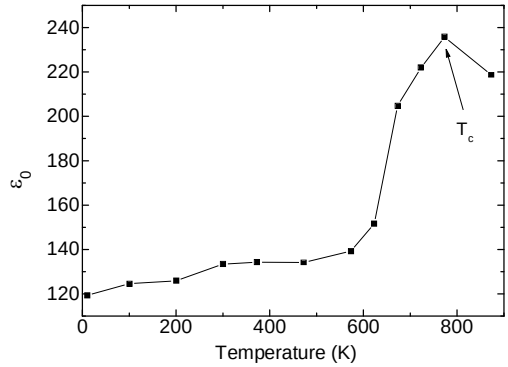

Figure 6.7. Temperature dependent static permittivity obtained from the contribution of all polar phonons.

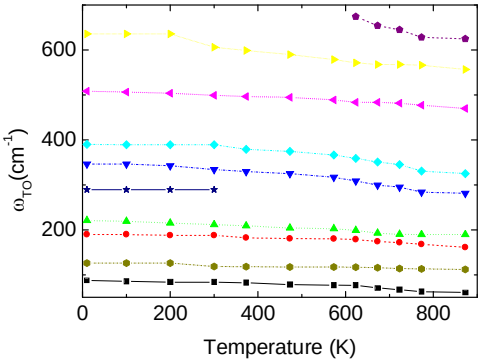

Figure 6.8. Temperature dependence of polar TO phonons frequencies obtained for 250 nm thick PTO/LAO.

Table 6.1. Polar phonon mode frequencies, dampings and dielectric strengths of the 250 nm PTO/LAO film at 10 K, 300 K, 573 K and 773 K.

	ω_{TO}	γ_{TO}	ω_{LO}	γ_{LO}	$\Delta\varepsilon$
10 K	88.14	9	118	46	92
	126	158	178	64	11
	189	78	200	242	1.47
	221	14	327	227	6
	289	4	289	5	0.002
	346	37	360	61	0.35
	390	89	456	9	1.05
	508	12	551	152	0.47
	635	106	683	81	0.41
	-	-	-	-	-
300 K	83.33	10.84	117.9	54.2	112.83
	118.13	205.13	167.12	50.8	1.01
	187.73	92.26	189.1	378	0.46
	211.54	28.5	324.18	158	9.94
	289.35	5.02	289.38	4.83	0.002
	334.25	40.98	349.82	98.9	0.19
	389.2	130.03	451.47	14.5	1.22
	499.09	23.18	532.97	164	0.46
	606.24	107.6	681.99	10.9	0.68
	-	-	-	-	–
573 K	77.15	14.25	116.3	62.04	120.6
	117.21	192.31	159.8	69.59	1.09
	179.94	61.12	183.15	327.84	1.08
	202.38	54.03	293.96	205.59	8.34
	-	-	-	-	-
	316.85	61.47	337	117.44	0.71
	366.3	141.48	444.14	39.95	1.35
	489.02	42.81	491.76	183.15	0.04
	578.76	120.42	678.16	46.47	1.23
	-	-	-	-	-
773 K	62.5	47.96	107.14	33.19	200.58
	113.09	168.04	145.6	92.95	6.78
	168.04	72.11	168.5	358.98	0.31
	189.56	82.19	282.97	148.89	17.86
	-	-	-	-	-
	283.88	93.86	306.78	136.45	0.07
	330.59	153.84	43316	51.16	1.67
	477.11	56.43	483.52	202.84	0.11
	565.94	154.3	626.38	61.24	1.69
	628.21	76.23	714.3	97.07	0.03

6.3. PFM investigations of the 250 nm Thick film

The presence of domains in PTO/LAO was previously studied using XRD and Raman spectroscopy.[116] The effect of *c*-, a_1- and a_2-domains can be anticipated also from the IR reflectivity spectra. Nevertheless, we have been interested in possibility to obtain direct, real space images of ferroelectric domain structures by PFM technique. The PFM images were recorded at ambient conditions using AFM microscope of the Ntegra spectra apparatus of NT-MDT as described in section 3.5. The imaging was done at a 1x1 μm^2 sized area.

Figure 6.9 gives the PFM image obtained for [001] surface of the 250 nm thick PTO/LAO. Figure 6.9(a) gives the vertical PFM image with the maximum contrast between the out-of-plane components of the local spontaneous polarizations. As *c*-domains are areas with out-of-plane spontaneous polarization, the color contrast corresponds to the positive or negative value of *c*-domain. In the vertical PFM image, the *a*-domains have almost zero value as they correspond to the areas with the in-plane spontaneous polarization. Figure 6.9(b) gives the lateral PFM image with the maximum contrast between the in-plane components of local spontaneous polarization. In lateral PFM image the areas of maximum contrast correspond to the a_1-domains as they are aligned along the [100] direction. The *c*- and a_2-domains are given by intermediate contrast.

The areas with wavy boundaries of diameter 200-500 nm with maximum contrast indicate the prevailing inward or upward polarization. The preferential orientation of the spontaneous polarization is almost parallel to the edge of the image, i.e. to pseudocubic axes of the substrate. Some areas are also seen with fine and faint straight boundaries at 45^0 or 135^0 with respect to the edge of the image. Domains along 45^0 or 135^0 with respect to the edge of the image correspond to the a_2-domains, which are along the [010] direction.

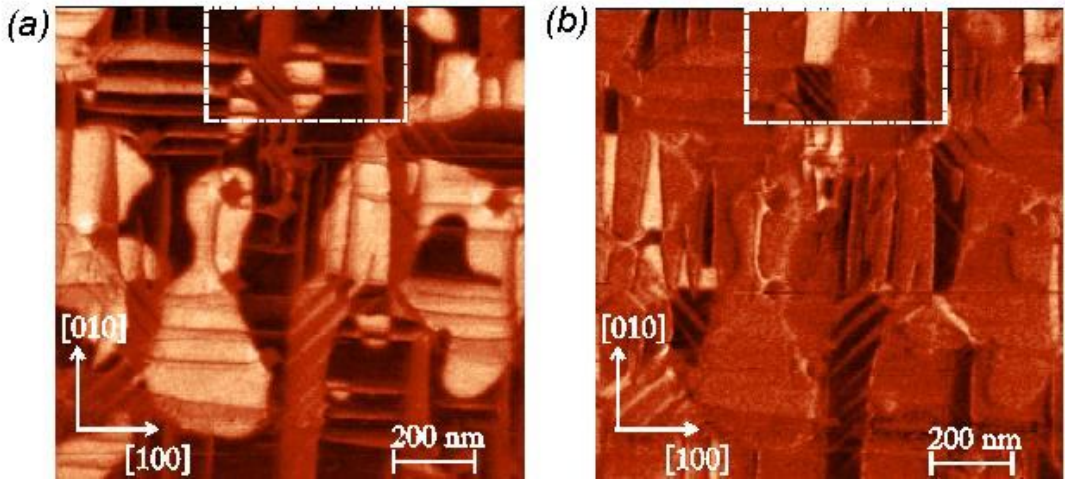

Figure 6.9. PFM image of the 250 nm thick PTO/LAO substrate in the (a) "vertical", i.e. out-of-plane PFM response mode and in the (b) "lateral" PFM response mode i.e. with contrast sensitive to the horizontal axis of the figure. Edges of the scanned area are roughly parallel to the pseudocubic axes of the substrate. The frame indicates the area shown enlarged in figure 6.10.

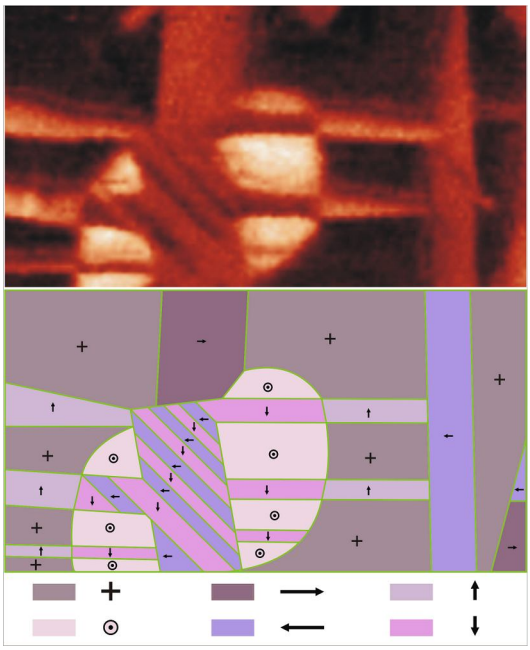

Figure 6.10. Enlarged portion of figure 6.10 along with the schematic suggestion of the assigned domain structure.

Mechanical compatibility condition, which ensures mechanical integrity of the interface (section 2.4.2) helps to understand the geometry of the observed domain pattern.[170] The 180^0 walls are subjected to the electrical compatibility condition, which ensures that there are no bound charges on the interface.[171]

An enlarged portion of figure 6.9 along with the assigned domain states is given in figure 6.10. The lines parallel to [100] and [001] indicate 90^0 ferroelastic walls separating the *c*- and *a*-domains. To have stress free domain wall the *c*- and a_1-domain should be separated by (101) or $(10\bar{1})$ type planar walls (90^0 walls), which intersect the (001) plane of the film along the [010] direction. Thus the a_1 ferroelastic domains tend to appear as (010)-oriented stripes in figure 6.9(b). Thus, comparing the vertical and lateral PFM images, all the four types of domains formations discussed in section 2.4.1 are seen in figure 6.9, namely 180^o *a*-*a* domains, 180^o *c*-*c* domains, 90^o *a*-*c* domains and 90^o a_1-a_2 domains.

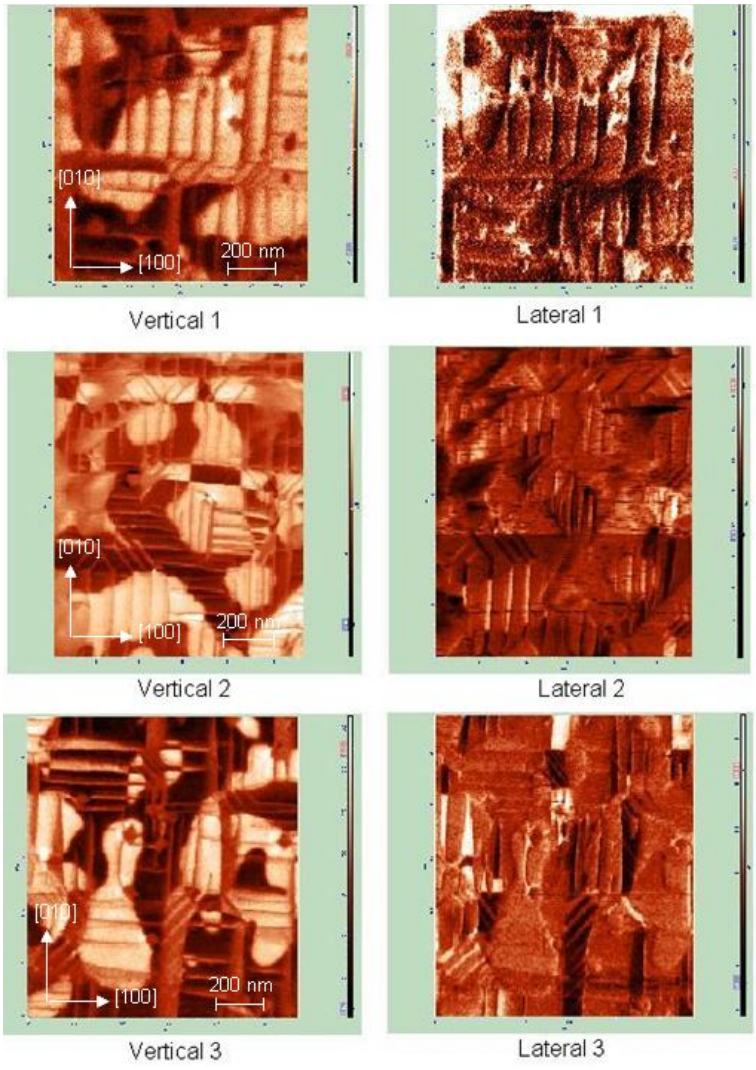

Figure 6.11. Vertical and lateral PFM image obtained for the 250 nm thick PTO/LAO from randomly selected positions.

PFM images collected randomly from different parts of the 250 nm thick PTO film are shown in figure 6.11. All the images show the presence of *c*-, a_1- and a_2-

domains. Different domain patterns, namely *c*/*a*/*c*/*a* and $a_1/a_2/a_1/a_2$, are seen with 180° *a*-*a* domains, 180° *c*-*c* domains, 90° *a*-*c* domains and 90° a_1-a_2 domains.

6.4. IR Data analysis of the 110 nm thick film

The R*T* reflectance spectra obtained from the 110 nm thick PTO/LAO is compared with the LAO substrate reflectivity in figure 6.12. This shows clear signature of PTO thin film even though it is not as prominent as the reflectance spectrum of 250 nm thick film. Special features corresponding to *E*(TO) modes appear around 80, 210 and 480 cm^{-1}. The features due to A_1(TO) modes give the small peak near 330 cm^{-1} and dip near 510 cm^{-1}.

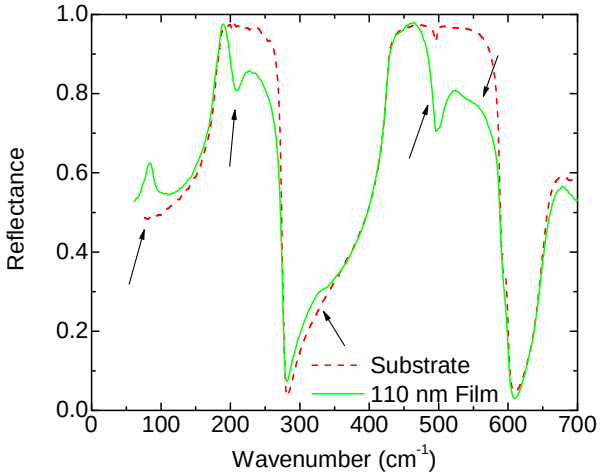

Figure 6.12. Comparison of RT reflectance spectra of the 110 nm thick PTO/LAO and the reflectivity spectra of LAO. Arrows indicate special features corresponding to the E(TO) and A_1(TO) modes in bulk PTO single crystal.

6.4.1 Low temperature IR measurement

The low temperature IR measurement gives a better resolved picture of the phonon modes in the thin film. The low temperature measurements from 300 to 10 K are given in figure 6.13. The *E*(1TO) mode around 80 cm^{-1} softens as the temperature reaches 300 K from 10 K. As expected at low temperatures, the peaks are narrower and sharper.

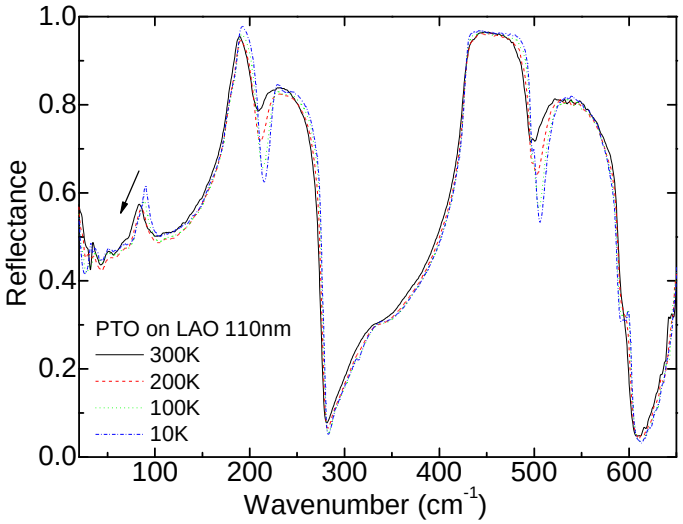

Figure 6.13. Low temperature reflectance spectra of the 110 nm thick PTO/LAO substrate.

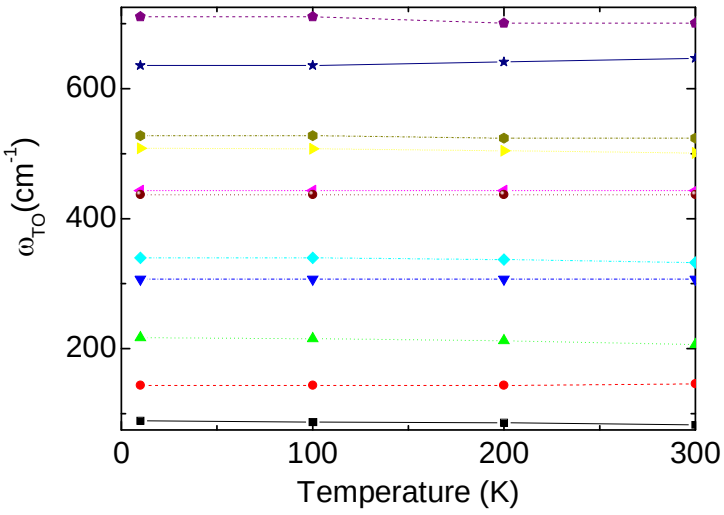

Figure 6.14. Temperature dependence of polar TO phonons frequencies obtained for the 110 nm thick PTO/LAO.

Figure 6.14 gives the TO frequencies obtained from the low temperature measurements 10 to 300 K. 11 damped harmonic oscillators are used to fit these reflectance spectra. It is seen that the TO mode frequencies of the first mode soften from 89 cm^{-1} to 83 cm^{-1} as the temperature increases from 10 to 300 K. This shows the soft mode.

The real and imaginary parts of complex permittivity obtained by fitting the reflectance spectra of the 110 nm thick PTO/LAO from 10 to 300K is given in figure 6.15. As the temperature is increased from 10 to 300 K, the soft mode softens by 6 cm^{-1}.

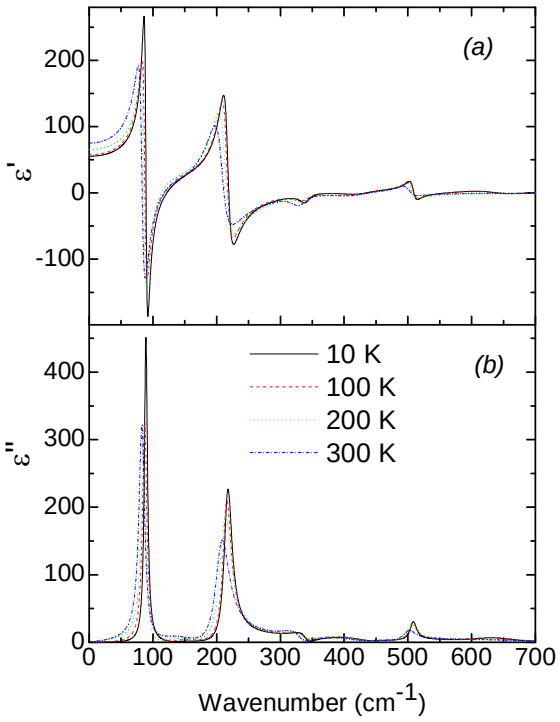

Figure 6.15: (a) Real and (b) imaginary parts of the permittivity of the 110 nm thick PTO/LAO.

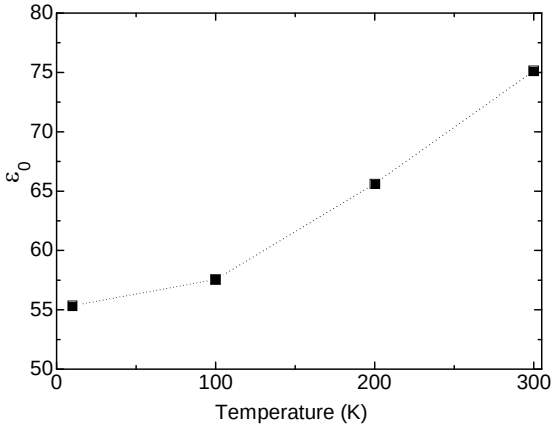

Figure 6.16. Temperature dependent static permittivity obtained from the contribution of all polar phonons for the 110 nm thick PTO/LAO.

Static permittivity given as the sum of ε_∞ and dielectric strengths of all modes, obtained for the PTO thin film in the temperature range 10 to 300 K is given in figure 6.16. The T_0 for this film is expected to be higher than T_0 of the 250 nm thick film as the thinner films are more stressed.[10] Comparing the static permittivities of both the films, it is seen that the static permittivity of the thinner film is almost half of the thicker film one.

6.5 PFM data analysis

PFM imaging turns out to be more difficult for the 110 nm thick PTO/LAO. Figure 6.17 shows the PFM image of it.

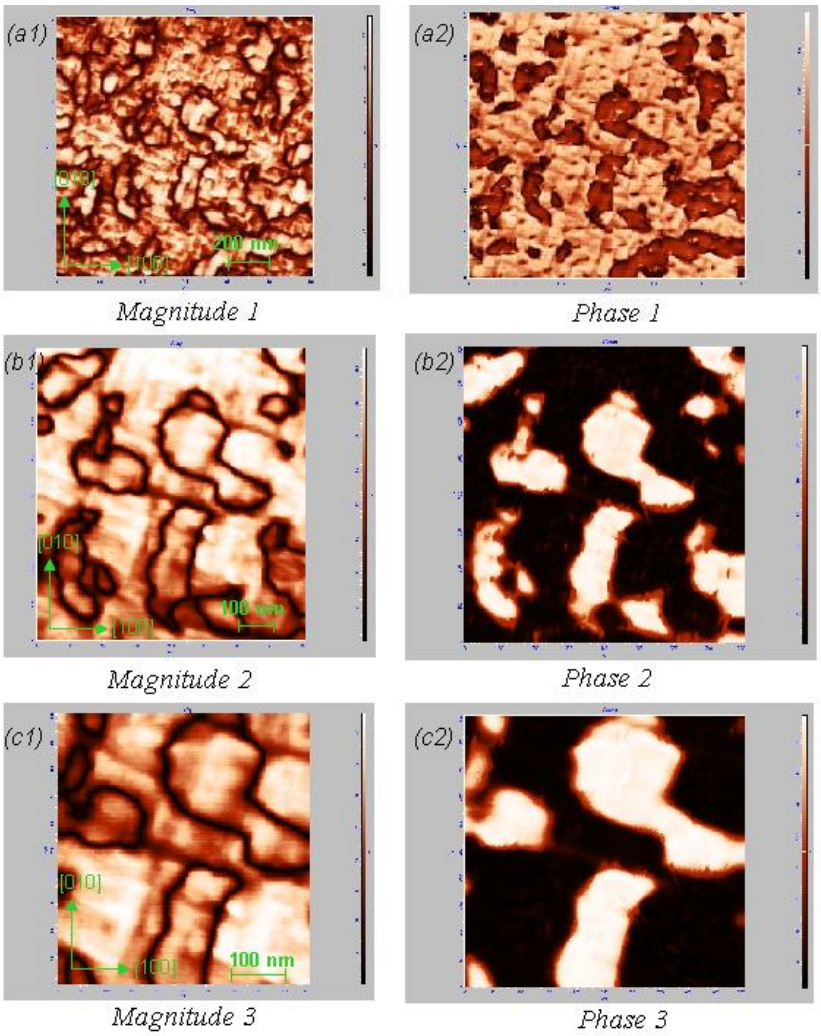

Figure 6.17. PFM images of the 110 nm thick PTO/LAO (a) Vertical magnitude and phase in 1.2x1.2 μm^2 sized area (b) Vertical magnitude and phase in 0.8x0.8 μm^2 sized area and (c) Vertical magnitude and phase in 0.5x0.5 μm^2 sized area.

Figure 6.17(a1) gives the vertical magnitude in 1.2x1.2 μm^2 sized area. The corresponding vertical phase image is given in figure 6.17(a2). The beautiful domain pattern is seen well with small domains. The domain pattern is better resolved by

zooming this area into 0.8x0.8 μm^2 sized area in figure 6.18(b1) and (b2) and 0.5x0.5 μm^2 sized area in figure 6.17(c1) and (c2). The maximum contrast in vertical PFM image gives the up and down position of out-of-plane *c*-domain. The phase PFM image gives the maximum contrast in a_1-domains

6.6 Effective medium approach

A theoretical approximation is done to evaluate the multidomain reflectance spectra of PTO thin film of different thicknesses using Bruggeman effective medium approximation and Lichtenecker mixing formula. These approaches are based on the assumption that the unperturbed dielectric function within each domain is similar to a single crystal one and that there is no preference for the *c*-axis orientation. Here the damping factors of all modes are taken as 25 cm^{-1} as a small damping factor and the ratio between ε_{11} and ε_{33} is taken as 2:1 as 60-70% are *c*-domains. The parameters of PTO are taken from Foster *et al*. (1993).[138]

The simulated normal incidence IR reflectance spectra of PTO/LAO obtained using Bruggeman and Lichtenecker mixing formula are given in figure 6.18. It is seen that the simulated reflectance spectra are similar to the measured reflectance spectra given in figures 6.2 and 6.12. Comparing the figures 6.18(a) and (b), the difference between them indicates that the shape of A_1(TO) bands is rather sensitive to the effective medium formula used.

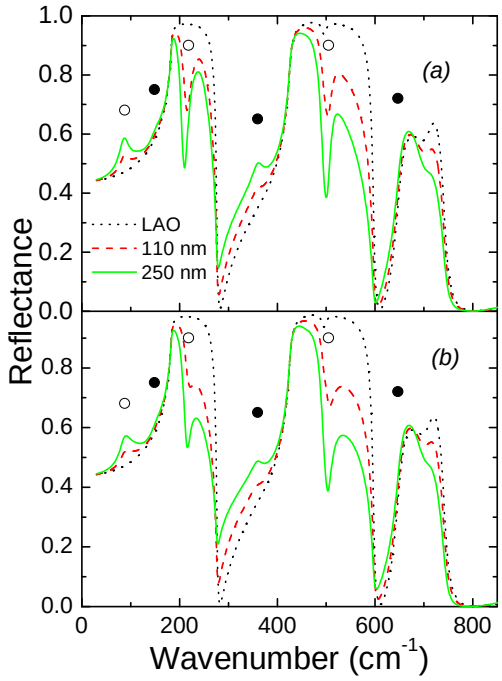

Figure 6.18. Simulated normal incidence IR reflectance spectra of PTO thin films on LAO substrate assuming (a) Bruggeman and (b) Lichtenecker mixing formula for approximation of the effective dielectric function of the hypothetical PTO layer with a completely random distribution of domain orientations. Open and full circle symbols mark positions of E and A_1 modes in the stress-free single-crystal bulk PTO, respectively, as given by Foster et al. (1993).

6.7 Discussion

The IR reflectance spectra of the 250 nm thick PTO/LAO show clear presence of the *E*(TO) modes. The A_1(TO) modes contribute to the high frequency sidebands. As the IR reflectance spectra give the modes with in-plane dipole moment and the dipole moments of A_1 polar modes are parallel to the spontaneous polarization, it is seen that the weak A_1(TO) modes confirm the presence of *a*-domains in the film.

Although the PTO/LAO favors the *c*/*a*/*c*/*a* domain pattern rather than $a_1/a_2/a_1/a_2$ at R*T*, a more complex domain pattern, with all three ferroelastic domain states, is expected in thicker films, which are known as a second-order poly-twin or cellular polydomain state.[172, 173]

The PFM image shows all three ferroelastic domain states arranged irregularly over the sample. In figure 6.10 the horizontal lines on the left show the *c*/*a*/*c*/*a* domain pattern with alternating sequence of *c*- and a_2-domain pattern. The central part of this figure shows $a_1/a_2/a_1/a_2$ embedded in the *c*/*a*/*c*/*a* domain. Similar pattern has been observed previously in a thicker PTO film grown on STO.[174, 175] From figure 6.11 it is

seen that 60-70 % of the scanned area consist of *c*-domains. Similar pattern of domain structure has been reconstructed using the computer simulations.[176]

The IR reflectance spectra given in figure 6.5 (b) and (c) show the presence of A_1(TO) mode sidebands along with the *E*(TO) modes. Thus both *c*- and *a*-domains are present in the film. Comparing the mode frequencies obtained for A_1(TO) side bands, it is seen that the mode frequencies are a bit shifted. For instance, the mode frequency of A_1(2TO) is 359 cm^{-1} in PTO single crystal, but for this thin film the mode frequency is obtained at 336 cm^{-1}. Similar shifts in mode frequencies have already been reported in Raman scattering spectra due to the influence of residual strain.[63, 64] Since the A_1 modes show the presence of *a*-domains, A_1(TO) mode frequencies are influenced by the stress or strain developed in the a_1/a_2 and c/a domain fraction.

As the IR reflectance gives the overall normal incident response of the film, the PFM imaging is used as an additional technique to investigate the complex domain structure in the 250 nm thick PTO film on LAO.

Publication Related to this work:-

1. E. Simon, F. Borodavka, I. Gregora, D. Nuzhnyy, S. Kamba, J. Hlinka, A. Bartasyte and S. Margueron, Investigation of ferroelectric domains in epitaxial $PbTiO_3$ films by piezoresponse force microscopy and far-infrared reflectance, J. Appl. Phys. 110, 084115 (2011).
2. A. Bartasyte, S. Margueron, J. Santiso, J. Hlinka, E. Simon, I. Gregora, O. Chaix-Puchery, J. Kreisel, C. Jimenez, F. Weiss, V. Kubilius, A. Abrutis, Domain Structure and Raman modes of $PbTiO_3$, Phase Transition, 84 (2011) 509-520.

CHAPTER 7 Poled Lead Zirconate Titanate

7.1 Introduction

The search for ferroelectric materials with piezoelectric properties lead to the processing of lead zirconate titanate $PbTi_xZr_{1-x}O_3$ (PZT) from the solid solution of lead titanate (PTO) and lead zirconate (PZO). PZT is widely used in transducers, sonar, medical therapy, actuator applications, capacitors, FRAM, etc.[177] The anisotropy of the ceramic perovskite PZT grains is not well understood as the material is not readily available in the single crystal form.

Lattice Parameters

In PZT the Ti and Zr ions occupy the 'B' sites randomly, giving perovskite structure as seen in figure 1.3. The lattice parameters for PZT around morphotropic phase boundary (MPB) for x =0.48-0.50 are given as a_t = 4.044 Å, c_t = 4.138 Å in the tetragonal phase at R*T*.[178]

Phase Transition

The phase diagram for PZT was first proposed by Jaffe, Cook and Jaffe (1971) as given in figure 7.1.[157] For concentration of x = 0.48-0.50, is the region of MPB where the adjacent phases in the phase diagram have equal Gibbs free energy.[154] There is a coexistence of tetragonal and rhombohedral phase at this concentration. The tetragonal phase has space group *P*4*mm*, with the polar axis along [100] and rhombohedral phase has space group *R*3*m*, with polar axis along pseudocubic [111] direction. The PZT samples near MPB are quiet interesting as they exhibit higher dielectric permittivity, piezoelectric coefficient, electromechanical coupling coefficient, and remanent polarization.[145,157]

In tetragonal phase the domains in PZT can be aligned in six possible directions namely with 90^o and 180^o domain walls, while in rhombohedral phase, as the distortion is along body diagonal, the domains can be aligned in eight domain states with 180^o, 109^o and 71^o domain walls as seen is figure 2.12.

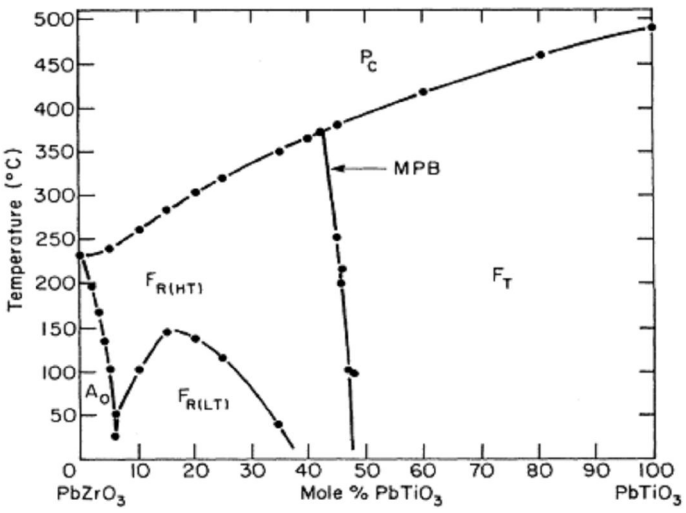

Figure 7.1. Phase diagram of PZT.[157]

PZT phase diagram is discussed especially near MPB also due to the presence of monoclinic phase as reported by Noheda *et al*. (1999).[163]

Hard and Soft PZT

The chemical properties of ferroelectric PZT are highly dependent on doping. Thus PZT can be classified as hard and soft PZT based on the doping and corresponding vacancies. Hard PZT is formed by acceptor-doped system creating oxygen vacancies while soft PZT is formed by donor-doped system creating lead vacancies. As compared to soft PZT, the hard PZT has lower permittivity, lower piezoelectric coefficient, it is difficult to pole, and shows lower resistivity, lower losses, strong aging and is mechanically harder.[17]

7.2 Samples used

The samples were commercially available from American Piezo Ceramics International Ltd., Mackeyville, PA, USA, as 14x7x1 mm^3 sized plates. These included hard (APC 840, APC 841 and APC 880) and soft (APC 850 and APC 856) poled PZT ceramics. These samples had Ti concentration near the MPB (x = 0.48-0.52). The samples were poled at Piezokeramika s.r.o., Librice, Czech Republic, with electric field applied along the plate length and parallel to the plate main surfaces. One main surface was then repolished by SiC (grits 400, 600, 1000 and 1250) and by CEROX 1650.

Images of hard PZT APC880 and soft PZT APC850 taken by a tabletop electron microscope are given in figure 7.2.

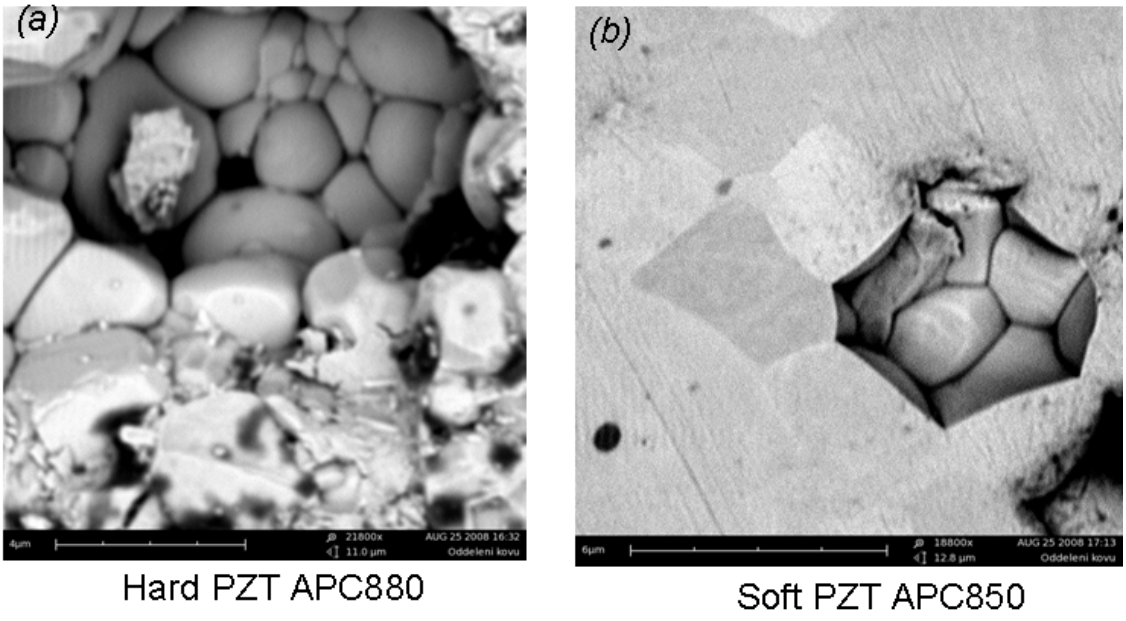

Figure 7.2. Grains observed in (a) hard PZT APC880 and (b) soft PZT APC850.

7.2.1 Poling

Poling is the process of aligning different domains in same direction by a strong electric field. *Depoling* is the process of applying some external force like stress, temperature, etc. to remove the effect of poling. Figure 7.3 shows the process of poling and depoling.

Poling is used to produce single-domain crystals with uniaxial pressing to remove the orthogonal (90^0) domains and then electric field poling to remove the antiparallel (180^0) domains like in BTO.[127] The mechanical poling is done by slowly applying a uniaxial pressure to the crystal, while observing the 90^0 domains in it. By repeating the process alternatively at 90^0, the domains will be aligned in the third direction, along the *c*-axis. To remove the antiparallel 180^0 domains, a DC field in (001) direction is applied, which gradually aligns the polarization in one direction forming a single domain crystal.[128]

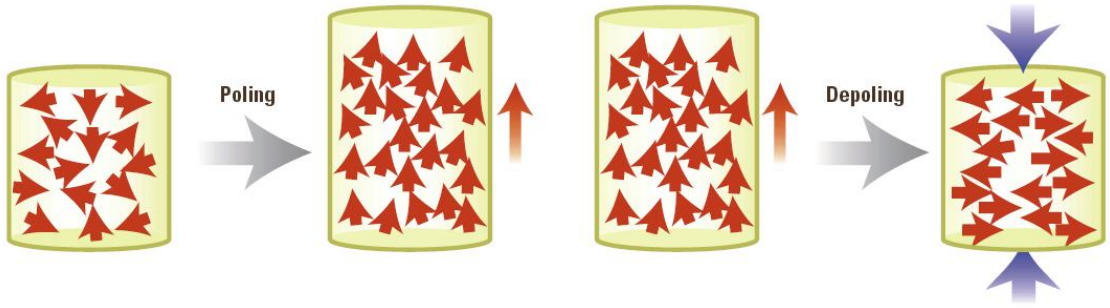

Figure 7.3. Effect of poling and depoling. Red arrow indicates the direction of electric dipoles, and the blue arrow shows the direction of applied stress.

The poling process tries to induce domains in the direction of applied electric field with the lowest possible field, at a temperature close to R*T* in shortest possible time. For soft PZT, at R*T*, poling at a field larger than the coercive field is adequate to reach full polarization. For hard ferroelectric ceramics, moderate poling conditions are not adequate due to the pinning of domain walls due to defects. Depinning of the domain walls can be done by applying a high temperature and high periodic electric field before normal poling or by quenching from a high temperature where the samples have high piezoelectric properties.[2, 129, 130, 131]

7.3 IR Measurements

Using the IR spectroscopy measurements we attempted to study the anisotropy in the phonon spectra introduced by poling the PZT sample. IR measurement is most appropriate direct technique for studying the strong polar modes as the mode strengths are directly proportional to the square of the associated dipole moment.

Figure 7.4 gives the R*T* reflectivity and Im[1/ε] spectrum obtained from the KKR analysis of hard and soft PZT, with the IR polarization parallel and perpendicular to the poling direction. The reflectivity spectra of PZT, as expected for the lead based perovskites have three main bands originating from the Last, Slater and Axe-type vibrations as described in section 1.2. The broad dip near the 350 cm^{-1} is considered as the fourth band, which arises either due to the Zr-Ti short-range order on the 'B' site perovskite position[88, 89], or due to the *E*- A_1 splitting of the TO2 Slater mode [29,133,178,179].

In figure 7.4(a) the anisotropy introduced by poling in hard PZT is visible by comparing the reflectivity spectrum (black and red lines) obtained when the IR polarization is along and perpendicular to the poling direction. This anisotropy is well observed near the dips around 150 cm^{-1} and 430 cm^{-1}, which correspond to the LO1 and LO2 bands. Similar shifts are observed when the polarization is parallel and perpendicular to the poling direction in soft PZT as seen in figure 7.4(b).

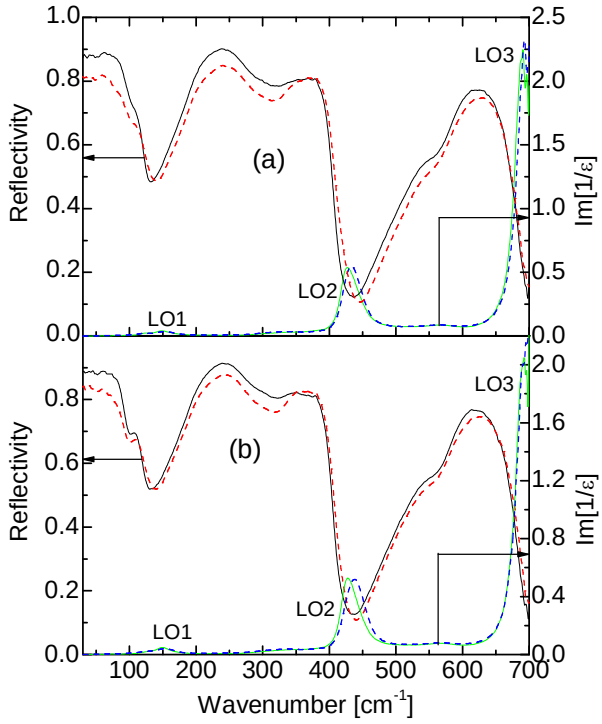

Figure 7.4. RT reflectivity and Im[1/ε] spectrum from KKR analysis of (a) hard PZT (APC 840) and (b) soft PZT (APC 850) samples. Solid (dashed) line stands for the polarization perpendicular (parallel) to the poling direction.

The minima observed when the polarization is parallel are higher than the minima when the polarization is perpendicular. This can be understood in the context that the poling introduces anisotropy and when polarization is parallel, it corresponds preferentially to A_1-spectra and for polarization perpendicular, it corresponds preferentially to *E*-spectra. In a poled ceramics, even a perfect poling cannot obtain the intrinsic *E* and A_1 spectra. The spectra when the electric field is parallel to the spontaneous polarization would probe the intrinsic A_1 modes and the A_1 mode frequencies are usually higher than the corresponding *E* modes.[29]

To understand the anisotropy introduced by poling, the response function Im[1/ε] was calculated using Kramers-Kronig relation (KKR) as given in section 3.3.3.3. Since the peaks in Im[1/ε] spectra give the LO bands, the shift in LO frequencies are estimated to be around 5-10 cm^{-1} for both the LO1 and LO2 in figure 7.4. Although this quantity is obviously smaller than the full magnitude of the intrinsic microscopic A_1-E splitting, this might be used to measure the poling degree.

IR reflectivity spectrum obtained on the unpolished side of the poled sample is given in figure 7.5. It is observed that the anisotropy introduced by poling is barely dependent on mechanical polishing. The decrease in the intensity of reflectivity spectrum in figure 7.5 is due to the fact that the reflected light from the rough sample surface is partially scattered and not observed by the detector.

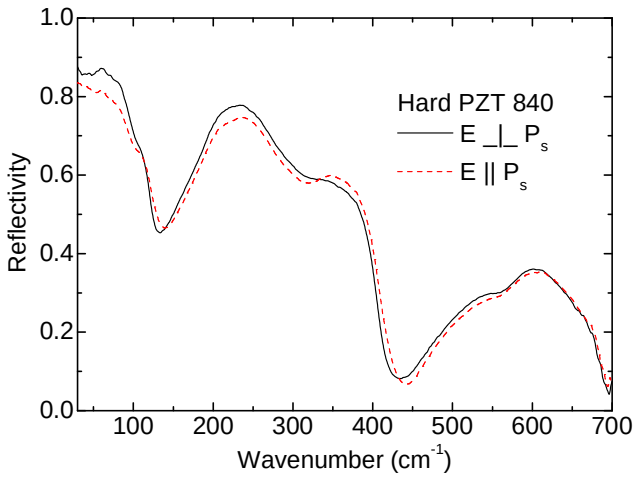

Figure 7.5. RT reflectivity spectrum of Hard PZT APC840 from the unpolished side. Solid (dashed) line stands for polarization perpendicular (parallel) to the poling direction.

The real and imaginary part of the permittivity spectra of hard PZT APC 840 is shown in figure 7.6. Since maxima in the loss function should correspond to the TO mode frequencies in an ideal crystal, the bands below 100, near 200 and 530 cm^{-1} are associated with the TO1, TO2, and TO3 modes in the poled ceramics. The up-shift for the TO2 and TO3 recorded with polarization along the poling direction is about 7 cm^{-1} and 5 cm^{-1}, respectively. The intensity redistribution in the poled ceramics is also associated with the high-frequency side peaks, which show close resemblance to the A_1 like parts of the TO2 and TO3 bands.[29] Such intensity redistribution also makes the poling-direction spectrum closer to the one theoretically given by the A_1 modes. This kind of intensity

redistribution behavior is typical for the case when the A_1-E splitting is larger than the mode damping, while the simple frequency shift is expected when the microscopic A_1-E components are overlapping.

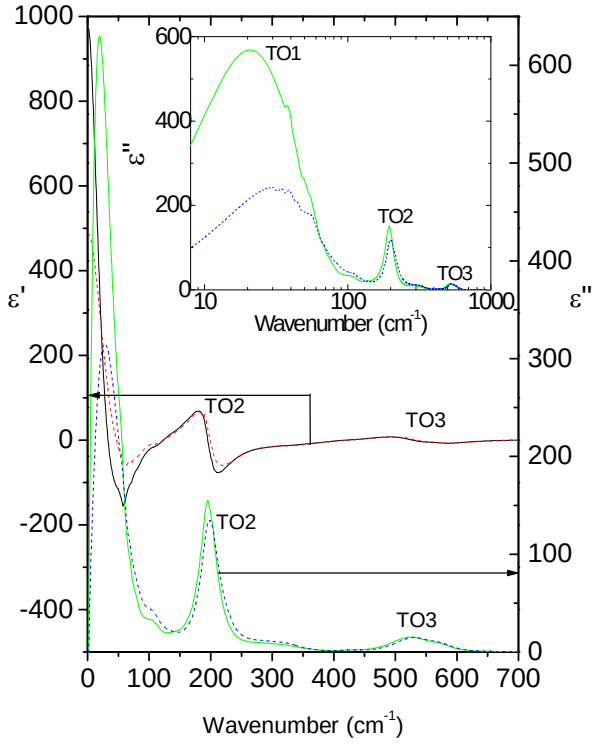

Figure 7.6. Real and imaginary part of dielectric spectrum of hard PZT (APC840) from KKR analysis. Solid (dashed) line stands for polarization perpendicular (parallel) to the poling direction. Inset shows the loss function with logarithmic scale for the wave number axis.

7.3.1 Temperature Measurements

The sample was heated to high temperature; up to 675 K, into the paraelectric phase and the corresponding reflectivity spectra were recorded. To study the effect of depolarization, the poled sample was heated with the IR polarization parallel to the poling direction. Figure 7.7 shows these high temperature reflectivity spectra. They show shift in the spectral minima as the temperature increases. This corresponds to the lowering of the LO mode frequencies as the temperature is increased.

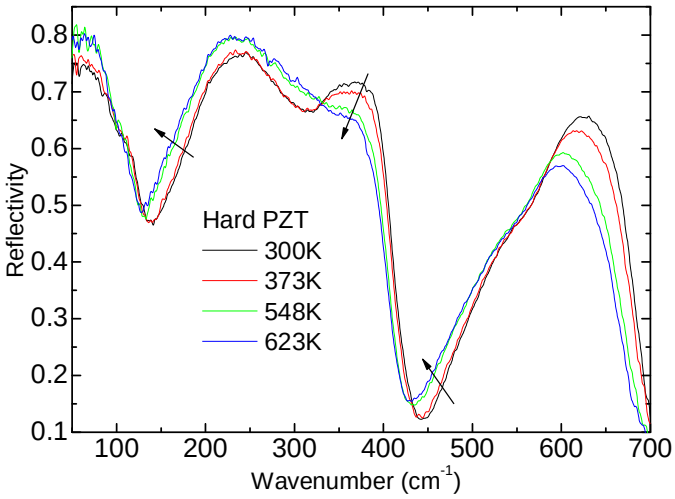

Figure 7.7. Temperature dependence of IR reflectivity spectrum of a poled hard PZT (APC880) for light polarized along the poling direction at several temperatures on heating.

Figure 7.8 gives the temperature dependent LO2 mode positions as the sample is heated and then cooled. As the specimen was heated above the PT temperature ($\approx T_0$ = 580 K), the cooling spectra will be depolarized. After the depolarizing experiment, at R*T*, the LO2 mode position is shifted almost by 8 cm^{-1} as seen in figure 7.8 (inset).

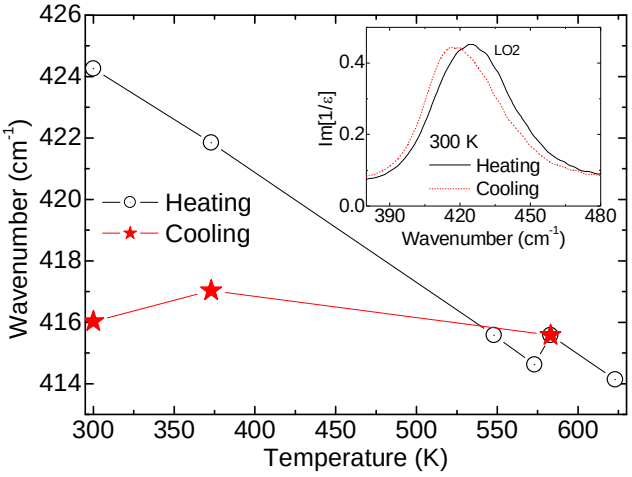

Figure 7.8. Temperature dependence of the LO2 band position obtained from fitting of Im[1/ε] spectra. Inset: Im[1/ε] spectrum of a hard PZT (APC880) for light polarized along the poling direction at T = 300 K in the heating and cooling sequence.

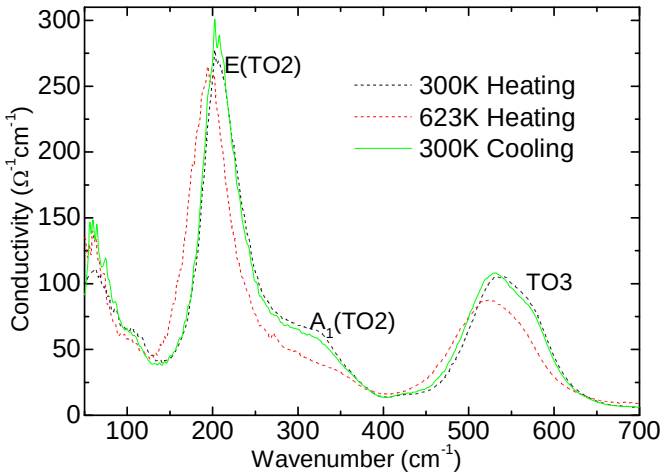

Figure 7.9. Conductivity spectra $\varepsilon_0\varepsilon\omega$ of a hard PZT (APC880) sample for IR light polarized parallel to the poling direction, during the same heating sequence as in figure 7.6. Solid line stands for RT measurement after heating the specimen above the depoling temperature.

The temperature dependent conductivity spectra $\varepsilon_0\varepsilon\omega$ show the temperature evolution of the effective TO bands in figure 7.9. Here, a similar though less pronounced permanent shift in TO bands (w.r.t that of the originally poled specimen) has been noticed, too.

7.4 Raman Measurement

Raman spectra were obtained for the PZT specimen in the range of 100-2000 cm^{-1}, as described in section 3.4.1, using the 514.5 nm Ar-laser line focused to a 2-3 µm

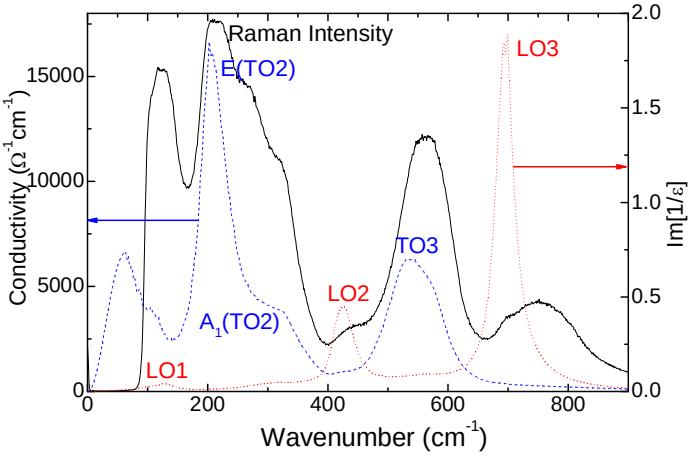

Figure 7.10. Comparison of the RT optical conductivity (left scale), Im[1/ε] (right scale), and Raman spectra (arbitrary intensity units) for light polarized along the poling direction in poled hard PZT APC840 ceramics.

sized spot. The Raman spectra are compared with the conductivity and response function obtained from IR measurements in figure 7.10. Similar discrepancy in the IR and Raman mode positions is common in many lead-based relaxor.[29, 88]

7.5 Discussion

The considerable local dielectric anisotropy of ferroelectric ceramics like PZT has to be taken into account when analyzing their reflectivity spectra[29], since poled PZT ceramics have wide applications. The effect of poling is pronouncedly seen in the case of LO2 band frequency where the shift observed in the poling direction is around 5 to 8 cm^{-1}. Similar frequency up-shifts are observed also in the case of LO1, TO2 and TO3 bands. Here intensity redistribution occurs in the case of TO2 and TO3 bands. Since the actual reflectivity spectra are not reliable at low frequency, the frequency shift of lower TO1 mode could not be estimated.

Because the dielectric response should depend only on the direction of the local polar axis but not on the sense of the spontaneous polarization the changes in the macroscopic dielectric anisotropy probed in IR experiments testify the displacement of the 90° (twin) domain walls in the poling and depoling process, while the arrangement of the eventual 180° domain wall system does not contribute here at all.

Comparing the reflectivity spectra of poled PZT, given in figure 7.4, with the PTO ceramics in figure 4.3, both reflectivity spectra have the basic Last, Slater and Axe modes. However the PTO ceramics shows some differences as compared to already measured PTO ceramic reflectivity spectra.[137,79] The poled PZT shows smooth reflectivity spectra as compared to the PTO ceramics. Comparing the permittivity, PZT has higher static permittivity than PTO ceramics. From the loss spectra it is seen that the PTO ceramics have parameters very close to those obtained for PTO bulk by Foster *et al.* (1993). Table 7.1 gives a comparison between *E*(TO) and *E*(LO) modes obtained for PTO single crystal, PTO ceramics and PZT.

The effect of poling is well studied by comparing the *E*(TO) and *E*(LO) mode frequencies. A frequency difference up to 4-11 cm^{-1} has been introduced in PZT due to poling. The P_s parallel to poling direction has always higher frequency than the corresponding frequency when the P_s is perpendicular to the poling direction.

	PTO single crystal (Foster *et al.* 1993)	PTO ceramics	Hard PZT Ps ‖ poling	Hard PZT Ps_|_ poling
E(TO1)	87.5	76	28	19
E(TO2)	218.5	202	199	195
E(TO3)	505	494	532	524
E(LO1)	128	125	129	125
E(LO2)	440.5	436	427	416
E(LO3)	687	689	700	692

Table 7.1: Comparison between E(TO) and E(LO) mode frequencies obtained for PTO single crystal by Foster et al. (1993), PTO ceramics, and hard PZT with P_s parallel and perpendicular to poling direction from present work.

Comparing the mode frequencies of PTO ceramic and PZT, it is seen that PTO ceramics have higher frequencies than for PZT except for *E*(TO3) and *E*(LO3). The same observation is also valid for comparison between PTO single crystal and PZT.

The Raman study shows that frequency shifts in PZT ceramics can be ascribed to the dynamical inhomogeneous depolarization fields, given by the dynamical charges located on nodal planes of the corresponding phonon wave. The distance of such nodal planes, determined by the scattering geometry, incident photon momentum, and momentum conservation condition, is typically of the order of few hundreds of nanometers. Rotation of the optical axis of the phonon-frequency dielectric tensor at the twin walls should lead to additional inhomogeneous depolarization fields, comparable to those experienced by the very long wavelength polar phonons probed by IR experiment.[29] If so, then it is not only the light propagation through the inhomogeneous medium, the angular averaging of the scattering by oblique modes on arbitrarily oriented crystallites and eventual confinement effects, but also these complex inhomogeneous depolarization field effects what might contribute to the observed Raman spectral features in these materials.[131]

Publication Related to this work:-

E. Simon, J. Hlinka, S. Kamba, I. Gregora, J. Erhart, Influence of poling on far-infrared response of lead zirconate titanate ceramics. J. Appl. Phys. 106 (2009) 074104(1) - 074104(5).

CHAPTER 8 Conclusions

This work is mainly focused on lead-based ceramics, thin films and PZT, and the aim was to study their lattice dynamics, phonon modes, and domain structure. Different experimental techniques like IR spectroscopy, Raman spectroscopy and PFM imaging have been used extensively throughout this work. Effective medium approximation including the Bruggeman effective medium approximation, Lichtenecker mixing formula and Arlt and Peusens model approximation gives a theoretical background for the experimental results. The results obtained can be concluded as follows:

- The imaginary part of permittivity obtained for PTO ceramics, poled PZT ceramics and 250 nm thick PTO/LAO film is given in figure 8.1.

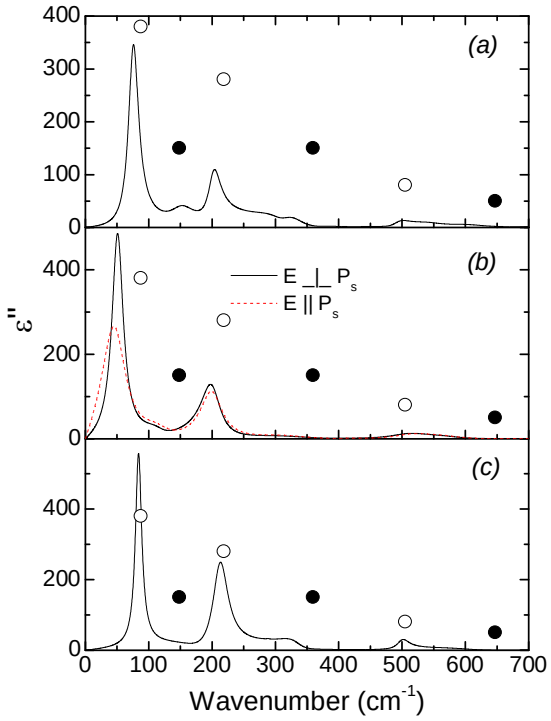

Figure 8.1. Imaginary part of permittivity at RT for (a) PTO ceramics, (b) Hard PZT APC840 ceramics and (c) 250nm thick PTO film on LAO substrate.

Figure 8.1 shows close resemblance to the peak positions obtained for PTO single crystal by Foster *et.al.* (1993)[138]. In all three cases the obtained spectra have overlapping of *E*- and A_1-mode components. The presence of *E*(TO) modes give evidence for *c*-domains and A_1(TO) mode sidebands give evidence for the presence of *a*- domains. The imaginary part of permittivity obtained for PTO thin

film on different substrates namely LAO, LSAT, MgO, NGO and STO also shows the presence of domains based on their in-plane strain.

- The fitting parameters obtained for PTO ceramics, PTO thin film and PZT using *3*-parameter model and *4*-parameter model and KKR give all the *E* and A_1 modes positions as expected by PTO single crystal. A slight shift in the mode positions can be explained as a result of domain formation and residual stress.[63, 64, 146] The additional bands other than the *E* and A_1 modes in PTO ceramics are originating from the geometric resonances due to the domain structure, probably related to the strain-compensation ferroelastic twinning.[87]
- Presence of domains is confirmed in PTO ceramics and thin films. As expected, in thicker thin film, domain patterns including all three ferroelastic domain state[172, 173] are seen. PFM images show that these *a*-domains are located in qualitatively different environments, in particular, as a part of both *c*/*a*/*c*/*a* and $a_1/a_2/a_1/a_2$ type structures. PFM images also demonstrate the presence of the 180^0 walls between the outward and inward oriented *c*-domains. Finally, IR reflectance spectra revel considerable broadening and shifts of A_1 vibrational bands originating from *a*-domains. The geometric resonances give evidence of α-type of domain configuration with 90^0 twin domains in PTO ceramics .[87]
- As the PTO ceramics and thin films have complex domain structure, the theoretical model helps to obtain dielectric function using the parameters on PTO single crystal. Different approximations made in the case of Bruggeman effective medium approximation, Lichtenecker mixing formula and Arlt and Peusens model allow appreciating the differences in the reflectivity spectra.
- Poling introduces anisotropy on dynamics of polar lattice modes in PZT ceramics. The observed changes are predictable and detectable, so that the IR spectroscopy technique can be used for quantitative studies of poling and depoling processes in PZT ceramics.
- PFM microscopy images allow to get local insight in the complex nanodomain structure with all six tetragonal ferroelectric domain states and both 180^0 and 90^0. IR reflectance measurements could serve as a very useful complementary tool for investigation of multidomain ferroelectric thin film because the typical probing

surface is about 10 mm^2 so the good special averaging is naturally ensured by this technique.

CHAPTER 9 Future Works

There are number of other interesting issues that appeared during this work but were left for future investigation. These includes, in particular:

- Detailed studies on the domain structure of PTO/MgO films (Figure 5.8). This may be interesting as the MgO substrate is transparent below 100 cm^{-1} - the IR transmission spectra along with the reflectance spectra may help to get a better picture about the domain state.
- Detailed studies on the domain structure of PTO/STO films It can be interesting as the misfit strain for the PTO/STO is comparatively lower (table 5.3) than the magnitude MgO and it allows to grow films on substrates with different crystallographic orientations. Certainly, these domain structures on these films would reflect the substrate crystallographic orientation.
- Detailed studies on the domain structure of films on conductive substrates. Doping of STO(111) with 0.5 % Nb makes the substrate conductive. The effect of conductive substrate on domain formation can be thus studied.
- Detailed studies on the domain textures in PZT single crystals. In PZT, near the MPB, the tetragonal phase can have 6 possible domain states and rhombohedral phase can have 8 possible domain states. As the PZT is poled, the domains can have at least 14 possible directions in MPB region. It will be interesting to investigate the domain structure near the MPB using PFM and Raman techniques. Literature shows the PFM images of domains in PZT[185] and possible domain states in poled PZT are discussed by Park and Shrout (1997)[186], but the data obtained in ceramics samples are difficult to interpret. The PFM imaging of poled PZT single crystals could be of great interest for understanding various previous experiments and it can be helpful for improvements of functional properties of this important piezoelectric ceramic material.

In summary, it was shown in several ways in this thesis that domain structure of lead-based perovskites does significantly influence their phonon spectra and that this influence can be well understood. Therefore, we can generally conclude that spectroscopic techniques used for studying of polar lattice vibrations, such as IR spectroscopy, are sensitive to the domain structure of ferroelectric perovskites.

The domain-structure related effects are typically rather faint in their magnitude but with the gradual improvements of the experimental precision, they should be more and more easily accessible for measurements and analysis. The outcome of the few cases studied here in detail indicates that many more domain structure related effects are yet to be uncovered. Therefore, these techniques have a real potential to be used in future as tools for revealing the information about their domain structure.

Bibliography

1. Valasek J., Phys. Rev. **17**, 475 (1921).
2. Cross L. E., Mater. Chem. Phys. **43**, 108 (1996).
3. Scott J. F., Science **315**, 954 (2007).
4. Scott J. F. and Araujo C. A., Science **246**, 1400 (1989).
5. http://www.electronics.ca/reports/technology/piezoelectric_devices.html
6. Lines M. E. and Glass A. M., Principles and applications of ferroelectrics and related materials, Uarendo, Oxford (1972).
7. Molotskii M., Rosenwaks Y. and Rosenman G., Annu. Rev. Mater. Res. **37**, 271 (2007).
8. Junquera J. and Ghosez Ph., Nature **422**, 506 (2003).
9. Takayama R., Tomita Y., Iilima K. and Ueda I., J. Appl. Phys. **63**, 5868 (1988).
10. Ohtani K., Okuyama M. and Hamakawa Y., Jpn. J. Appl. Phys Suppl. **23**, 133 (1983).
11. Dawber M., Rabe K. M., and Scott J. F., Rev. Mod. Phys. **77**, 1083 (2005).
12. Speck J. S. and Pompe W., J. Appl. Phys. **76**, 466 (1994).
13. Ramesh R., Sands T., and Keramidas V. G., Appl. Phys. Lett. **63**, 731 (1993).
14. Koukhar V. J., Pertsev N. A., and Waser R., Phys. Rev. B **64**, 214103 (2001).
15. Yu S. H., Li Y. L., and Chen L. Q., J. Appl. Phys. **94**, 2542 (2003).
16. Li Y. L., Hu S. Y., Liu Z. K and Chen. L. Q., Appl Phys Lett **78**, 3878 (2001).
17. Damjanovic D., Rep. Prog. Phys. **61**, 1267 (1998).
18. Setter N., Damjanovic D., Eng L., Fox G., Gevorgian S., Hong S., Kingon A., Kohlstedt H., Park N. Y., Stephenson G. B., Stolitchnov I., Taganstev A. K., Taylor D. V., Yamada T. and Streiffer S., J. Appl. Phys. **100**, 051606 (2006).
19. Ganpule C. S., Nagarajan V., Hill B. K., Roytburd A. L., Williams E. D., Ramesh R., Alpay S. P., Roelofs A., Waser R. and Eng L. M., J. Appl. Phys. **91**, 1477 (2002).
20. Saurenbach F., Terris B. D., Appl. Phys. Lett. **56**, 1703, (1990).
21. Luthi R., Haefke H., Meyer K.P., Meyer E., Howald L., Guntherodt H.J., J. Appl. Phys. **74**, 7461 (1993).
22. Zavala G., Fendler J. H. and Trolier-McKinstry S. E., J. Appl. Phys. **81**, 7480 (1997).
23. Gruverman A., Auciello O. and Tokumoto H., Annu. Rev. Mater. Sci. **28**, 101 (1998).
24. Kang Y. M. and Baik S., J. Appl. Phys. **82**, 2532 (1997).
25. Graef M. De and Mc Henry M. E., Structure of Materials: an introduction to crystallography, diffraction and symmetry, Cambridge University Press, p. 671, (2007).
26. Last J. T., Phys. Rev. **105**, 1740 (1957).
27. Slater J. C., Phys. Rev. **78**, 748 (1950).
28. Axe J. D., Phys. Rev. **157**, 429 (1957).
29. Hlinka J., Petzelt J., Kamba S., Noujni D. and Otsapchuk T., Phase Transit. **79**, 41 (2006).
30. Ashcroft N. W. and Mermin N. D., Solid State Physics, Harcourt College Publishers, (1976).

31. Kittel C., Introduction to Solid State Physics, Eight Edition, Wiley, John & Sons Incorporated, (2004).
32. Singh J., Lecture Note on Lattice Vibrations: Phonon Scattering, http://www.cambridge.org/resources/052182379X/2064_ch06.pdf
33. Bruesch P., Phonons: theory and experiment I, Series in Solid State Sciences 34, Springer- Verlag Berlin Heidelberg New York (1982).
34. Fox M., Optical properties of Solids, Second edition, Oxford University press, (2010).
35. Gervais F., Infrared and millimeter waves, 8, Chapter 7, edited by K. J. Button, Ac. Press, New York, (1983).
36. Chaves A. S. and Porto S. P. S., Solid State Commun. **13**, 865 (1973).
37. Sawyer C. B. and Tower C. H., Phys. Rev. **35**, 269 (1930).
38. Uchino K., Am. Ceram. Soc. Bull. **65**, 647 (1986).
39. Marton P., Rychetsky I., and Hlinka J., Phys. Rev. B **81**, 144125 (2010).
40. Devonshire A. F., Advanc. in Phys. **3**, 85 (1954).
41. Devonshire A. F., Phil. Mag. **40**, 1040 (1949).
42. Devonshire A. F., Phil. Mag., **42**, 1065 (1951).
43. Cochran W., Phys. Rev. Letters **2**, 495 (1959).
44. Kempa M., Hlinka J., Kulda J., Bourges P., Kania A., and Petzelt J., Phase Transitions 79, 351 (2006).
45. Hlinka J., Kempa M., Kulda J., Bourges P., Kania A., and Petzelt J., Phys. Rev. B 73, 140101 (2006).
46. Bruce A. D. and Cowley R. A., Structural Phase transitions, London, Taylor & Francis (1981).
47. Buixaderas E., Kamba S. and Petzelt J., Ferroelectrics, **308**, 131 (2004).
48. Fong D. D. and Thompson, Annu. Rev. Mater. Res. **36**, 431 (2006).
49. Okino H., Ida T., Ebihara H., Yamada H., Matsushige K. and Yamamoto T., Jpn. J. Appl. Phys., **40**, 5828 (2001).
50. Pompe W., Gong X., Suo Z., Speck J. S., J. Appl. Phys. **74**, 6012–19 (1993).
51. Jang H. M., Oak M.-Ae, Lee J-H., Jeong Y.K, and Scott J. F., Phys. Rev. B, 80, 132105 (2009)
52. Arlt G., Ferroelectrics **91**, 3 (1989).
53. Wang Y. G., Zhong W. L. and Zhang P. L., Phys. Rev. B **51**, 5311 (1995).
54. Fousek J. and Janovec V., J. Appl. Phys. **40**, 135 (1969).
55. Jeong H. T., Cho Y. C., Cho C. R. and Jeong Se- Y., J. Phys. Soc. Jpn. **70,** 2588 (2001).
56. Lee D., Behera R. K., Wu P., Xu H., Li Y. L., Sinnott S. B., Phillpot S. R., Chen L. Q., and Gopalan V., Phys. Rev. B **80**, 060102 (2009).
57. Dimos D. and Mueller C. H., Annu. Rev. Mater. Sci. **28**, 397–419 (1998).
58. Choi K. J., Biegalski M., Li Y. L., Sharan A., Schubert J., Uecker R., Reiche P., Chen Y. B., Pan X. Q., Gopalan V., Chen L-Q., Schlom D. G., and Eom C. B., Science **306**, 1005 (2004).
59. Kuroiwa Y., Aoyag S. i, Sawada A., Harada J., Nishibori E., Takata M., and Sakata M., Phys. Rev. Lett. 87, 217601 (2001).
60. Cohen R. E., Nature 358, 136 (1992).
61. Kwak B. S., Erbil A., Wilkens B. J., Budai J. D., Chisholm M. F., and Boather L. A., Phys. Rev. Lett. **68**, 3733 (1992).

62. Schlom D. G., Chen L. Q., Eom C. B., Rabe K. M., Streiffer S. K. and Triscone J. M., Annu. Rev. Mater. Res. **37**, 589 (2007).
63. Bartasyte A., Margueron S., Kreisel J., Bourson P., Chaix-Pluchery O., Rapenne-Homand L., Santiso J., Jimenez C., Abrutis A., Weiss F. and Fontana M. D., Phys. Rev. B **79**, 104104 (2009).
64. Bartasyte A., Chaix-Pluchery O., Kreisel J., Santiso J., Margueron S., Boudard M., Jimenez C., Abrutis A., and Weiss F., IEEE Trans. Ultrason. Ferroelectr. Freq. Control **54**, 2623 (2007).
65. Sun L., Chen Y. F., He L., Ge C. Z., Ding D. S., Yu T., Zhang M. S. and Ming N. B., Phys. Rev. B **55**, 12218 (1997).
66. Feng Z. C., Kwaqk B. S., Erbil A. and Boatner L. A., Appl. Phys. Lett. **62**, 349(1993).
67. Oja R., Johnston K., Frantti J. and Nieminen R. M., Phys. Rev. B **78**, 094102 (2008).
68. Bartasyte A., Abrutis A., Jimenez C., Weiss F., Chaix-Pluchery O., and Saltyte Z., Ferroelectrics **353**, 104 (2007).
69. Bartasyte A., Bouregba R., Dogheche E., Boudard M., Poullain G., Jimenez C., Plausinaitiene V., Remiens D., Abrutis A., Weiss F., Chaix-Pluchery O., and Saltyte Z., J. Surf. Coat. Technol., **201**, pp. 9340–9344 (2007).
70. Bartasyte A., Chaix-Pluchery O., Kreisel J., Boudard M., Jimenez C., Abrutis A., Weiss F. and Saltyte Z., J. Appl. Phys. **103**, 014103 (2008).
71. Bartasyte A., Dkhil B., Kreisel J., Chevreul J., Chaix-Pluchery O., Rapenne-Homand L., Jimenez C., Abrutis A. and Weiss F., Appl. Phys. Lett. **93**, 242907 (2008).
72. Lee S. W., Jang H. M., Cho S. M. and Yi G. C., Appl. Phys. Lett. **80,** 3165 (2002).
73. Foster C. M., Li Z., Buckett M., Miller D., Baldo P. M., Rehn L. E., Bai G. R., Guo D., You H. and Merkle K. L., J. Appl. Phys., **78**, 2607 (1995).
74. Pertsev N. A., Zembilgotov A. G., Tagantsev A. K., Phys. Rev. Lett. **80**, 1988–91, (1998).
75. Stemmer S., Streiffer S.K., Ernst F., Ruhle M., Hsu W.Y. and Raj R., Solid State Ionics **75**, 43 (1995).
76. Ostapchuk T., Petzelt J., Zelezny V., Pashkin A., Pokorny J., Drbohlav I., Kuzel R., Rafaja D., Gorshunov B. P., Dressel M., Ohly C., Hoffmann-Eifert S., and Waser R., Phys. Rev. B **66**, 235406 (2002).
77. Speck J. S. and Pompe W., J. Appl. Phys. **76**, 477 (1994).
78. Nagarajan V., Roytburd A., Stanishevsky A., Prasertchoung S., Zhao T., Chen L., Melngailis J., Auciello O. and Remesh R., Nature **2**, 43 (2002).
79. Tornberg N. E., and Perrry C. H., J. Chem Phys. 53, 2946 (1970).
80. Shirane S., Pepinsky R., and Frazer B. C., Acta crystalloge A 26, 244 (1970).
81. Pecharroman C. and Iglesias J. E., Phys. Rev. B **49**, 7139 (1994).
82. Hudak O., Rychetsky I., and Petzelt J., Ferroelectrics **208**, 429 (1998).
83. Bruggeman D. A. G., Ann. Phys. (Berlin) 24 636 (1935).
84. Zakri T., Laurent J. P. and Vauclin M., J. Phys., D: Appl. Phys. **31**, 1589 (1998).
85. Arlt G. and Peusens H., Ferroelectrics **48**, 214 (1983).
86. Arlt G. and Sasko P., J. Appl. Phys. **51**, 4956 (1980).

87. Hlinka J., Simon E., Bogicevic C., Karolak F. Amd Janolin P. –E., Phys. Rev. B 84, 092104 (2011).
88. Hlinka J., Ostapchuk T., Noujni D., Kamba S. and Petzelt J., Phys. Rev. Lett. **96**, 027601 (2006).
89. Buixaderas E., Kamba S., Petzelt J., Drahokoupil J., Laufek F. and Kosec M., Appl. Phys. Lett. **91**, 112909 (2007).
90. Chen Y. F., Chen J. X., Shun L., Tao T., Li P., Ming N. B. and Shi L. J., J. Crystal Growth **146**, 624 (1995).
91. Keijser M. de, Leeuw D. M. de, Veldhoven P. J. van, Veirmen A. E. M. De, Neerinck D. G. and Dormans G. J. M., Thin Solid Films **266**, 157(1995).
92. Schmidt C., Burte E. P., MOCVD of ferroelectric thin films, in: Allendorf M.D., Bernard C. (Eds.), Chemical Vapor Deposition, ECS Proceedings 97–25, 1055 (1997).
93. Funakubo H., Nagashima K., Shinozaki K., and Mizutani N., Thin Solid Films **368**, 261 (2000).
94. Budd K. D., Dey S. K, and Payne D. A., "SolGel Processing of $PbTiO_3$, $PbZrO_3$, PZT, and PLZT Thin Films," Br. Ceram. Proc., **36**, 107–21 (1985).
95. Kang Y. M., Bae S. C., Ku J. K., and Baik S., Thin Solid Films **312**, 40 (1998).
96. Wasa K., Haneda Y., Sato T., Adachi H. and Setsune K., Vacuum, **51**, 591 (1998).
97. Senateur J. P., Weiss F., Thomas O., Madar R. and Abrutis A., Patent 93/08838PCTFR94/00858 (Europe, USA).
98. Kamba S., Nuzhnyy D., Nechache R., Zaveta K., Niznansky D., Santava E., Harnagea C. and Pignolet A., Phys. Rev. B **77**, 104111 (2008).
99. Buixaderas E., PhD. Thesis, Universidad del Pais Vasco, (2001).
100. Barker A. S. and Hopfield S. S., Phys. Rev. **135**, A1732 (1964).
101. Servoin J. L., Gervais F., Quittet A. M., and Luspin Y., Phys. Rev. B **21**, 2038 (1980).
102. Gervais F. and Piriou B., J. Phys. C, **7**, 2374 (1974); Phys, Rev. B **10**, 1642 (1974).
103. Lowndes R. P., Phys. Rev. B **1**, 2754 (1970).
104. Berreman D. W. and Unterwald F. C., Phys. Rev. **174**, 791 (1968).
105. Boas M. L., Mathematical Methods in the Physical Sciences, John Wiley Sons, Inc. Hoboken, NJ (1983).
106. Jackson J.D., Classical Electrodynamics, 2nd edition. Wiley, New York (1975).
107. Bruesch P., Phonons: theory and experiment II, Series in Solid State Sciences 65, Springer- Verlag Berlin Heidelberg New York (1982).
108. Bedeaux D. and Vlieger J., Physica **67**, 55 (1973)
109. Heavens O.S., Rep. Prog. Phys. **23**, 1 (1960).
110. Ferraro J. R, Nakamoto K. and Brown C. W., Introduction to Raman Spectroscopy, Second Edition, Academic Press (2002).
111. Hayes W. and Loudon R., Scattering of light by Crystals, Wiley, (1978).
112. Gregora I., International Tables for Crystallography, Volume D: Physical Properties of Crystals, chapter Raman Scattering, Edited by A. Authier, pages 314-328. Kluwer Academic Publishers London, (2003).
113. Yacobi B. G., Semiconductor Materials, An Introduction to Basic Principles. Kluwer Academic/ Plenum Publishers, New York (2002).

114. Damen T. C., Porto S. P. S., and Tell B., Phys. Rev. **142**, 570 (1966).
115. Petzelt J., Ostapchuk T., Gregora I., Savinov M., Chvostova D., Liu J., and Shen Z., J. Eur. Ceram. Soc. **26**, 2855 (2006).
116. Bartasyte A., Margueron S., Santiso J., Hlinka J., Simon E., Gregora I., Chaix-Pluchery O., Kreisel J., Jimenez C., Weiss F., Kubilius V. and Abrutis A., Phase Transition, **84**, 509-520 (2011).
117. http://www.ntmdt.com/spm-principles/view/piezoresponse-force-microscopy
118. Wu S., Piezoresponse Force Microscopy, Application Note, Agilent Technologies, Inc. USA (2007).
119. Proksch R. and Kalinin S., Piezoresponse Force Microscopy with Asylum Research AFMs, Application Note 10, Asylum Research.
120. http://www.americanpiezo.com/piezo_theory/piezo_theory.pdf
121. http://arxiv.org/ftp/cond-mat/papers/0509/0509009.pdf
122. http://www.azonano.com/Details.asp?ArticleID=2682#2
123. NT-MDT, NTEGRA, Basic information- Part 1, Descriptive manual, Probe Nanolaboratory.
124. NT-MDT, NTEGRA, Setup and installation- Part 2, Descriptive manual, Probe Nanolaboratory.
125. NT-MDT, NTEGRA, Atomic Force Microscopy- Part 3, Descriptive manual, Probe Nanolaboratory.
126. NT-MDT, NTEGRA, Scanning Tunneling Microscopy- Part 4, Descriptive manual, Probe Nanolaboratory.
127. Garrett M. H., Chang J. Y, Jenssen H. P., and Warde C., Ferroelectrics **120**, 167 (1991).
128. Nakao O., Tomomatsu K., Ajimura S., Kurosaka A. and Tominaga H., Jpn. J. Appl. Phys. **31**, 3117 (1992).
129. Kamel T.M., Kools F.X.N.M. and With G. de, J. Eur. Ceram. Soc. **27**, 2471–2479 (2007).
130. Kamel T. M. and With G., J. Eur. Ceram. Soc. **28**, 1827–38 (2008).
131. Simon E., Hlinka J., Kamba S., Gregora I. and Erhart J., J. Appl. Phys. **106**, 074104 (2009).
132. Shirane G., Hoshino S., and Suzuki K., Phys. Rev. 80, 1105 (1950).
133. Lurio A. and Burns G., J. Appl. Phys. **45**, 1986 (1974).
134. Mabud S. A. and Glazer A. M., J. Appl. Cryst., **12**, 49 (1979).
135. Sicron N., Ravel B., Yacoby Y., Stern E. A., Dogan F. and Rehr J. J., Phys. Rev. B., **50**, 13168 (1994).
136. Fontana M. D., Idrissi H., Kugel G. E. and Wojcik K., Ferroelectrics **80**, 117 (1988).
137. Perry C. H., Khanna B. N. and Rupprecht G., Phys. Rev., **135**, A408 (1964).
138. Foster C. M., Li. Z., Grimsditch M., Chan S.K. and Lam D J., Phys. Rev. B **48**, 10160 (1993).
139. Burns G. and Scott B. A., Phys. Rev. Lett. **25**, 167 (1970).
140. Shirane G., Axe J. D., Harada J. and Remeika J. P., Phys. Rev. B **2**, 155 (1970).
141. Fontana M. D., Idrissi H. and Wojcik K., Europhys. Lett. **11**, 419 (1990).
142. Ostapchuk T., et al. (to be published)
143. Cerdeira F., Holzapfel W. B. and Bauerle D., Phys. Rev. B **11**, 1188 (1975).
144. Frey R. A. and Silberman E., Helv. Phys. Acta **49**, 1 (1976).

145. Rossetti G. A., Khachaturyan A. G., Akcay G. and Ni Y., J. Appl. Phys. **103**, 114113 (2008).
146. Simon E., Borodavka F., Gregora I., Nuzhnyy D., Kamba S. and Hlinka J., (2011).
147. Pertsev N. A. and Koukhar V. G., Phys. Rev. Lett. **84**, 3722 (2000).
148. Li Y. L., Hu S. Y., Liu Z. K and Chen L. Q., Acta Mater. **50**, 395 (2002).
149. van der Marel D., Habermeier H. -U., Heitmann D., König W., and Wittlin A., Physica C **176**, 1 (1991).
150. Calvani P., Capizzi M., Donato F., Dore P., Lupi S., Maselli P. and Varsamis C. P., Physica C **181**, 289 (1991).
151. Hayward S. A., Morrison F. D., Redfern S. A. T., Salje E. K. H., Scott J. F, Knight K. S., Tarantino S., Glazer A. M., Shuvaeva V., Daniel P., Zhang M., and Carpenter M. A., Phys. Rev. B **72**, 054110 (2005).
152. Bovtun V., Pashkov V., Kempa M., Kamba S., Eremenko A., Molchanov V., Poplavko Y., Yakymenko Y., Lee J H. and Schlom D. G., J. Appl. Phys. **109**, 024106 (2011).
153. Chakoumakos B. C., Schlom D. G., Urbanik M. and Luine J., J. Appl. Phys. **83**, 1979 (1998).
154. Cao W. and Cross L. E., Phys. Rev. B **47**, 4825 (1993).
155. Utke I., Klemenz C., Scheel H. J. And Nuesch P., J. Crystal Growth **174**, 813 (1997).
156. Nuzhnyy D., Petzelt J., Kamba S., Marti X., Cechal T., Brooks C. M. and Schlom D. G., J. Phys. : Condens. Matter **23**, 045901 (2011).
157. Jaffe B., Cook W. R. and Jaffe H., Piezoelectric Ceramics, Academic, London p. 136 (1971).
158. Ouillion R., Pinan-Lucarre J-P., Ranson P., Pruzan Ph., Mishra S. K., Rajan R. and Panday D., J. Phys. : Condens. Matter **14**, 2079 (2002).
159. Aruta C., Phys. Status Solidi A, **183**, 353 (2001).
160. Brooks N. B., Solid State Commun., **64**, 383 (1987).
161. Lee H. N. and Hesse D., Appl Phys Lett **80**, 1040 (2002).
162. Chu Y-H., Cruz M. P., Yang C-H., Martin L. W., Yang P-L., Zhang J-X., Lee Kilho, Yu P., Chen L-Q. and Ramesh R., Adv. Mater. **19**, 2662 (2007).
163. Noheda B., Cox D. E., Shirane G., Gonzalo J. A., Cross L. E. and Park S. E., Appl. Phys. Lett. **47**, 2059 (1999).
164. Streiffer S. K., Eastman J. A., Fong D. D., Thompson C., Munkholm A., Ramana Murty M. V., Auciello O., Bai G. R., and Stephenson G. B., Phys. Rev. Lett. **89**, 067601 (2002).
165. Fong D. D., Stephenson G. B., Streiffer S. K., Eastman J. A., Auciello O., Fuoss P. H., and Thompson C., Science **304**, 1650 (2004).
166. Lichtensteiger C., Triscone J.-M., Junquera J. and Ghosez P., Phys. Rev. Lett. **94**, 047603 (2005).
167. Roytburt A. L., Phys. Stat. Sol. (a) **37**, 329 (1976).
168. http://www.crystec.de/laalo3-e.html
169. Zhang Z. M., Choi B. I., Fink M. I. and Anderson A. C., J. Opt. Soc. Am. B **11**, 2252 (1994).
170. Li J. Y., Rogan R. C., Ustundag E. and Bhattacharya K., Nature Mat. **4**, 776 (2005).

171. Shu Y. C. and Bhattacharya K., Phil. Mag. B **81**, 2021 (2001).
172. Roytburd A., Alpay S., Bendersky L. A., Nagarajan V. and Ramesh R., J. Appl. Phys. **89**, 553 (2001).
173. Ganpule C. S., Roytburd A. L., Nagarajan V., Hill B. K., Ogale S. B., Williams E. D. and Ramesh R., Phys. Rev. B **65**, 014101 (2001).
174. Utsugi S., Fujisawa T., Ikariyama R., Yasui S., Nakaki H., Yamada T., Ishikawa M., Matsushima M., Morioka H. and Funakubo H., Appl. Phys. Lett. **94**, 052906 (2009).
175. Choi S. K., Ahn S. H., Jung W. W., Park J. C., Song S. A., Lim C. B., and Cho Y., Appl. Phys. Lett. **88**, 052901 (2006).
176. Slutsker J., Artemev A. and Roytburd A. L., J. Appl. Phys. **91**, 9049 (2002).
177. Haertling G. H., J. Am. Chem. Soc. **82**, 797 (1999).
178. Železný V., Simon P., Gervais F. and Kala T., Mater. Res. Bull. **22**, 1695 (1987).
179. Buixaderas E., Gregora I., Kamba S., Petzelt J., and Kosec M., J. Phys.: Condens. Matter **20**, 345229 (2008).

List of Tables

Table 4.1: Mode frequencies obtained for PTO single crystal using Raman spectroscopy by Burns *et al.* (1973)[139], Cerdeirs *et al.* (1975)[143], Frey *et al.* (1976)[144], Foster *et al.* (1993)[138] and using IR spectroscopy by Ostapchuk *et al.* (2011)[142].

Table 4.2: The list of the 11 TO and 11 LO polar mode frequencies and damping parameters (in cm^{-1}) obtained from the adjustment to the R*T* IR reflectance spectra of PTO ceramics (ω_∞=6.35). Values printed in bold correspond to the intrinsic modes of PTO.

Table 5.1: Deposition conditions for PTP layers grown by PI-MOCVD.

Table 5.2: TO frequencies of LAO at R*T* obtained by *3*-parameter and *4*-parameter fitting models by different authors.

Table 5.3: Characteristics of all substrates and of bulk PTO single crystal along with misfit strain and thermal strain for all film substrate system.

Table 5.4: Mode frequencies obtained for bulk PTO single crystal and 55 nm thick PTO thin films of LAO, LSAT, MgO, NGO, STO (100), STO (110) and STO (111) + 0.5% Nb.

Table 6.1: Polar phonon mode frequencies, damping and dielectric strength of the 250 nm PTO/LAO film at 10 K, 300 K, 573 K and 773 K.

Table 7.1: Comparison between *E*(TO) and *E*(LO) mode frequencies obtained for PTO single crystal by Foster *et al.* (1993), PTO ceramics, and hard PZT with *Ps* parallel and perpendicular to poling direction from present work.

List of Abbreviations

AFM	Atomic Force Microscopy
FIR	Far Infrared
FT	Fourier transform
FT-IR	Fourier transform Infrared spectroscopy
IR	Infrared
KKR	Kramers Kronig Relation
LA	Longitudinal Acoustic
LO	Longitudinal Optical
MOCVD	Metalorganic Chemical Vapour Deposition
MIR	Middle Infrared
NIR	Near Infrared
OPUS	Optics User Software
PT	Phase transition
PFM	Piezoresponse Force Microscopy
PLD	Pulse Laser Deposition
RT	Room Temperature
SEM	Scanning Electron Microscope
TA	Transverse Acoustic
TO	Transverse Optical
VPFM	Vertical PFM
XRD	X-ray diffraction

List of variables

a_g	grain size
a_f	lattice parameter of film
a_s	lattice parameter of substrate
$a(C)$	lattice parameter a in cubic phase
$a(T)$	lattice parameter a in tetragonal phase
C	Curie constant
$c(T)$	lattice parameter c in tetragonal phase
d_{33}	effective piezocoefficient
d_f	thin film thickness
e_I	polarization of incident beam
e_S	polarization of scattered beam
E_0	vibrational amplitude
E_c	Coercive field
F	free energy
f	oscillator strength
I_0	intensity of incident beam
I_R	intensity of reflected beam
I_T	intensity of transmitted beam
I_A	intensity absorbed by the sample
k	restoring force
k	extinction coefficient
n_0	refractive index of air
n_1	refractive index of thin film
n_2	refractive index of substrate
P_s	Spontaneous polarization
P_R	Remanent polarization
p	dipole moment
$\boldsymbol{q}$	quasi-momentum
q_0	vibrational amplitude
q	Effective charge
R	reflectivity
S	mechanical strain
T_C	Curie temperature
T_j	response function
T_p	processing temperature in cubic phase
T_{RT}	Room temperature
U	potential energy
V_{ac}	AC bias
V_{dc}	DC bias
V_s	surface potential
V_{tip}	voltage applied to the tip of the cantilever
W	domain period
w	domain width
W_f	permissible walls crystallographically prominent domain walls
$W\infty$	permissible walls with arbitrary orientation

X	mechanical stress
x	relative displacement
z	cantilever displacement
z_{dc}	static surface displacement
α	polarizability tensor
α	angle between lattice constants *b* and *c*
$\alpha_f(C)$	thermal expansion coefficient of film in cubic phase
α_s	thermal expansion coefficient of the substrate
β	angle between lattice constants *a* and *c*
γ	angle between lattice constants *a* and *b*
γ	damping rate
$\Delta\varepsilon_j$	dielectric strength
ε	complex dielectric function
ε’	permittivity- real part of complex dielectric function
ε”	dielectric losses- imaginary part of complex dielectric function
ε_0	permittivity of free space
ε_{eff}	homogeneous (averaged) effective dielectric function
εr	relative dielectric constant
ε_s	epitaxial strain
ε_∞	high frequency dielectric constant
ε_{33}	dielectric function when applied electric field is parallel to polarization
ε_{11}	dielectric function when applied electric field is perpendicular to polarization
η	Bose- Einstein factor
μ	reduced mass
μ	magnetic permeability
ν_I	frequency of incident beam
ν_S	frequency of scattered beam
ν_s	velocity of sound in medium
ν_0	frequency of incident light
ν_m	vibrational frequency of scattered crystal
τ	relaxation time
τ_p	phonon lifetime
ω	frequency
ω_{ac}	AC bias frequency
ω_{TO}	transverse eigen frequency
ω_{LO}	longitudinal eigen frequency
ω_{SM}	Soft mode frequency
$\hbar$	planks constant
$d\Omega$	solid- angle element

List of Publications

Published

(I publish under the name of my husband as E. Simon**)**

1. E. Simon, F. Borodavka, I. Gregora, D. Nuzhnyy, S. Kamba, J. Hlinka, A. Bartasyte and S. Margueron, Investigation of ferroelectric domains in epitaxial PbTiO3 films by piezoresponse force microscopy and far-infrared reflectance, J. Appl. Phy. 110, 084115 (2011).
2. J. Hlinka, E. Simon, C. Bogicevic, F. Karolak and P. E. Janolin, Geometric resonances in Far-infrered reflectance spectra of PbTiO3 ceramics. Phys. Rev. B. 84, 092104 (2011)
3. A. Bartasyte, S. Margueron, J. Santiso, J. Hlinka, E. Simon, I. Gregora, O. Chaix-Puchery, J. Kreisel, C. Jimenez, F. Weiss, V. Kubilius, A. Abrutis, Domain Structure and Raman modes of $PbTiO_3$, Phase Transition, 84 (2011) 509-520.
4. E. Simon, T. Ostapchuk, P. Kužel, J. Hlinka, S. Kamba, E. Nguema, P. Mounaix, J. C. Carru and G. Velu, Terahertz and far infrared response of $Ba_xSr_{1-x}TiO_3$ films, Phase Transitions, 83 (2010) 966 – 973.
5. I. Gregora, P. Ondrejkovič, E. Simon, M. Berta, M. Savinov, J. Hlinka, H. Luo, Q. Zhang, Raman Spectroscopy Study of $Na_{½}Bi_{½}TiO_3$-$BaTiO_3$ Lead-Free Single Crystal Relaxor Piezoelectrics, Ferroelectrics 404 (2010) 220 - 225.
6. E. Simon, J. Hlinka, S. Kamba, I. Gregora, J. Erhart, Influence of poling on far-infrared response of lead zirconate titanate ceramics. J. Appl. Phys. 106 (2009) 074104(1) - 074104(5).
7. S. Kamba, M. Savinov, F. Laufek, O. Tkáč, C. Kadlec, S. Veljko, E.V. John, O. Tkáč, G. Subodh, M.T. Sebastian, M. Klementová, V. Bovtun, J. Pokorný, V. Goian, J. Petzelt, Ferroelectric and incipient ferroelectric properties of a novel $Sr_{9-x}Pb_xCe_2Ti_{12}0_{36}$ (x=0-9) ceramic system, Chem. Mater. 21 (2009) 811 - 819.

In Progress

(I publish under the name of my husband as E. Simon**)**

8. S. Margueron, A. Bartasyte, A. M. Glazer, E. Simon, J. Hlinka and I. Gregora, Resolved E-Symmetry Zone-center Phonons in $LiTaO_3$ and $LiNbO_3$.
9. J. Hlinka, F. Borodavka, E. Simon, I. Gregora and S. Kamba, Lattice modes in paraelectric $La_{1/2}Na_{1/2}TiO_3$ by IR and Raman spectroscopy.